Colloidal Crystals:

Preparation, Characterization, and Applications

Dissertation zur Erlangung des Grades
„Doktor der Naturwissenschaften“
am Fachbereich Chemie, Pharmazie und Geowissenschaften
der Johannes-Gutenberg-Universität in Mainz

vorgelegt von

Jianjun Wang
geboren in Zhejiang / P. R. China

Mainz, 2006

Content

Chapter 1 General Introduction

1.1 Colloidal System

Colloids are small objects dispersed in a medium having at least one dimension in the range of 1nm to 1μm and often the upper limit can be extended to hundreds of microns. Brownian motion - resulting from the random bombardment of solvent molecules, is the characteristic feature of the colloidal particles. Colloidal particles are important in a broad range of technologies and in the processing of various materials including foods, inks, paints, coatings, cosmetics and photographic films, and thus are intensely studied in materials science, chemistry, and biology. Figure 1.1 shows a partial list of these colloidal systems, together with their typical range of critical dimensions.[1]

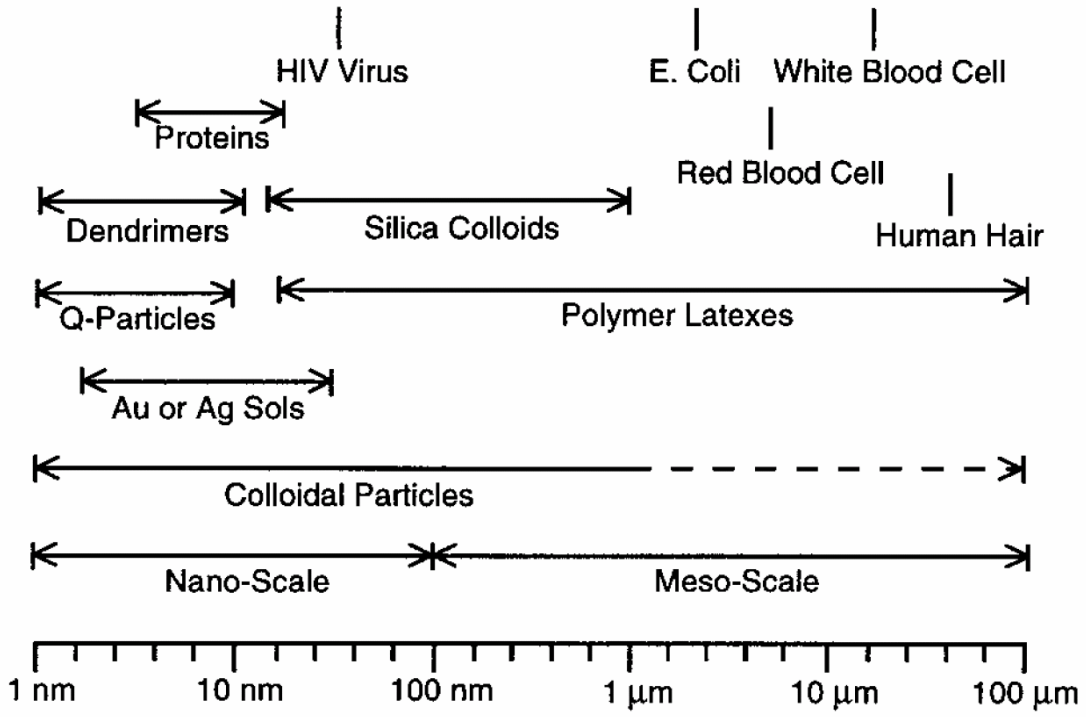

Fig. 1.1: A list of some of representitive colloidal systems, together with their typical ranges of dimensions. In this chart the upper limit of the critical dimension for colloids has been extended from 1μm to 100μm.[1]

1.2 Colloidal Crystals

Colloidal crystals are three-dimensional periodic lattices assembled from monodispersed spherical colloidal particles. For example, the natural opals, which show attractive iridescence, are polycrystalline colloidal crystals composed of the silica colloids and surrounding medium, and the iridescence is due to the diffraction of visible or near infrared light as a consequence of the periodic modulation of the refractive index between the silica particles and the surrounding medium as demonstrated in Figure 1.2.

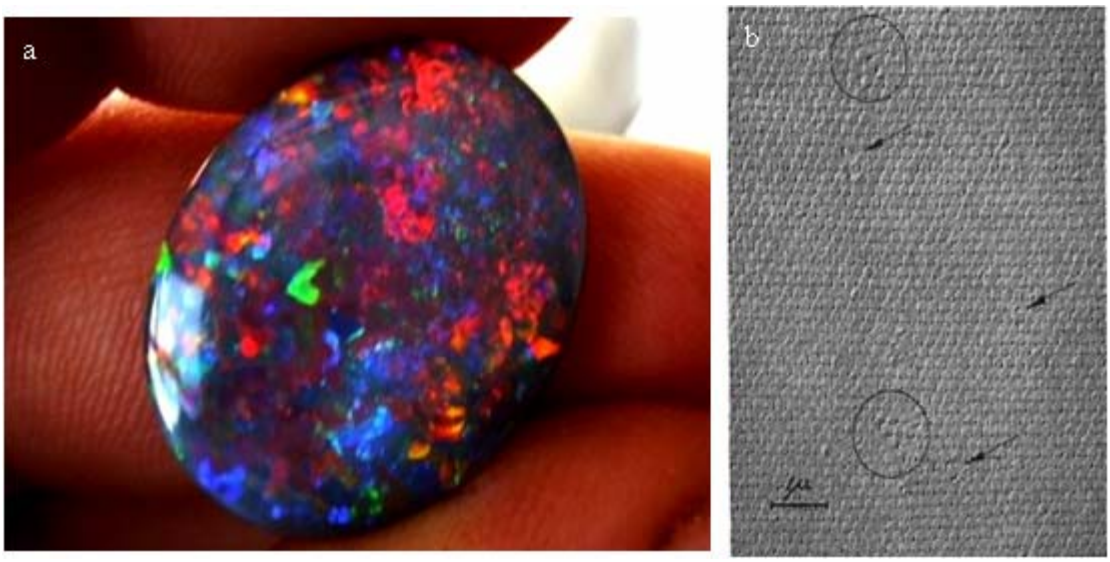

Fig. 1.2: a) Photographic image of a natural opal , and b) SEM image of the shadowed replica of the opal.[2]

Colloidal crystals have gained continuous interest mainly because of two reasons: Firstly, from the fundamental standpoint, colloidal crystals provide the best experimental realization of a hard sphere model, whose phase behaviour is completely dominated by entropy, thus the rich variety of the self assembly phenomena provide a fascinating test bed for the basic physical processes such as melting, freezing, and glass transitions.[3-7] Secondly, from materials standpoint, bottom up assembly - the assembly process present in bacteria,[8] macromolecules,[9] and submicron particles,[10] generates ordered structures with a precision that challenges current lithographic techniques. Most importantly, in recent years colloidal crystals have fully demonstrated the potential to obtain interesting and useful functionality not only from

the constituent materials of the colloidal particles but also from the long-range order of the crystalline lattice (metamaterials).

1.3 Colloidal Crystals and Photonic Crystals

Photonic crystals (PC) are an artificial crystalline solid built from building blocks that are approximately a thousand times larger than the atoms in traditional molecular crystals.[11-13] Because the length scale of the lattice is in the Vis or near IR range, the photonic crystal can influence the propagation of the electromagnetic waves in a similar way as a semiconductor does for electrons, that is, there exists a band gap that excludes the passage of the photons of some specific frequencies. This property can be utilized to control and manipulate photons, as depicted in Figure 1.3 where a point defect or line defect is introduced in the PC in order to suppress the spontaneous emission of light which determines fundamentally the maximum available output of the solar cell or to fabricate the wave-guide without any energy loss even at sharp bends.[14] Joannopoulus's photonic crystals micropolis, shown in Figure 1.4 is believed to represent the all-optical chip of the future,[11] where signals are transmitted with light rather than electrons. With the all-optical chips, it would be possible to build a personal computer that operates at hundreds of terahertz (10^{12} Hz), which is a great step forward in comparison with the semiconductor technology based on which producing a 10GHz (10^{9}Hz) personal computer is difficult.

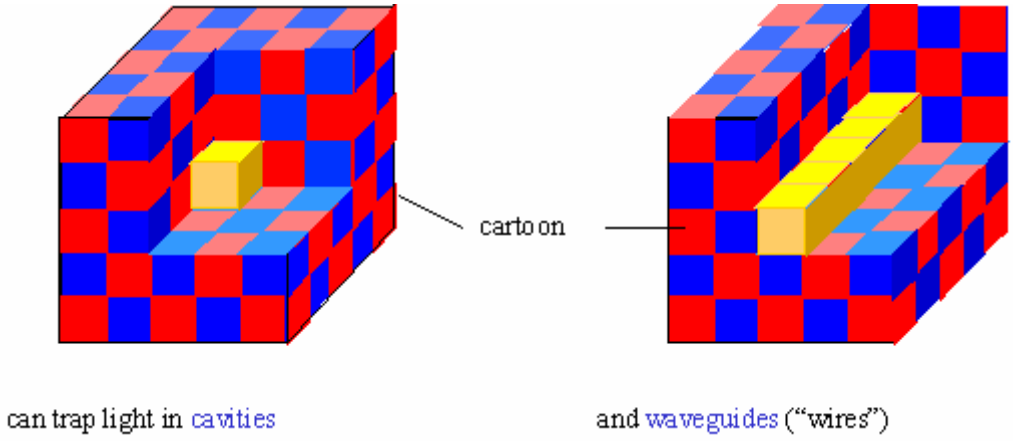

Fig. 1.3: Scheme of the point defect in PC to trap light (left) and line defect in PC to guide light without any energy loss even at sharp bends (right).[14]

Face centered cubic (fcc) colloidal crystals made of dielectric spheres do not possess a complete 3D photonic band gap - one that extends throughout the entire Brillouin zone in the photonic band structure, but a pseudo gap (so called stop gap) - it only shows up in the transition spectrum along a certain propagation direction, because of a symmetry-induced degeneracy of the polarization modes at the W point of the Brillouin zone. But this degeneracy can be broken by using shape-anisotropic[15] or dielectrically anisotropic[16] objects as building blocks. Photonic crystals can also be realized if the dielectric contrast of these systems is increased by using colloidal crystals as removable templates to structure high-index solids. The resulting macroporous samples, called inverse opals, possess arrays of air voids embedded with high-index solids such as ceramics or metals. In these inverted structures, a full photonic bandgap between the eighth and ninth bands can be achieved if the refractive index contrast between the air spheres and interstitial material exceeds 2.8.[17-19] It is worthwhile to mention that although complete photonic bandgap materials fabricated from colloidal crystals have not been realized, colloidal crystals with tunable stop band have been exploited as sensors to monitor the variation in temperature, strain, as well as the concentration of a chemical or biochemical species.[20-23]

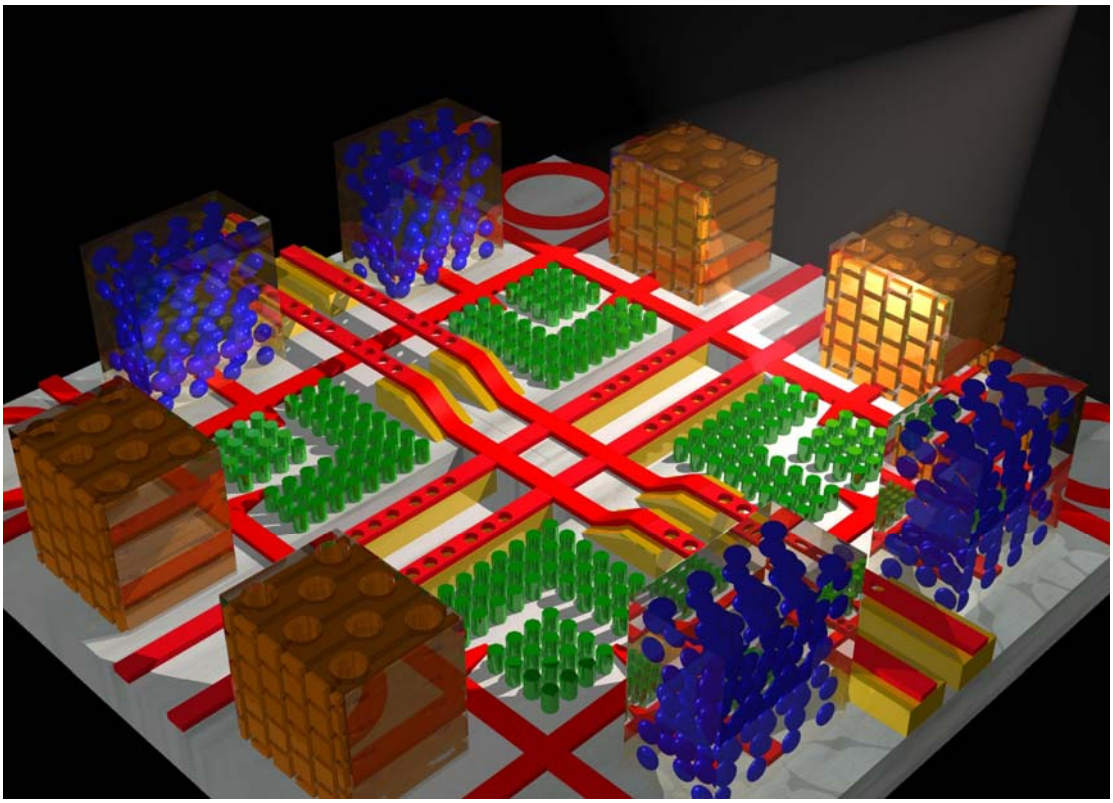

Fig. 1.4: Joannopoulu's photonic crystal micropolis—futuristic all optical chip.

1.4 Colloidal Crystals and Phononic Crystals

Phononic crystals are actually the phonon version of photonic crystals, thus the developments of photonic crystals have stimulated those of phononic crystals. In a photonic crystal, the band gap is caused by the periodic variation of the refractive index, while in a phononic crystal it is the variation of the elastic constants and/or the density that prohibits the propagation of acoustic waves within a specific frequency range.

Acoustic waves differ from light waves in the following two ways:

a) Acoustic waves are mechanical, thus they cannot travel through vacuum, whereas light waves are electromagnetic and can travel through vacuum. Mechanic waves are called acoustic waves when passing through a gas or liquid, and are called elastic waves when passing through a solid.

b) An elastic wave in a homogeneous solid has three independent polarizations: one is longitudinal (the displacement of the primitive basis from its equilibrium position coincidences with the propagation of the wave) and the other two are transverse (primitive basis moves perpendicular to its propagation wave), while the light wave has only two independent polarizations: transverse electric wave and transverse magnetic wave. Furthermore an acoustic wave has only longitudinal polarization, because shear waves cannot pass through gases or liquids.

The dispersion relation of the mechanic wave - plots of frequency, ω, versus wave vector, $\boldsymbol{k}$, in a homogeneous medium is very simple:

$$\omega = c \bullet k \tag{1}$$

here c is the velocity of sound in the medium, while the dispersion relation for materials like phononic crystals is complicated as shown in Figure 1.5, where the phononic band gap prohibiting the propagation of the wave in certain frequency region can be found in the yellow area.[24]

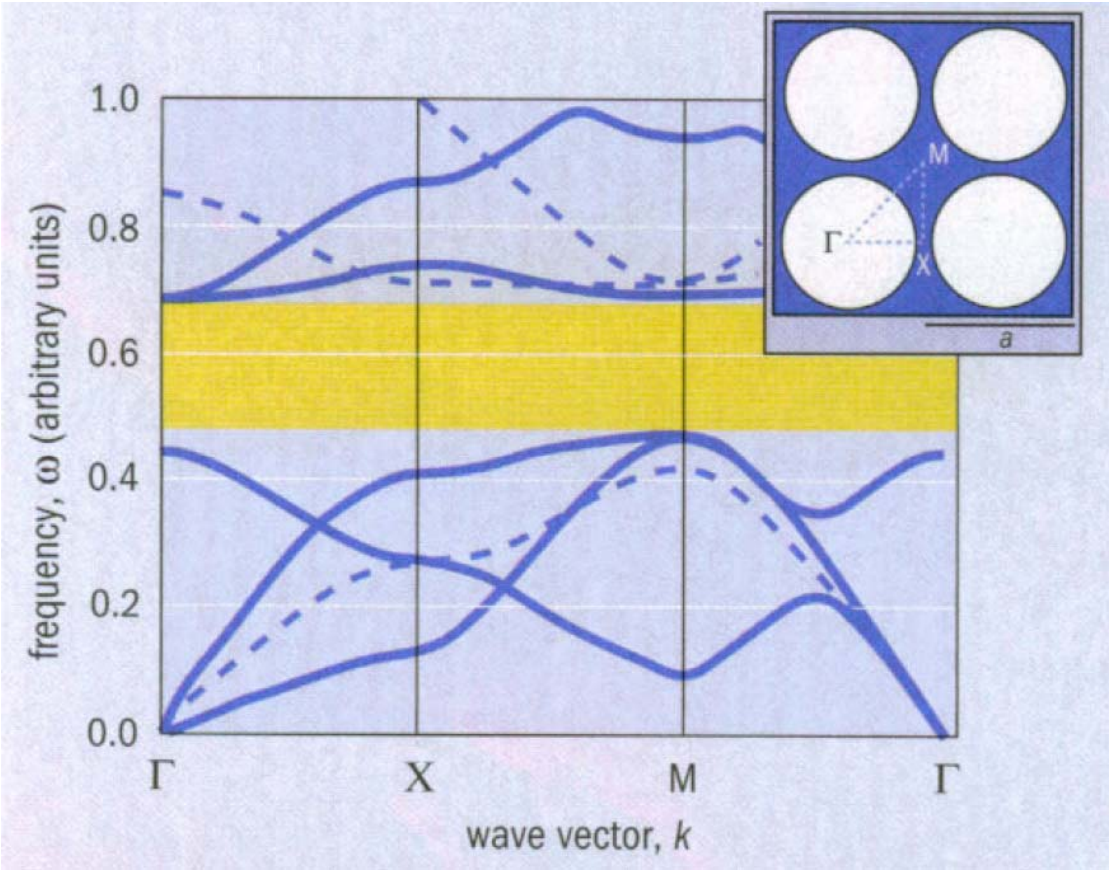

Fig 1.5: The dispersion relations for different phonons in the structure (insert - a 2D phononic crystal is made by fabrication of an array of air-filled cylinders in a solid material, thus the speed of sound changes periodically) shows forbidden of wave propagation within a specific frequency range (the yellow region).[24]

The lattice constant of colloidal crystals lies in the hypersonic region (wavelength less than 10μm or frequencies higher than100MHz). The behavior of hypersonic phonons has great impacts in solid-state physics. For example, the efficiency of the spontaneous emission of light in semiconductor materials is determined by the interaction between the electron and hypersonic phonon, as a consequence, high efficient semiconductor based light emitting devices can be fabricated if control over the phonon is realized. Phonons also determine the thermal conductivity of the dielectric material and of many semiconductors, thus phononic crystals which can manipulate the flow of phonons, have great impact in the thermoelectrics (the temperature gradient across the junctions of two dissimilar conductors causes the flow of the electrical current, and vice versa). As depicted previously, it is possible to make both the photonic and phononic crystals of the same

materials using colloidal crystals, which could lead to breakthroughs in the field of acousto-optics.[24]

1.5 Colloidal Crystals, 2D and 3D Patterned Structures

Photolithography is the technique most widely used for the fabrication of microstructures, but the method is intrinsically a planar technology, and its extension to 3D structures is limited to the stacking of planar sheets.[25-30] Inexpensive, simple, and conveniently self-assembled colloidal crystals offer possible routes to the fabrication of 2D and 3D microstructures.

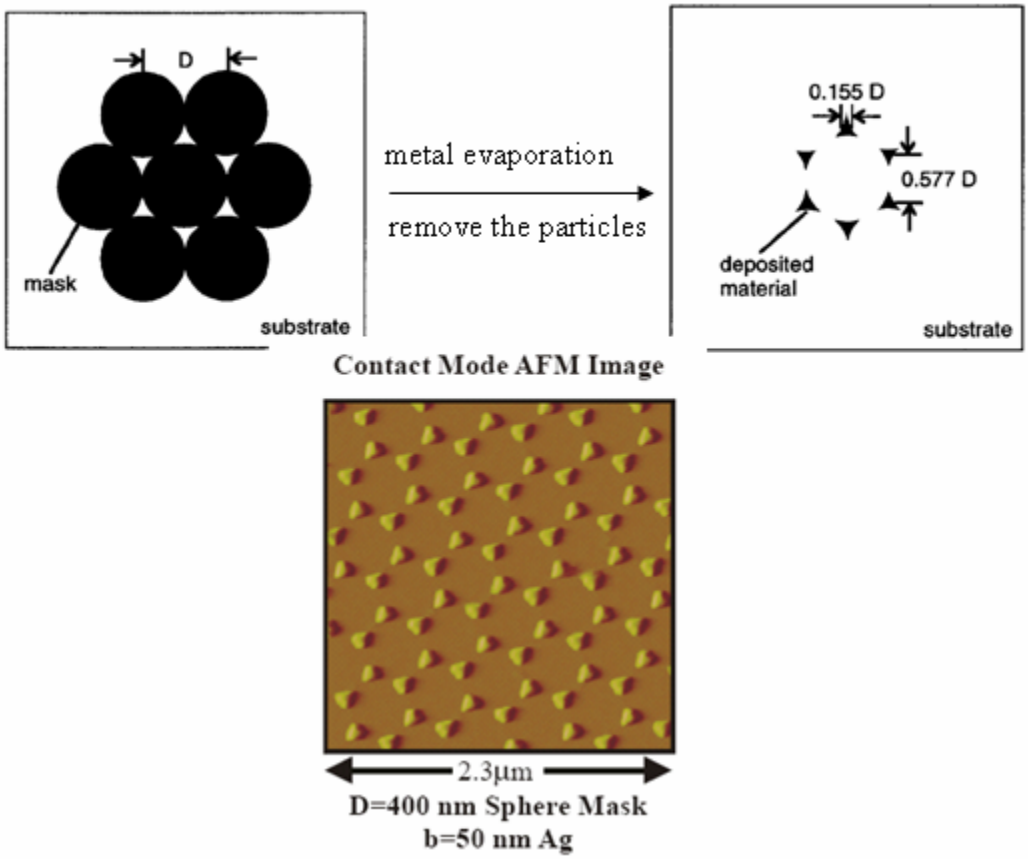

Fig 1.6: Scheme of the nanosphere lithography in which a 2D hexagonal monolayer of colloidal spheres is used as mask for selective deposition.(up) AFM image of an as-prepared hexagonal triangular silver dot array.

A triangular void space exists among the three physically contacted spheres, when the colloidal spheres assemble into a two dimensional close-packed monolayer on a solid substrate. Such kind of void arrays have been used as physical masks to

selectively deposit metals or dielectric materials onto the solid substrate as shown in Figure 1.6. As early as 1980s, Fisher and Zingsheim demonstrated this lithographic method to generate 2D arrays of nanostrutures.[31] This method coined as nanosphere lithography has been explored by a number of groups afterwards.[32-34] And the resolution of this methods has been extended to the scale of around 10nm by using proteins as the template.[35]

Another example is the fabrication of the macroporous materials with colloidal crystals as templates. Three dimensionally ordered macroporous (3DOM) materials are produced by combining colloidal crystals with suitable structure forming precursors, followed by removal of the colloidal crystal templates from the solid composite by chemical or thermal methods. The resulting product is a close-packed array of the air spheres in the former location of the colloidal sphere template with windows connecting the air spheres which is due to the former location of the contact points between the neighboring spheres. Such so called inverse opals are structures with well-defined porosity and may be particularly suitable for catalytic and sensor applications, as they provide a combination of efficient transport and high surface area.

1.6 Objective and Scope of Thesis

The main aim of the present work is to assemble monomodal colloidal crystals, binary colloidal crystals and trimodal colloidal structures with vertical lifting deposition. This method will also be employed to fabricate silica mono and binary inverse opals. Brilloiun scattering is employed to characterize the as-synthesized dry and wet monomodal colloidal crystals in the quest for the phononic band gap materials. Their applications in material science will also be explored by further process, such as electrochemical polymerization of the polyaniline in the colloidal crystal templates.

Chapter 2 presents the synthesis of the building blocks of colloidal crystals. Monodispersed colloidal particles with varieties of functional groups, different composition and particle size, were synthesized with surfactant free emulsion polymerization, miniemulsion polymerization and seeded emulsion polymerization. The interaction between the particles in suspension is briefly described.

Characterization methods, such as dynamic light scattering and scanning electron microscopy are compared.

The fabrication of monomodal colloidal crystals and binary colloidal crystals with vertical lifting deposition is demonstrated in chapter 3. The effects of varying the experimental parameters, such as the concentration, size of the particles, and temperature of the suspension on the assembly process of monomodal colloidal crystals are investigated. A detailed description of the formation of various lattice types depending on the size ratio and relative concentration between small and large particles during the synthesis of the binary colloidal crystals can be found in this chapter. Convenient growth of the silica inverse opal from the suspension of a mixture of polystyrene microsphere and silica nanoparticle by vertical lifting deposition followed by pyrolysis in ambient atmosphere is also shown.[36] Base on my knowledge on the fabrication monomodal colloidal crystals and binary colloidal crystals, vertical lifting deposition was further explored to prepare trimodal colloidal crystals and their binary inverse opals. The optical properties of the prepared monomodal, binary, trimodal colloidal crystals and mono, binary inverse opals were characterized by the Vis-NIR spectroscopy, and the spectral shifts are analyzed to deduce the lattice composition of trimodal colloidal structures. The result agrees well with that from the computer modeling.[37]

In addition to vertical lifting deposition, a spotting technique was employed to produce colloidal crystal microarrays comprising of up to *9600* single colloidal crystal structures with dimensions down to 100 μm on microfabricated substrates. Optical properties of the colloidal crystal microarrays were characterized in parallel by reflection spectroscopy.[38] A new method called vertical cell lifting method was also investigated to fabricate thick silica nanoparticle array films. As such, this method has potential to assemble thick nanoparticle (such as quantum dots, magnetic paticles) films, which are useful for device applications. All these results will be discussed in chapter 3.

In chapter 4, measurements of the particle vibrational eigenmodes in the synthesized monomodal colloidal crystals by Brillouin light scattering are reported. Here the particle size ranged from 187nm to 856nm revealing up to 21 eigenmodes, and all the eigenmodes are captured by theoretical calculation.[39] We observed experimentally the phononic band gap in thin films formed by self-assembled polystyrene microsphere colloidal crystals with subsequent fluid infiltration. The

frequency and the gap width could be tuned by adjusting the contrast of sound speed between the polystyrene particles and the infiltration matrix with simply exchanging the liquids. The tuning of the gap width was also realized by varying the lattice constant, in our case the particle size. [40]

Chapter 5 concentrates on the preparation of inverse opals of polyaniline (PANI) by electrochemical polymerization with polystyrene colloidal crystals as sacrificial templates. In order to explore the potential in biosensing applications, PANI composite inverse opals were fabricated with different dopants, such as polyacrilic acid (PAA), and polystyrene sulfonate (PSS). It was found that these dopants had major effects on the structure and mechanically stability of the obtained films. The synthesized PANI composite inverse opals remained electroactive in neutral pH. The preliminary application of such films as electrocatalysts for the oxidation of the reduced β-nicotinamide adenine dinucleotide (NADH) showed the increment of the electrocatalytic efficiency in the inverse opal film by one order of magnitude compared with the unpatterned film due to the increase of the effective surface area.[41]

Chapter 5 also includes the preparation carbon nanoparticles with controllable hierarchical structures using silica inverse opals as templates in combination with the precursor defined pyrolysis (PDP).[42] Silica inverse opals were further used for the preparation of gold / silica inverse opals, and gold porous sphere arrays were obtained by the removal of silica scaffold.

References

1 Xia YN, Gates B., Yin YD, Lu Y, *Adv. Mater.* **2000**, *12*, 693.

2 Sanders J. V. *Nature* **1964**, *204*, 1151.

3 Hachisu S., Kobayashi Y., Kose A., *J. Colloid Interf. Sci.* **1973**, *42*, 342.

4 Pusey P. N., Van Megen W., *Nature* **1986**, *320*, 340.

5 Yethiraj A., Van blaaderen A., *nature* **2003**, *421*, 513.

6 Kegel W. K., Van Blaaderen A., *Science* **2000**, *287*, 290.

7 Pham k. N., *Science*, **2002**, *296*, 104.

8 Shebton W., Pum D., Sleytr U., *Nature* **1997**, *389*, 585.

9 Guarini K. W., Black C. T., Yeung S. H., *Adv. Mater.* **2002**, *14*, 1290.

10 Redl F. X., Cho K. S., Murray C. B., O'Brien S., *Nature* **2003**, *423*, 968.

11 Joannopoulos J. D., Villeneuve P. R., Fan S., *Nature* **1997**, *386*, 143.

12 Yablonovith E., *Sci. Am.***2001**, *285*, 34.

13 Lopez C., *Adv. Mater.* **2003**, *15*, 1679.

14 http://www.*ab-initio.mit.edu/photons/tutorial/*

15 Haus J. W. ,Sozuer H. S., Inguva R., *J. Mod. Opt* **1992**, *39*, 1991.

16 Li Z. Y., Wang J., Gu B. Y., *Phys. Rev. B* **1998**, *58*, 3721.

17 Colvin V. L., *MRS Bulletin* **2001**, *Augst*, 637.

18 Biswas R., Sigalas M. M., Subramania G., Ho K. M., *Phys. Rev. B* **1998,** *57*, 3701

19 Busch K., John. S., *Phys. Rev. E* **1998**, *58*, 3896.

20 Weissman J. M., Sunkara H. B., Tse A. S., Asher S. A., *Science* **1996**, *274*, 959.

21 Reese C. E., Baltusavish M. E., Kein J. P., Asher S. A., *Anal. Chem.* **2001**, *73*, 5038.

22 Cassageau T., Caruso F., *Adv. Mater.* **2002**, *14*, 1629.

23 Sumioka K., Kayashima H., Tsutsui T., *Adv. Mater.* **2002**, *14*, 1284.

24 Gorishnyy T.,Maldovan M.,Ullal C., Thomas E. L. *Physics World* **2005,** *18*, 25.

25 http://public.itrs.net/files/2003ITRS/Home2003.htm

26 Switkes M, Kunz R. R., Rothschild M,. Sinta R. F., Yeung M., Baek S. Y., *J. Vac. Sci. Technol. B* **2003**, *21*, 2794.

27 Owa S., Nagasaka H., *J. Microlith. Microfab. Microsys.* **2004**, *3*, 104.

28 Switkes M., Rothschild M., *J. Vac. Sci. Technol. B* **2001**, *19*, 2353.

29 Montcalm C., Grabner R. F., Hundyma R. M., Schmidt M. A., Spiller E.,Walton C. C.,Wedowski M., Folta J. A., *Appl. Opt.* **2002**, *41*, 3262.

30 Hoffnagle J. A., Hinsberg W. D., Houle F. A., Sanchez M. I., *J. Photopolym. Sci. Technol.* **2003**, *16*, 373.

31 Fisher Y. C., Zingsheim H. P., *J. Vac. Sci. Technol*. **1981**, *19*, 881.

32 Hulteen J. C., Duyue R. P. V., *J. Vac. Sci. Technol*. **1995**, A*13*, 1553.

33 Roxlo B. C., Deckman H. W., Gland J., Cameron D. S., Chianelli R. R., *Science* **1987**, *235*, 1629.

34 Green M., Garcia-Parajo M., Khaleque F., *Appl. Phys. Lett*. **1993**, *62*, 264.

35 Douglas K., Devaud G., Clark N. A., *Science* **1992**, *257*, 642.

36 Wang J., Glasser G., Neumann T., Knoll W., Jonas U., submitted to *Adv. Mater.* **2006.**

37 Wang J., Li Q., Knoll W., Jonas U., *submit to J. Am. Chem. Soc.* **2006**.

38 Burkerta K., Neumanna T., Wang J., Jonas U., Knoll W., Ottlebenc H., *submitted to Langmuir* **2006**.

39 Cheng W., Wang J., Jonas U., Fytas G., Penciu R. S., Economou E. N, *J. Chem. Phys.* **2005**, *123*, 121104.

40 Cheng W., Wang J., Jonas U., Fytas G., Stefanou N., *Nature Materials* **2006**, *5*, 830.

41 Tian S., Wang J.，Jonas U.， Knoll W.， *Chem. Mater*. **2005**, *17*, 5726.

42 Zhi L., Wang J., Cui G., Kastler M., Schmaltz B., Kolb U., Jonas U., Müllen K., *submitted to Adv. Mater.***2006**.

Chapter 2 Synthesis of Nano- and Microspheres

2.1 General

Numerous chemical methods can be used for the preparation of monodispersed colloidal particles.[1] The Stöber procedure is widely employed for preparing amorphous monodispersed silica colloids,[2] where dilute solution of tetraethylorthosilicate (TEOS) is hydrolyzed in ethanol, and monodispersed colloidal spheres, cubes, ellipsoids and rods could be produced. The reaction conditions are precisely controlled, such as the pH, the temperature, the method for mixing the reactants, the concentration of reactants, and the concentration of counter ions so that the particle nucleation and the growth are strictly separated and nucleation is avoided during the particle growth, thus the LaMer rule for the synthesis of the monodisperse colloidal particles is met.[3]

The size range of the synthesized silica colloids can be varied from 50nm to 2μm by simply changing the concentration of the reactants. The surface of the silica particles inheritly has the silanol groups (-Si-OH), and can be further functionalised by siloxanes.[4] Other materials such as metal sols,[5] quantum dots,[6] and organic chromophores[7] can be incorporated into the particles for different kinds of applications.

Polymer latex with large size range and different chemical composition is prepared in aqueous medium by a host of techniques. Overview of various polymerization techniques is listed in table 2.1.[8]

Table 2.1 Overview of various polymerization techniques in aqueous medium[8]

Method	**Initiation**	**Stabilizer**	**Procedure**	**Particle Size**
suspension	hydrophobic	small amount of surfactants	batch	10~500μm
emulsion	hydrophilic	surfactants or none	batch, semi-batch, continuous, seeded	50nm~10μm
miniemulsion	hydrophobic	surfactants	batch, semi-batch, continuous,	50~500nm
microemulsion	hydrophobic	surfactants	batch, semi-batch,	10~100nm

Table 2.2 Principles of stabilization of colloidal particles[9]

Stabilization	Acting forces	Important parameters
Electrostatic	Electrostatic repulsion of equally charged particles; repulsive potential (V_R) around charged particles at distance (d) decays as: $V_R \propto f(\psi)\exp(-\frac{d}{\lambda_D})$	Charge density at the interface, surface potential (ψ), ionic strength (I_S); Debye screening length (λ_D) $\lambda_D = \left(\frac{\varepsilon \cdot \varepsilon_0 \cdot \kappa_B T}{\sum_i (z_i \cdot e)^2 \cdot C_{salt}} \right)^{0.5}$
Steric	Osmotic and entropic forces between overlapping stabilizer layers of approaching particles $V_R \propto \frac{C_{S,L}^2}{v_{C,P} \cdot \rho_{S,L}^2} \cdot (\psi - \chi_{S,Cp}) \cdot \left[\left(\Delta R - \frac{d}{2} \right)^2 \left(\frac{3D}{2} + 2\Delta R + \frac{d}{2} \right) \right]$	Solution state of stabilizing polymer molecules (interaction parameter between polymer and stabilizing polymer and continuous); temperature, ionic strength as far as both inference the solution state of the lyophilic polymer
Electrosteric	Competition between the osmotic pressure induced by counterion condensation inside the polyelectrolyte corona, which stretches the polyelectrolyte chain into the aqueous phase, and entropic polymer elasticity, which pulls the chains back the surface, $\Delta R \propto I_S^a; a = -1/5$	Ionic strength, conformation and c charge density of the polyelectrolyte chain, ration corona thickness to particle diameter (D); corona shrinks upon increasing ionic strength.

Note: C_{salt} is the molar bulk concentration of the ions, k_BT is the thermal energy, ε and ε_0 are the permittivities in the continuous phase and vacuum, z is the stoichiometric valency of the electrolyte, and e is the elementary charge; $C_{S,L}$ is the concentration of lyophilic polymer per unit volume inside the corona; v_{cp} is the molar volume of the continuous phase, $\rho_{S,L}$ is the density of the lyophilic polymer, ψ_1 is the an entropy parameter for mixing of the overlap region, and $\chi_{S,cp}$ is the interaction parameter between the lyophilic polymer and the dispersion medium.

With the methods listed in table 2.1, polymer latexes can be specifically designed with regard to mechanical properties, particle size, interfacial properties and volume properties. For application in colloidal crystallization, individual particles are required in a colloidal suspension so that a large area of close packed colloidal crystal can be obtained. Therefore, the particle-solution interaction is a vital parameter. Interfacial properties can be varied by the kind of stabilizer, initiator, and co-monomer. Three kinds of interfacial forces are normally explored to counteract the attractive van der Waals force, i.e. electrostatic, steric, and eletosteric forces. Each of these forces contributes to the particle stability. Table 2.2 summarizes principles of the particle stabilization by these interactions.[9] Electrostatic stabilization is realized via application of ionic or cationic initiator, for example, negative changed particles can be prepared with potassium persulfate as initiator, and positive changed particles can be prepared with 2,2'-azobis(2-amidinopropane) dihydrochloride as initiator. Low molecular weight ionic surfactants such as sodium dodecylsulfate, and alkyl ammonium compounds such as cetyltrimethylammonium bromide are also used to realize electrostatic stabilization. But a disadvantage of the electrostatic stabilization is that it decreases exponentially with the added electrolyte concentration. Also, the ionic strength changes considerably during the storage and application of water based colloidal particle, therefore resorting to other kinds of stabilization is required during the storage and application of aqueous dispersions

In contrast, steric stabilization is insensitive to the electrolyte concentration, and the agregation process is reversible when the polymer stabilizer adheres strongly or covalently bound to the colloidal particles. Electrosteric stabilization is the combination of electrostatic and steric stabilization, which can be realized by the addition of polyelectrolytes when the particles have been synthesized or with ionizable comonomers during the preparation of the polymer latex.

In addition to the interfacial properties, the size and size distribution of the polymer particles are also crucial in colloidal crystallization. Generally, a particle size distribution (PSD) less than 5% is required. In our lab, surfactant free emulsion polymerization, seeded emulsion polymerization, and mini-emulsion polymerization are used for the synthesis of monodisperse polymer particles with sizes ranging from several tens of nanometers to several micrometers. A typical reactor is shown in Figure 2.1.

Fig. 2.1: Typical reactor used in the lab for the preparation of polymer latex

All these three methods belong to free radical polymerisation. The reaction begins with the decomposition of initiator to produce free radicals, which reacts with monomers. This step is called initiation shown here:

$$I \rightarrow 2R\bullet$$
$$R\bullet + M \rightarrow RM_1\bullet$$

Generally the initiation efficiency $f < 1$, because once the initiating radicals are formed, there is a competition between the addition to monomers and all other possible secondarly reactions.

The initiation is followed by the propagation, where the free radicals react with the monomer. Because of steric factors and radical stabilization by conjugation normally the head-to-tail addition is more probable as shown below:

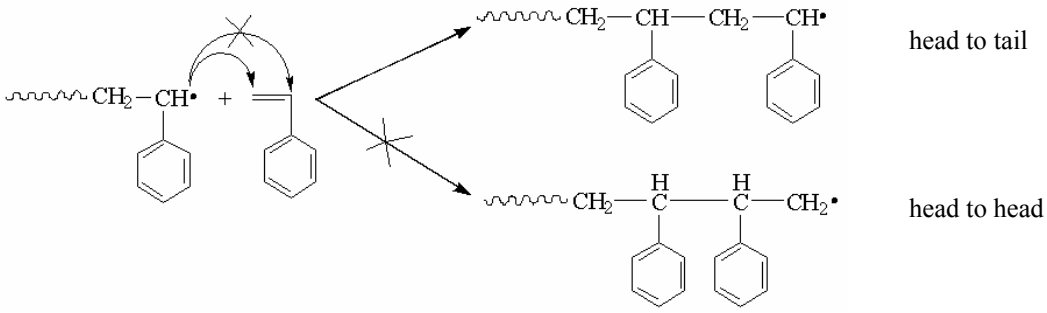

Finally, the reaction is terminated mainly by two ways, namely: recombination and disproportionation. Recombination refers to two free radicals meeting and forming one head-to-head chain with double length and molecular weight:

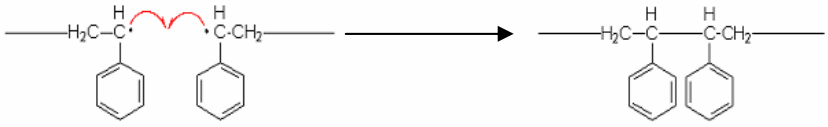

disproportionation refers to two radicals meeting, and an electron in one radical abstracting a hydrogen in the other radical, resulting in two chains with different end group and negligible change in molecular weight:

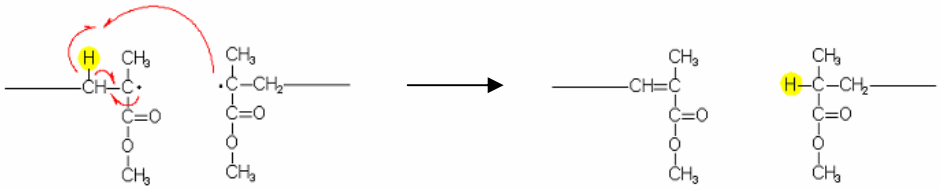

Termination can also occur by transferring the active centre to another molecule, which may be a polymer, monomer, initiator, or solvent molecule. For the synthesis of polymer particles, functional groups can be introduced by addition of chain transfer agents (CTA).

2.2 Surfactant Free Emulsion Polymerisation

Surfactant free emulsion polymerization stands out among other techniques because the particles prepared have lower size distribution and are easier to be purified than the particles prepared with other methods. Surfactant free emulsion polymerization has been widely described in the literature since Matsumoto *et al* first reported this technique in 1965[10]. Mainly three kinds of mechanisms,[11] i.e. homogeneous nucleation, oligomer micellization, and a coagulation mechanism, have been proposed to explain the formation of stable polymer particles without emulsifier. Normally one of the following reactant components is used in a reaction for the system to obtain colloidal stability:

a) Ionizable initiators, such as potassium persulfate and 2, 2'-azobis(2-amidinopropane) dihydrochloride.

b) Hydrophilic comonomers, such as PEG macromolecular monomers.

c) Ionic comonomers, such as acrylic acid.

Similar to the conventional emulsion polymerization, surfactant free emulsion polymerization can be divided into three stages:

Stage 1: in this stage, nucleation of the polymer particles occurs, when oligomer radicals (actually such oligomer radicals behave similar to that of surfactants with their hydrophilic heads and hydrophobic tails.) aggregate to form micelles. The system is characterized by the increase of the particle number and particle size. For the surfactant free emulsion polymerization, this stage is shorter compared with the conventional emulsion polymerization, which leads to narrower particles size distribution.

Stage 2: is the particle growth stage. It begins when the nucleation of the polymer particles is complete. It is characterized by the constant particle number, constant monomer concentration in the polymer particle, and increase of the particle size.

Stage 3: this stage begins when monomer droplets disappear in the dispersion. In this stage, the polymer particle number keeps constant while the concentration of monomer in the polymer particle decreases.

The dependence of D (particle size) on the ionic strength ([I] between 0.88 and 50mM), monomer concentration ([M] between 0.58 and 0.87M), potassium persulfate ([P] between 0.29 and 0.29 and 2.76 mM), and the temperature (T in K between 60 and 95) is described by equation 1, which is summarized by Goodwin et al based on the comprehensive experimental data obtained in their lab:[12]

$$\log = 0.238\left[\log\left(\frac{[I][M]^{1.723}}{[P]}\right)+\frac{4929}{T}\right]-0.827 \qquad (1)$$

Precautions must be taken when using equation (1), because the polymerization hardware has an influence on the results of the emulsion polymerization, for example, the reactor material, reactor geometry and hydrodynamic conditions have effects on the particle size and size distribution. Moreover, the particles synthesized with the same recipe but with chemicals from different companies or from the same company but different batches lead to different particle size.

In practice, particle size can be easily controlled by the concentration of the initiator, ionic strength, and the concentration of the ionisable comonomer. Shouldice et al summarized the dependence of the polystyrene particles size on the concentration of initiator and the concentration of ionisable comonomers as shown in Figure 2.2.[13] It

can be seen from Figure 2.2 that the particle size increases with the concentration of the initiator and ionic strength, and decreases with the concentration of the SSA comonomer within a specific range. These data demonstrate that practical strategies for the synthesis of polymer particles by varying the concentration of initiator, ionic strength, and the concentration of ionic comonomer.

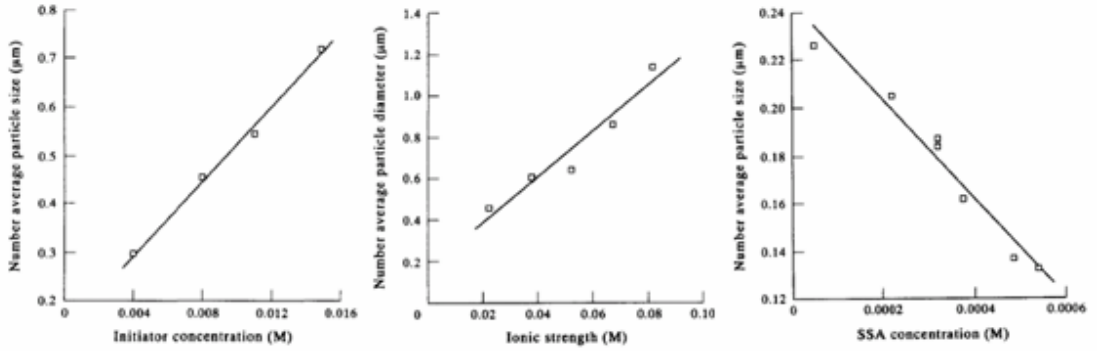

Fig. 2.2: Left: A plot of the particle size against the initiator concentration, reaction temperature was 75°C, ionic strength was not controlled. Center: A plot of the particle size against the ionic strength, reaction temperature was 85°C. Right: A plot of the particle size against the styrene sulfonic acid (SSA) sodium salt concentration, reaction temperature was 80°C.[13]

With the reactor in our lab, monodisperse polymer particles (PSD less than 5%) have been synthesised, and the particle size could be conveniently varied with the above mentioned strategies. One example is shown in Figure 2.3. The SEM image shows the PS particles with PSD=2.3% from DLS. And Table 2.3 is a representative recipe.

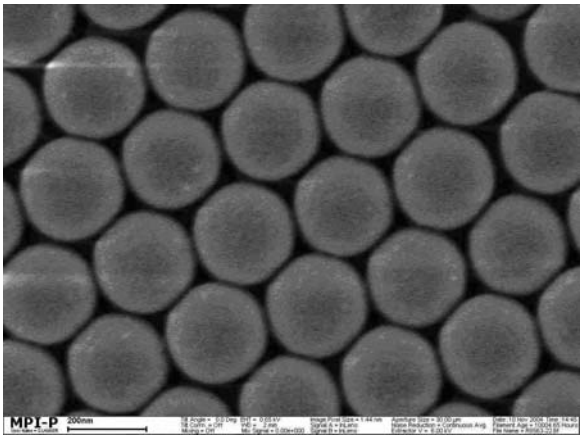

Fig. 2.3: Polystyrene particles prepared by surfactant free emulsion polymerization, D=256nm (SEM), 271nm (DLS). PSD is 2.3% from DLS.

Table 2.3: Representative recipe for the surfactant free emulsion polymerisation.

particle batch	JW PHD 102
batch	300g H_2O, 15.43 St, 0.11g APS(in 10mL H_2O), 0.15g AA, 0.034g NaSS
stirring speed	300rpm
temperature	80°
reaction time	24hrs
size(LS)	205nm
poydispersity	0.01

Note: St is styrene, APS is ammonium persulfate, AA is acrylic acid, NaSS is sodium styrene sulfonate.

2.3 Seeded Emulsion Polymerisation

It is highly desirable to control the placement of monomer or functional groups for various applications such as colloidal stability, surface functionality, post-reaction and medical diagnostics. Seeded emulsion polymerisation is a powerful tool to prepare tailored latex particles with expected layered morphology.

Seed particles are first prepared with other polymerisation techniques, and used as nucleus in the seeded emulsion polymerisation, therefore conditions can be chosen to start the polymerisation in stage 2 or stage 3 which was described in the previous section. If the monomers are added to the dispersion with all seed particles as a second batch, and the monomer is a good solvent for the seed polymer so that the seed particles are swollen with the monomers, then the polymerisation starts in stage 3. The morphology of the produced particles is determined by many effects, such as the size of the seed particles, the degree of cross linking of the seed particles, the amount of monomer added in the second stage and also the interfacial tension between the seed polymer, the polymer formed by the monomer added later and the dispersion medium.[14] The addition of monomers can also be performed in such a way that the feed rate is slower than the rate of polymerisation. This is the so-called semi-continuous monomer-starved emulsion polymerisation, which leads to the core/shell polymer morphology, because the second polymer phase is only allowed to nucleate and grow on the surface of the seed particles.

The final particle size synthesized by the seeded emulsion polymerisation is determined by equation (2), where V_{feed} is the total volume of the fed monomer, V_{seed} is the total volume of seed polymer, and N_{seed} is the number of seed particles.[15]

$$D = \left[\left(V_{feed} + V_{seed} \right) \cdot \frac{6}{\pi} \cdot \frac{1}{N_{seed}} \right] \qquad (2)$$

With the semi-continuous monomer-starved seeded emulsion polymerization, I have synthesised polyethylene glycol (PEG) capped polystyrene microspheres. Table 2.4 is the recipe and Figure 2.4 is the SEM image of the synthesized particles. Functional groups (PEG) were placed mostly on the surface of polystyrene seeds. In the SEM image at left side of Figure 2.4, there are necks between particles, which should be formed by the hairy PEG macromoleculars.

Table 2.4: recipe of the PEG capped PS particles with seeded emulsion polymerization

batch	core (JW PHD 152)	shell (JW PHD 153)
feed1	300g H_2O 15.4g St 0.034g NaSS 0.03g PEG	50g core 250g H_2O 16g St 0.5g PEG (MW 2080)
feed2	0.11g APS in 10ml H_2O	0.93g APS in 20g H_2O
stirring speed	300rpm	150rpm
temperature	80℃	80℃
reaction time	24hrs	24hrs
size (LS)	223nm	367nm
polydisperisty	0.01	0.02

Note: St is styrene, APS is ammonium persulfate, PEG is polyethylene glycol methyl ether methacrylate(MW 2080), NaSS is sodium styrene sulfonate.

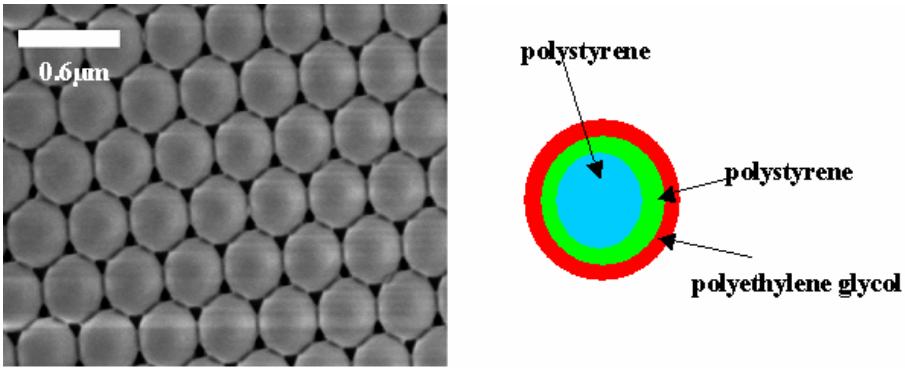

Fig: 2.4: SEM image of the PEG capped PS particles (left), and scheme of such particles (right).

The ability of the as-synthesized PEG capped polystyrene particles in resisting nonspecific protein adsorption is compared with that of the plain PS particles and poly-L-lysine-*g*-poly (ethylene glycerol) (PLL-*g*-PEG) (from Prof. Markus Textor's group in Zurich) capped polystyrene particles where the PLL-*g*-PEG is attached to PS particle surface by the coulomb force because the PLL-*g*-PEG and the PS are oppositely charged at pH 7.4, and also with that of PEG-*co*-PS plus 1% polyoxyethylene (20) sorbitan monolaurate (Tween 20) which is added to make sure that the surface is really saturated with PEG. The results are shown in Figure 2.5 where the Alexafluo-543 labelled straptavidin has been used to check the adsorption resistant ability of different particles with the confocal laser scanning microscopy (CLSM). The images in Figure 2.5 demonstrate that all the PEG-capped particles have comparable strong ability in resisting nonspecific protein adsorption, which means that the PEG in PEG-*co*-PS particles stays mostly on the surface of the PS particles.[16]

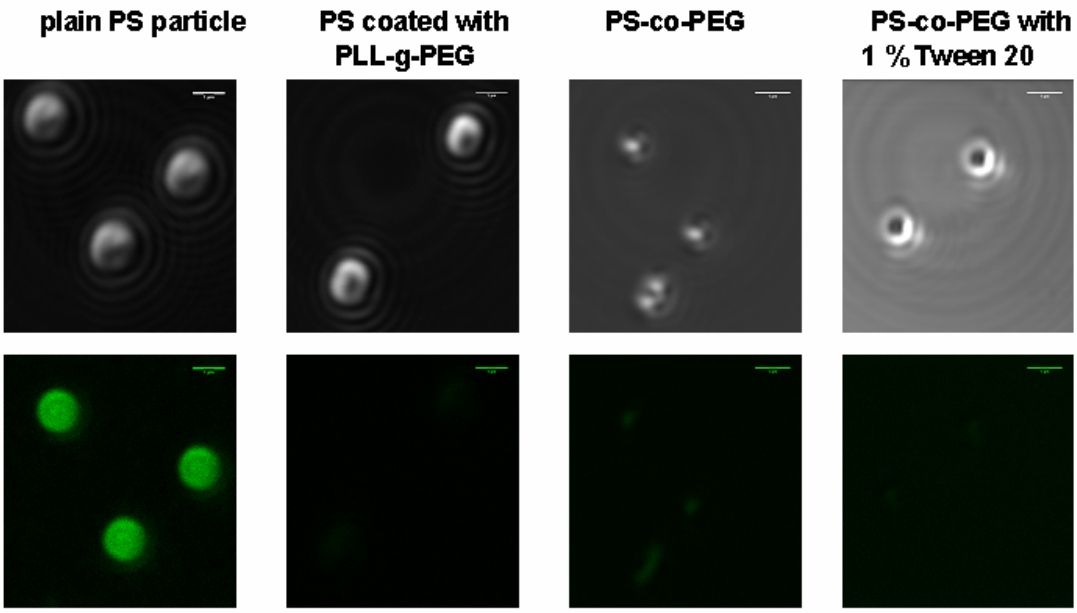

Fig. 2.5: Reflective mode (upper row) and fluorescence mode (lower row) images of the different PEG capped particles stained with Alexafluo-543 modified Straptavidin on the surface. In the fluorescent mode images only the plain particles are visible by strong emission which shows that all the PEG capped particles have the comparable ability in resisting the adsorption of stained proteins. The scale bar is 1 micron.

2.4 Mini-emulsion Polymerisation

In conventional emulsion polymerisation, the initiation and following polymerisation take place in monomer swollen micelles, with the initiation first occuring in the aqueous medium, then according to the homogenous nucleation mechanism, a new polymer phase swollen with monomer is produced in the dispersion medium, which is the main locus for the following polymerisation. The monomer droplets in both cases are ruled out as the main loci for polymerisation, because the surface area of the monomer droplets is considerably smaller than that of the monomer swollen micelles. While in the miniemulsion polymerization, the size of monomer droplets (from several tens of nanometers to several hundreds of nanometers) is much smaller than that of the conventional emulsion polymerization (several microns). In addition, the initiator in miniemulsion polymerizatin is oil soluble. Therefore miniemulsion polymerisation can be regarded as a special suspension polymerisation, where the main polymerization loci are in the monomer droplets, and the precursor particles are preserved during polymerization, which provides a tool to incorporate other guest materials in the synthesized particles.

To create a miniemulsion, surfactants such as SDS are added to provide electrostatic or steric stabilisation of the precursor particles and ultrahydrophobes such as hexadecane are used to counteract Oswald ripening (the growth of the particles with the expenditure of the smaller particles) by the osmotic pressure in the droplets. Furthermore high energy is also required to overcome the difference in surface energy $\gamma \Delta A$ (γ is the interfacial tension, and ΔA is the area of the newly formed interface) and form the finely dispersed oil droplets. Generally, an ultrasound or homogeniser is used for the emulsification.

Table 2.5 is a representative recipe of the miniemulsion polymerisation, where particle size can be easily altered by adjusting the surfactant concentration and also the sonification time.

Table 2.5: A representative recipe of the miniemulsion polymerization.

particle batch	JW PHD 109
batch	50g H_2O, 30g MMA, 0.5g HD 5.4g SDS 0.3g AA 0.1g AIBN
stirring speed	360rpm
temperature	72℃
reaction time	12hrs
size (LS)	65nm
polydispersity	0.08

Note: MMA is methyl methacrylate, HD is hexadecane, SDS is the sodium dodecylsulfate, AA is acrylic acid, AIBN is azobisisobutyrol nitrile.

With the miniemulsion polymerization, polystyrene particles embedded with rylene dyes (from Prof. Muellen's group at MPIP) were prepared, Figure 2.6 shows that the particles show fluorescence, and the PSD of the particles obtained is 3% from DLS.

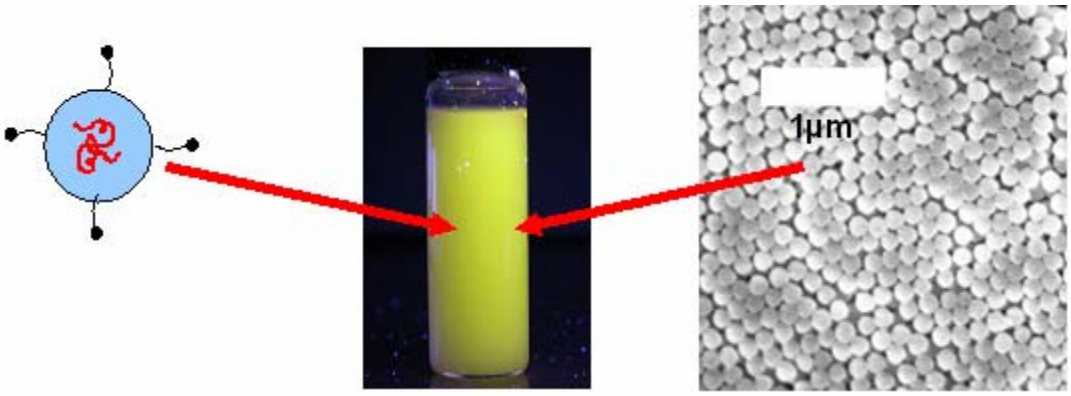

Fig 2.6: Rylene contained polystyrene particles, scheme of the particle with rylene dye (left), suspension of the rylene particles exhibits yellow fluorescence because the rylene dye (middle), and SEM image of the particles reveals that the particles are monodisperse (right).

2.5 Characterization of Particles

For the colloidal crystallization, the most significant characteristics of the colloidal dispersions are the size and size distribution. Although the majority of

colloidal dispersion of scientific and technological interest are composed of particles that differ tremendously in size, and may have irregular shapes, particles synthesised by the previously described three polymerisation methods are normally spherical and their size distribution is reasonable narrow (monodisperse). Dynamic light scattering and scanning electron microscopy are used to probe the particle characteristics.

2.5.1 Dynamic Light Scattering (DLS)

When a light photon enters the colloidal dispersion, the oscillating electrical field induces transient oscillating dipoles in the molecules of the colloidal particles, which can re-emit light by themselves. The colloidal particles in suspension are always moving because of the continuous collisions of the dispersion molecules with the particles - the famous Brownian motion, and when the monochromatic light hits a moving particle, the scattered light is energy-shifted by the transactional energy of the particle, so it is not monochromatic any more, which is called Doppler broadening (more about light scattering can be found in chapter 4).

In dynamic light scattering, DLS, or quasi-elastic light scattering, QELS, or photon correlation spectroscopy, PCS, not only the intensity I ($w_0 + w$) but also the frequency spectrum ($w_0 + w$) of the scattered light at specific angle are accurately measured. The intensity and the frequency can be expressed by equation (3):

$$I_{\Theta}(\omega_0 + \omega) = I_0 \frac{D\left|\vec{K}\right|^2}{\left[D\left|\vec{K}\right|^2\right]^2 + \omega^2} \tag{3}$$

w_0 is the frequency of the incident light, and the scattering wave vector $\vec{K}$,

$$\left|\vec{K}\right| = 4\pi/\lambda_0 \sin\frac{\Theta}{2} \tag{4}$$

The plot of *I* against *w* is called a Lorenz curve:

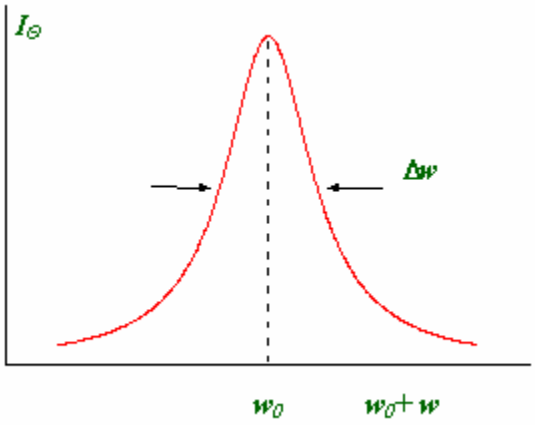

Fig. 2.7: The spectrum of the light scattered at some angle Θ

The characteristic width of the Lorenz curve is,

$$\Delta\omega \propto D\kappa^2 \propto \left(16\pi^2 D/\lambda_0^2\right)\sin^2\frac{\Theta}{2} \tag{5}$$

here D is the diffusion coefficient, which is related to the thermal energy *kT*, viscosity of the solvent η and hydrodynamic radius of the particle R:

$$D = \frac{kT}{6\pi\eta R} \tag{6}$$

Thus R can be calculated with equation (6), when the D, T, and η are known.

For more information about light scattering, please refer to book edited by Berne Bruce.[17]

The particle size measured for DLS is the hydrodynamic radius. The particles in dispersion always carry some solvent molecules (called hydration when the dispersion medium is water), thus size measured from the DLS is normally larger than the data from SEM (the measurement normally is carried in vacuum state) (will be described below) which is almost equal to the real core size.[18]

In our lab I used Zeta Sizer 3000HS from Malvern Instrument Ltd to measure the particle size and size distribution.

2.5.2 Scanning Electron Microscopy

In the scanning electron microscope, the electron beam, which is focused to a diameter of about 5-10nm, scans over the surface of the sample. The various interactions of the electron beam with the sample are depicted in Figure 2.9. The incident electron passing close to the sample atoms can ionize an electron (inelastic process). Ionized electrons leaving the sample with very small kinetic energy (5eV) are called secondary electrons, which are topography related. The backscattered electron beam is caused by the direct collision of the incident electrons with the sample atoms and scattering backward at angle of 180 degrees ('elastic' process). The amount of backscattered electrons varies with the atomic number - higher atomic number elements appear brighter (or scatter more effectively) than lower atomic number elements, thus the resulting image shows elemental contrast. A dedicated detector collects these secondary or backscattered electrons. The output from the detector is used to modulate the intensity of the electron beam and thus images can be reconstructured.

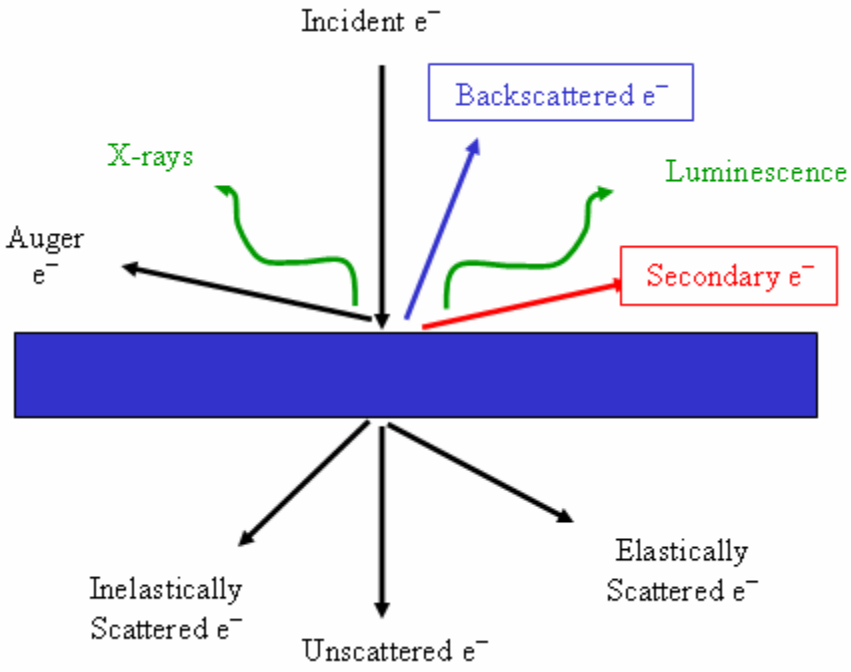

Fig 2.8: Scheme of the interaction of the electron beam with the sample

If the instrument is coupled to a solid state X-ray detector, so that the intensity and wavelength of the characteristic X-ray emitted by the surface atoms can be determined, it is also possible to provide the detailed information on the surface composition of the sample.[19]

Low-voltage scanning electron microscope (LV-SEM) images on native samples (non-sputtered) were taken with a LEO Gemini 1530 at acceleration voltages of 0.2-1kV and normally the diameter of at least 200 particles were measured to confirm the data obtained from DLS.

References

1 *Fine Particles* (Ed. Matijevic), a special issue in *MRS Bull.* **1989**, *14*, 18.

2 Stoeber W., Fink A., *J. Colloid interface Sci.***1968***, 26,* 62.

3 a) Zaiser E. M., LaMer V. K., *J. Colloid Interface Sci.***1948**, *3*, 571. b) V. K. Lamer, *Ind. Eng. Chem*. **1952**, *44,* 1270.

4 Ueda M., Kim H.-B., Ichimura K., *J. Mater. Chem*. **1994**, *4*, 883.

5 Yu A, Meiser F, Cassagneau T., Caruso F., Nano Lett. **2004,** *4*, 177.

6 Wang D.,. Rogach A. L, Caruso F., Nano Lett. **2002,** *2*, 857.

7 Xia YN, Gates B., Yin YD, Lu Y., *Adv. Mater*. **2000,** *12***,** 693

8 *Colloids and Colloid Assemblies* (Ed. F. Caruso), **2003**, P4.

9 *Colloids and Colloid Assemblies* (Ed. F. Caruso), **2003**, p13.

10 Matsumoto T., Ochi A., *Kobunshi Kagaku* **1965**, *22*, 481.

11 Wang Q., Fu S., Yu T., *Prog. Polym. Sci*. **1994**, *19*, 703.

12 Goodwin J. W., Hean J., Ho C. C., Ottewill R. H., *Coll. Polm. Sci*. **1974**, *252*, 464.

13 Shouldice G., Vandezande G. A., Rudin A., *Eur. Polym. J*. **1994**, *30*, 179.

14 *Polymer Colloids: A Comprehensive Introduction* (Fitch R. M.), **1997,** p41.

15 *Colloids and Colloid Assemblies* (Ed. F. Caruso), **2003**, p14

16 Xu F., Zhen G. L., Yu F., Kuennemann E., Textor M., Knoll W., *J. Am. Chem. Soc.,* **2005**, *127*, 3084.

17 Dynamic light scattering (Ed. Berne, Bruce) **2000.**

18 *Polymer Colloids: A Comprehensive Introduction* (Ed. Fitch R. M.), **1997,** p83.

19 Foundations of Colloidal Science (Ed. Robert J. Hunter), **2001**, p204.

Chapter 3 Preparation of Colloidal Crystals and Inverse Opals

In the quest for a method that can be employed for the assembly of monommodal, bimodal and even trimodal colloidal dispersion into crystals in a controllable way, the numerous methods reported for the preparation of monomodal colloidal crystals will be first discussed.

3.1 Background

A rich variety of methods have been reported for the preparation of colloidal crystals.[1-3] These methods can be mainly categorized into six types that are schematically represented in Figure 3.1. Whatever method is applied, the utilization of monodisperse colloid particles, i.e. polydispersity below 5%, is a prerequisite to obtain ordered crystals with a low defect density. Usually, fcc structures with the (111) plane parallel to the surface of the film are obtained. Method a) represents the classical approach of sedimentation of colloid particles under the influence of gravity into highly ordered structures. When the rate of sedimentation is slow the particles at the bottom of the container can undergo the disorder-to-order transition driven by the minimization of thermodynamic energy. But if the particles are sufficiently small or the density of the particles is comparable to that of the dispersion medium, the sedimentation will not occur and the particles exist as stable dispersion. Normally, silica particles with the size larger than 500nm can be crystallized with sedimentation method. The drawbacks of this method are that it provides little control on the quality of the top layer and that it requires much time to obtain sufficiently large samples (several weeks to months). A further problem consists in the difficulty to drive co-crystallization of a bimodal dispersion, because the sedimentation rate under gravity is governed by the Stokes law, which depends directly on the square of the particle diameter and linearly on the density difference between the particles and the surrounding medium as shown in equation (1):

$$v = \frac{2}{9}\frac{ga^2(\rho_P - \rho_L)}{\eta} \tag{1}$$

where v is the sedimentation rate, a is the radius of the particles, g is the

acceleration due to gravity, η is the viscosity of the medium, and ρ_P, ρ_L represent the density of the particle and medium, respectively.

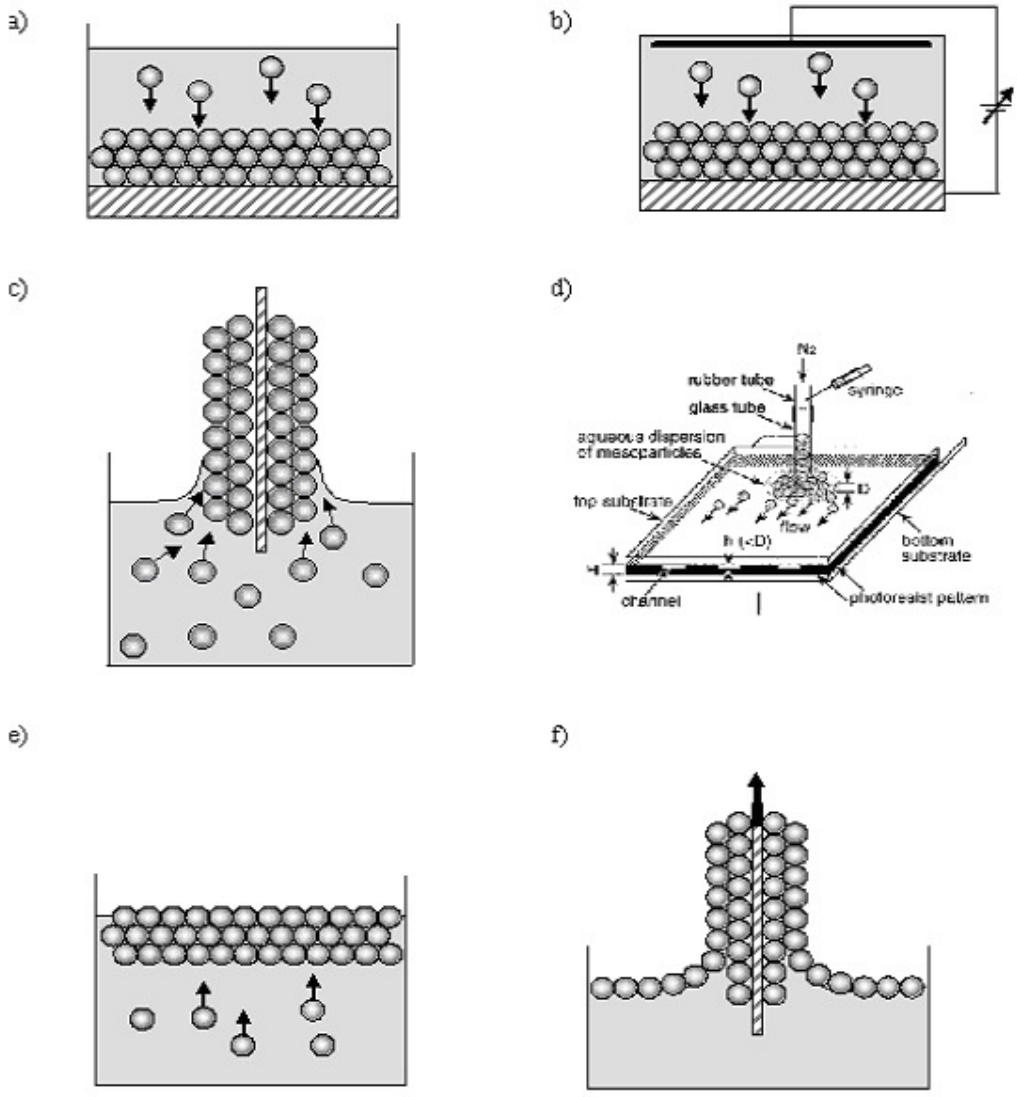

Fig. 3.1: Schematic outlines of the six categories of procedures to assemble colloids into 3D crystalline structures: a) sedimentation in a gravitational field, b) sedimentation under an external electric field, c) vertical deposition by evaporation, d) confined cell technique, e) crystallization at liquid surfaces by flotation, f) vertical deposition by withdrawing.

An artificial force through sedimentation by a centrifuge or applying electrical fields parallel to the sedimentation vector have been used to shorted the time required, as schematically shown in b). Nowadays, sedimentation under electrical fields is widely used for the fabrication of colloidal crystals on patterned substrates with

lattices other than fcc (111).[4,5] Based on the early work and theory developed by Nagayama,[6-8] Colvin and coworkers have used vertical particle deposition procedure shown in c).[9] Here, the crystallization is initially driven by strong attractive capillary forces acting between particles at the drying front when the liquid film reaches a thickness of the particle diameter (see Figure 3.2). This effect drives particles to aggregate in the top layer and creates a porous structure with high specific surface area. The large surface area facilitates solvent evaporation and induces a solvent flux from the suspension bulk through the growing crystal front to the drying particle layer. By this solvent flux particles from the suspension bulk are dragged in a second stage to the growing front and settle epitaxially at this front, allowing the build up of thick particle crystals with over 100 individual layers.[10]

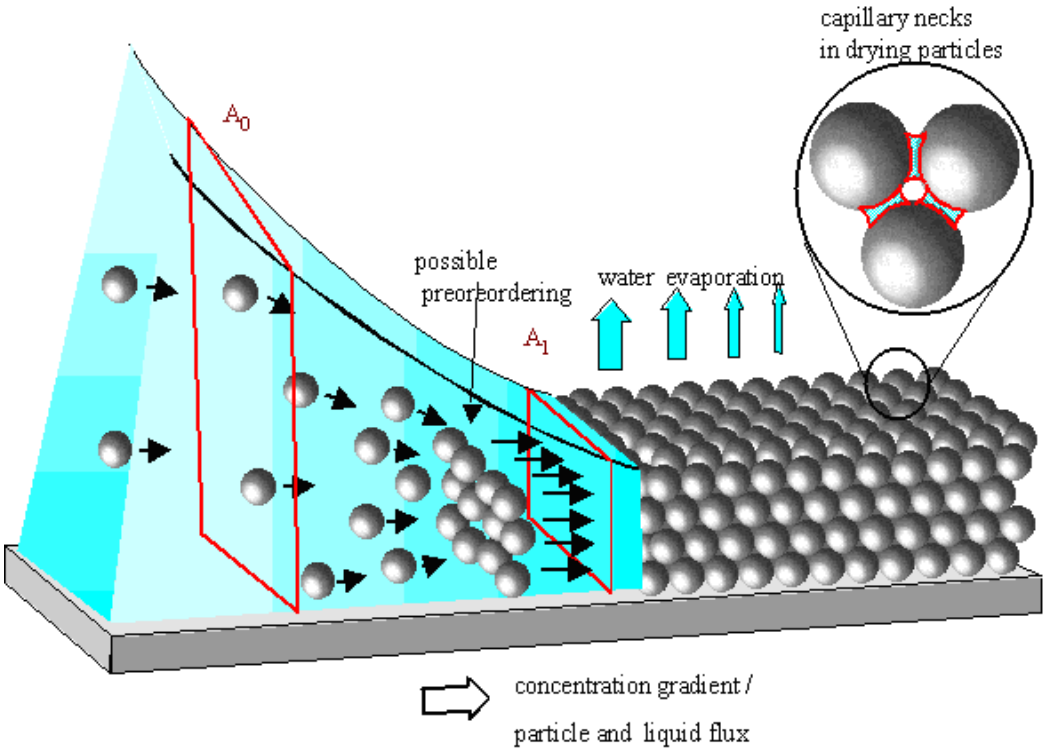

Fig. 3.2: Funnel and Filter' effect of colloid crystallization.

Xia and coworkers invented a method that forms colloidal crystals in a physically confined cell shown in d),[11] in which a colloid suspension is squeezed between two planar substrates spaced by a porous sidewall with channels smaller than the particle diameter. Continuous sonification is used to settle particles in their thermodynamic minimum position. This method reduces the preparation time for colloid crystals substantially, but it requires special equipment (particularly the porous wall) and

might be limited to smaller sample dimensions. Another method is called flocculation shown in e), where the polymer particles (PS or PMMA) assemble at the air-water interface, but again this method (similar to the sedimentation) requires a specific density matching of colloid particles and suspending medium, and the number of layers is not easily controled.[12] A method related to the vertical evaporation is shown in f),[13,14] where a substrate is vertically lifted out of a colloid suspension while the particles crystallize at the drying front into multilayer structures. This method is comparably fast and simple to implement even for large substrate areas. With this method it is further possible to cocrystalize bimodal and even trimodal colloidal structures.

3.2 Experimental

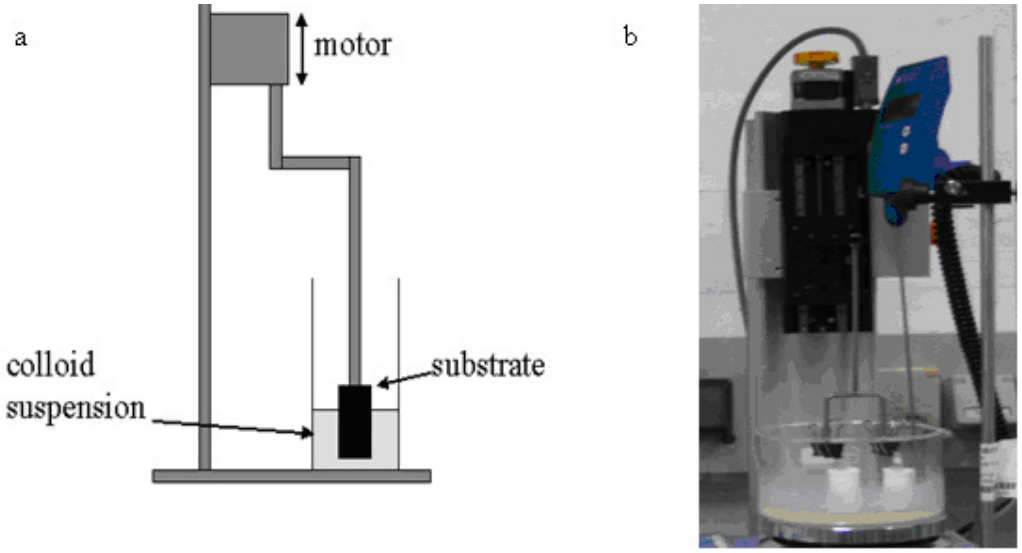

Fig. 3.3: a) Scheme and b) photo graphic image of the dip coating set-up.

Monodisperse polystyrene particles of different size used in the experiments were prepared by emulsion polymerisation and miniemulsion polymerisation described in chapter 2 and were purified by several circles of centrifugation and re-dispersion in ultrapure water (Milli-Q system from Millipore GmbH, Eschborn, Germany). The particle size was measured by dynamic light scattering with Zeta Sizer 3000HS. (Malvern Instrument Ltd.) and confirmed by SEM. Silica nanoparticles used in the experiments were provided by EKA Chemicals. Poly acrylic acids of different

molecular weights were obtained from Aldrich and used as received. UV-Vis-NIR spectra were taken with Lambda UV/VIS/NIR- & UV/VIS Spectrometer (Perkin-Elmer).

Glass substrates, which were cleaned by piranha solution (H_2O_2:H_2SO_4=30:70, v/v. *Caution: piranha solution reacts violently with organic compounds and must be handled with extreme care*) and washed by copious amounts of ultrapure water, were lifted out of the colloidal suspension by a home made dipping devise shown in Figure 3.3. The typical lifting speed was 12μm/min. Low-voltage scanning electron microscope (LV-SEM) images on native samples (non-sputtered) were taken with a LEO Gemini 1530 SEM at acceleration voltages of 0.2-1kV.

3.3 Fabrication of Monomodal Colloidal Crystals (mCC)

3.3.1 Effect of Process Parameters on Formation of mCCs

As stated previously, vertical lifting deposition is adopted to assemble colloidal crystals, not only because this method produces large area of crystals with the uniform thickness, fewer defects, and almost single crystalline orientation within one day, but also for the reason that the vertical lifting deposition can assemble binary and trimodal colloidal crystals. When the substrates are lifted out of a colloidal suspension at controlled speed (normally 12 μm/min with the home made set-up), the hydrophilic substrate entrains some amount of colloidal dispersion due to the surface tension, and the colloidal crystal forms when the meniscus sweeps over the substrate.

The number of the colloidal crystal layers is proportional to the meniscus length, as proposed by Nagayama et al.,[15] who used a similar set-up to deposit colloidal monolayers. From their results they have deduced an equation that includes the parameters which influence the layer number of as-fabricated colloidal crystals:

$$k = \frac{\beta L j_e \phi}{0.605 v d (1-\phi)} \tag{2}$$

k is the number of the particle layers, β is the ratio between the velocity of particle in solution and the fluid velocity (and is taken to be one), L is the meniscus length, j_e is the solvent evaporation rate, ϕ is the particle volume fraction in suspension, v is the

array growth rate determined by the withdrawing speed, and d is the particle diameter. However, equation (1) has to be considered only as a first approximation for the growth of the multilayers by vertical lifting deposition since deviations from the predicted behaviour have been observered.[10,13] In practice, L is related to the surface tension, which can be varied by addition of different kinds of surfactant. j_e can be controlled by the temperature of the suspension. v, the withdraw speed, is set by the motor control shown in Figure 3.3. And d can be easily varied by the different emulsion polymerisation methods mentioned in chapter 2. By changing these parameters monomodal colloidal crystals with a layer number ranging from one to several tens were prepared.

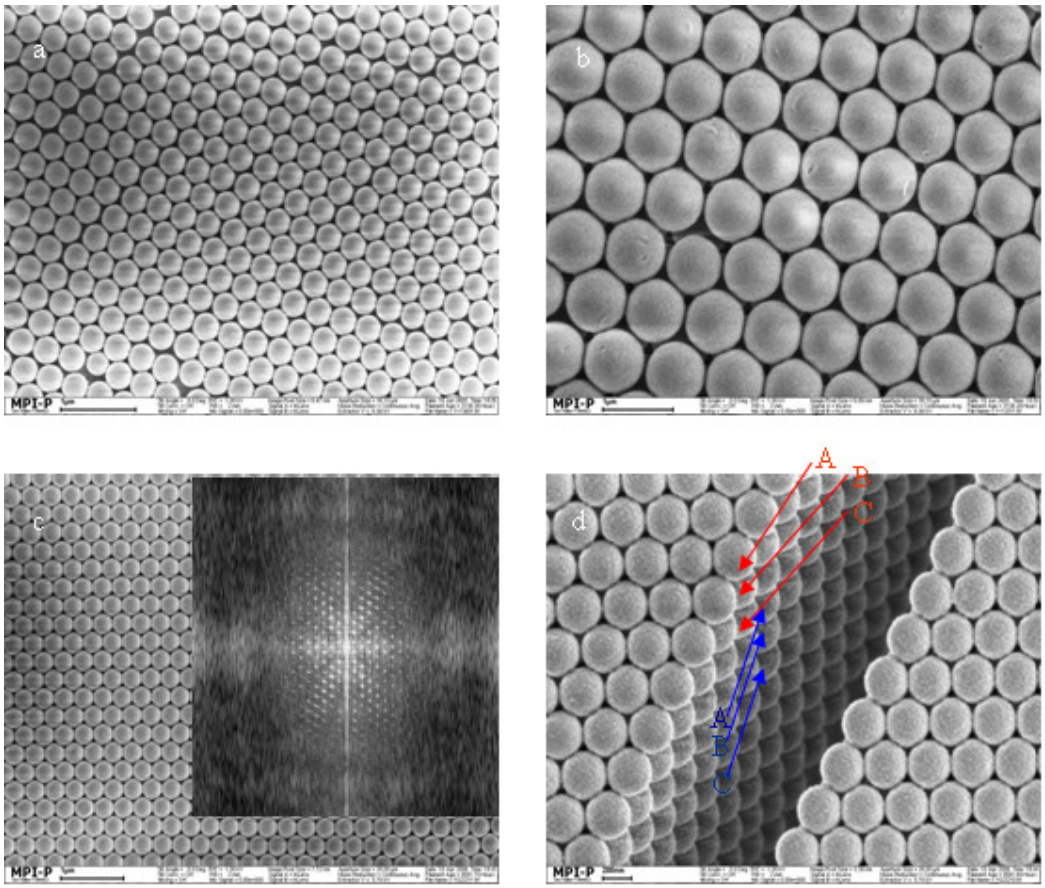

Fig. 3.4: SEM images of monomodal colloidal crystals. a) , b) , c) ,top view, and inset in c) is the FFT image. Image d) is the perspective image from a crystal crack.

Figure 3.4 shows the SEM images of the synthesized monomodal colloidal crystals. Figure 3.1 a) is the monolayer film of polystyrene 839 nm lifted from 0.25 % (v/v) of colloidal suspension with lifting speed of 24µm/min at 30°C. When the lifting speed

was lowered to 12μm/min with the same suspension and the other parameters kept constant, a double layered film was obtained as shown in figure 3.4 b). Figure 3.4 c) is a multilayer film of polystyrene 330 nm with fcc (111) parallel to the substrate. The inset of Figure 3.4 c) is the fast Fourier transformation (FFT) image showing hexagonal patterns reflecting the high quality of the packing of the formed crystal. Figure 3.4 d) is the perspective view from the crack ascribed to the shrinkage of the spheres during the drying process. From this image, we can clearly see the typical ABCABC…stacking of the fcc lattice.

3.3.2 Optical Properties of mCCs

In general, the dielectric constant of colloidal particles is different from that of the surrounding medium, which results in a periodic variation in the refractive index of the material. Similar to the diffraction of X-rays from atomic and molecular crystals, the as-fabricated colloidal crystals diffract UV, visible, or near-IR light, depending on their lattice constant (Figure 3.5). The electromagnetic wave reflected from subsequent layers will interfere constructively if the path difference, $2d\sin\theta$, is an integer multiple of the wavelength λ:

$$n\lambda = 2d\sin\theta \tag{3}$$

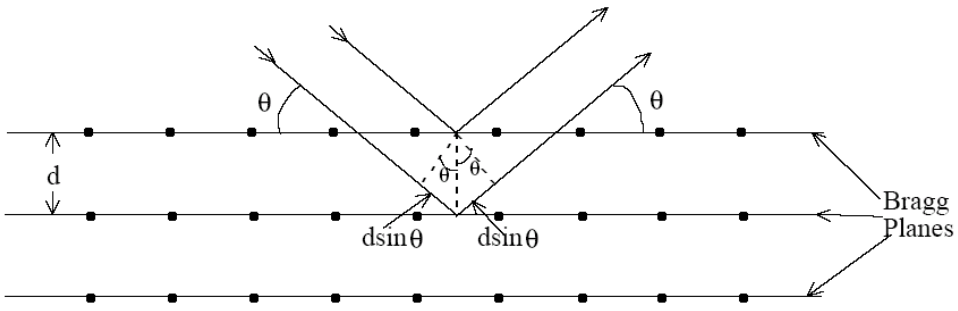

Fig. 3.5: Scheme of Bragg diffraction.

The diffracted wavelength by colloidal crystals can be approximated by equation (4):

$$\lambda_{\max} = (8/3)^2 D(n_{eff}^2 - \sin^2\theta)^{1/2} \tag{4}$$

where $\lambda_{\max}$ is the wavelength of the first order Bragg diffraction, D is the diameter of the sphere, and θ is the angle between the normal vector to the substrate and the

reflected light, and the n_{eff} is the effective refractive index of the colloidal crystal film. For the colloidal crystals in air:

$$n_{eff} = \left[n_{sphere}^2 \phi + n_{air}^2 (1-\phi)\right]^{1/2} \quad (5)$$

here ϕ is the volume fraction of the colloidal particles in the film.

Figure 3.6 displays the absorption spectra of the monomodal colloidal crystals composed of PS 270 nm, PS 330 nm, and PS 489 nm respectively. The light is normal to the fcc (111) plane, thus the θ is 0, ϕ is 0.24, n_{air} =1, and n_{sphere} is 1.59 for polystyrene. The shift of the diffraction peaks is due to the increase of D.

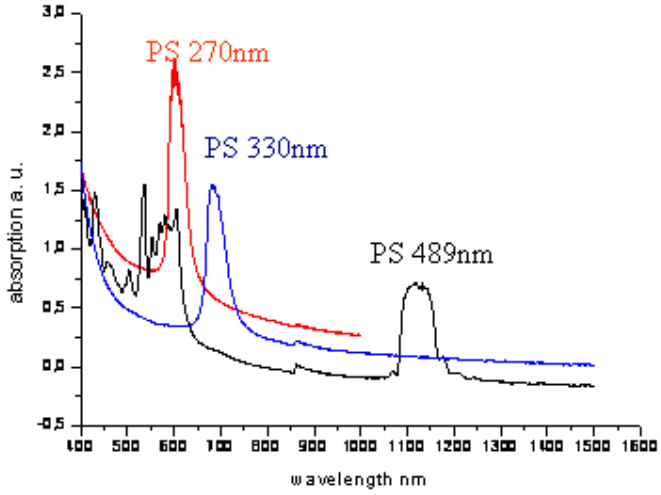

Fig. 3.6: shows the diffracted wavelength with the synthesized colloidal crystal consisting of PS colloidal particles with diameter of 270 nm, 330 nm, and 489 nm.

3.4 Fabrications of Binary Colloidal Crystals

3.4.1 Introduction

Theoretical calculations and computer simulations have predicted that a variety of binary colloidal crystal (bCC) structures can be formed when two species (bidisperse) of colloidal particles are allowed to co-crystallize in suspension, where the type of crystal structures is determined by the size ratio and the relative concentration between small and large particles.[16-18] Such crystal structures have also been observed

experimentally,[19-21] and it was recently found that even oppositely charged particles can form binary colloidal crystals in suspension under appropriate conditions.[22, 23] However, there are limited reports for the efficient fabrication of extended binary colloidal crystals in the dry state due to difficulties in fabrication and characterization, with most of these reported procedures being based on layer-by-layer methods.[24-26] Co-crystallization methods were also employed,[27, 28] but only a monolayer of the as-synthesized bCCs was demonstrated.

In this section, I will discuss the formation of binary colloidal crystal multilayer films under thermodynamic non-equilibrium conditions by vertical lifting deposition from suspensions of mixtures with large and small particles. The influence of the relative concentration and size ratio between the small and large particles of the suspension on the particle stochiometry in the crystal and the crystal quality was systematically studied.

The vertical lifting deposition was further used for the direct replica formation and subsequent preparation of an inverse silica opal by the simultaneous deposition of large, crystal-forming latex particles (the sacrificial template, here polystyrene) and replica-forming nanoparticles (the matrix material filling the interstitial space, here silica nanoparticles), followed by the removal of templating particles and annealing of the replica during pyrolysis at 450°C in air. We found that the variation of the relative particle concentration in the suspension and an optional polyelectrolyte additive (acting as flocculent) determines the filling fraction of small nanoparticles around the large latex particles in the colloid crystal. For the different binary crystals and the silica replicas, optical spectra were measured and compared with the underlying monomodal colloid crystals (mCC).

The particle deposition by evaporation[9] of a colloidal suspension and by vertical lifting[13] of a solid support from the suspension is a convenient method for the preparation of colloidal crystal multilayers with high order and large dimensions (practically over several square centimeters, but potentially much larger in an industrial scale up). These techniques rely largely on the particle transport and deposition at the growing crystal front (Figure 3. 7, right), which is induced by the liquid flow from the suspension bulk to the drying crystal layer (besides capillary forces at the liquid-air interface).[10, 29] The common lattice geometry generally formed by vertical lifting deposition is the close-packed face-centered cubic lattice (fcc) with the (111) plane parallel to the substrate interface. In this lattice two specific types of

interstitial sites exist, the tetrahedral and the octahedral site, as depicted in Figure 3.7, left. The largest sphere that could be theoretically accommodated among the four particles in the tetrahedral site can have a size ratio of $\gamma_{S/L} = d_S/d_L = 0.226$ (relative diameter of the small sphere d_S compared to the large one d_L). For the octahedral site, formed by six particles, this size ratio may not exceed $\gamma_{S/L} = 0.414$.

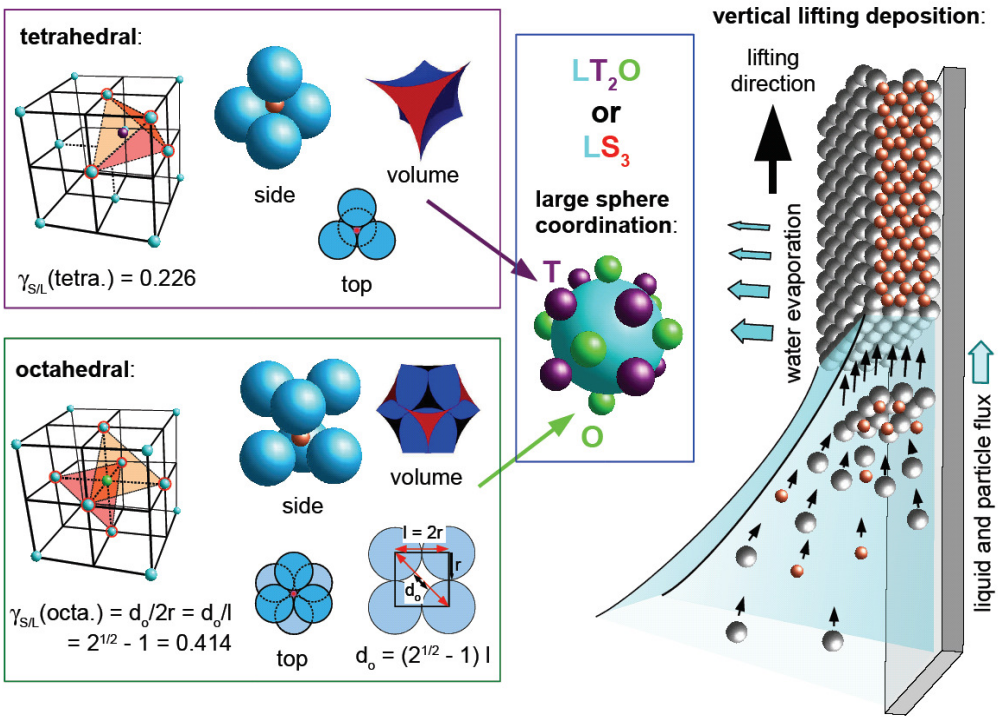

Fig. 3.7: left, Analysis of the fcc lattice geometry with interstitial sites (tetrahedral, left-top and octahedral, left-bottom) for accommodation of small particles. right: Schematic representation of the particle transfer and crystallization mechanism during vertical lifting deposition, which is largely driven by the liquid and particle flux from the suspension bulk to the porous crystal layer, where the liquid is evaporating.

Based on the kinetically controlled process of liquid flux-induced particle packing during vertical lifting deposition, it is possible to simultaneously co-crystallize large and small colloid particles from a mixture in suspension (Figure 3.7, right) into structures, which may not form under thermodynamic equilibrium conditions, e.g. during particle sedimentation. With full occupation of tetrahedral and octahedral sites with one type of small particles, a stoichiometric ratio of three small (S) to one large (L) colloid would be expected in the crystal. If the larger octahedral sites (O) would be discriminated from the smaller tetrahedral voids (T) by differently sized particles, a

theoretical stoichiometry of LT_2O would result. The spatial arrangement of the small particles around a large one is depicted in the center of Figure 3.7. In the experiments previously reported in the literature for single colloidal species, the dependence of the crystal layer thickness on the particle concentration and transfer speed has been studied systematically, with high concentrations and/or low transfer speeds leading to an increased crystal layer thickness on unstructured substrates.[9,13] Besides these parameters, the relative particle concentrations and size ratios in mixtures of large and small colloids are important experimental parameters which have an influence on the lattice geometry and quality in the formation process of binary colloidal crystals. These parameters and the resulting binary colloidal crystals have been investigated in the present study. For this purpose we define the relative concentration as the quotient of the volume fractions $\phi_{S/L}=\phi_S/\phi_L$.

3.4.2 Relative Particle Concentration

The influence of the relative concentration of small polystyrene (PS) particles with respect to large PS colloids on the crystallization and structure formation was investigated for an optimal size ratio around $\gamma_{S/L} = 0.226$ (with the small particles fitting into both, the tetrahedral and octahedral voids). The most appropriate volume fraction for the large particles with a diameter of $d_L = 839$ nm was found to be $\phi_L = 0.01$ to form well-ordered fcc multilayer crystals during vertical lifting deposition at a substrate lifting speed of 0.2 μm s^{-1}. When adding small colloidal particles with a diameter of $d_S = 187$ nm to the suspension, it was found for volume fractions up to about $\phi_S = 4\times10^{-4}$, that the small particles were co-transferred with the large particles to the solid substrate and embedded in the interstitial sites of the highly ordered fcc crystal of the large colloids (see the SEM images in Figure 3.8 a-c). For a specific small-particle volume fraction of around $\phi_S = 2.0\times10^{-4}$, a well-ordered top layer was found in the SEM image (Figure 3. 8 a) with each three-fold hollow site between three large particles being occupied by one small colloid. The surface superlattice of the small particles corresponds to a 1/2cos30° x 1/2cos30° R30° geometry. Besides the usual cracks in the crystal layer, the most common defect structures found in the surface layer are vacancy defects with small particles missing and particle multiplets.

At this concentration (ϕ_S = 2.0×10^{-4}) the surface defect density is the lowest with about 10-20%.

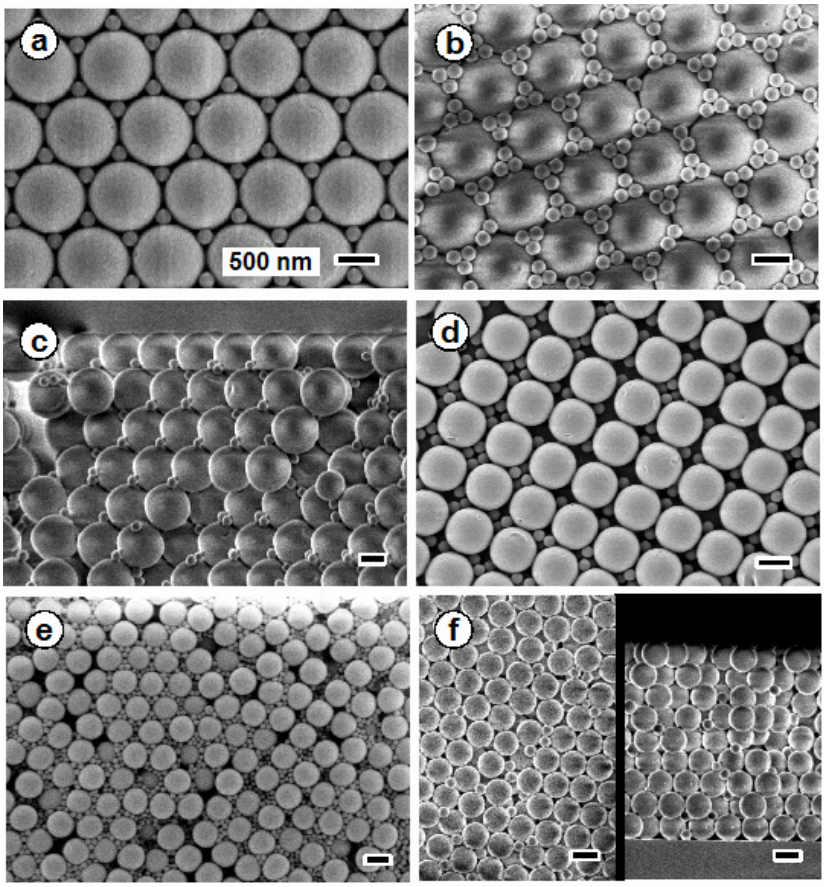

Fig. 3.8: a) Top view onto a binary colloidal crystal prepared from a mixed suspension of large (d_L = 839 nm, ϕ_L = 0.01) and small (d_S = 187 nm, ϕ_S = 2.0×10^{-4}) polystyrene colloids with a size ratio of $\gamma_{S/L}$ = 0.226, showing at the surface a 1/2cos30° x 1/2cos30° R30° superlattice of the small particles. b) At a higher concentration of the small particles (ϕ_S = 3.84×10^{-4}), the voids between the large particles at the surface are filled with colloid triplets. c) Side view of a fracture through the crystal film of a) showing the high fcc order of the large particles and the presence of the small colloids throughout the whole layer. d) Region with a square lattice geometry at higher concentration of the small particles (ϕ_S = 3.07×10^{-4}). e) Disordered mixed film at a very high concentration of small colloids (here 489 nm PS, ϕ_L = 0.005 and 95 nm PMMA, ϕ_S = 6.0×10^{-4}). f) Disordered film for a colloid mixture (489 nm and 209 nm) with low concentration of the small particles (ϕ_L = 0.005, ϕ_S = 1.35×10^{-4}), but a too large size ratio of $\gamma_{S/L}$ = 0.427 to fit into the tetrahedral sites. All scale bars are 500nm.

When the volume fraction of the small particles is increased to about ϕ_S=3.8×10^{-4}, the three-fold hollow sites are filled with a triple cluster of three small particles, as shown in Figure 3.8 b. A fracture through this co-crystal layer (Figure 3.8 c)

demonstrates the high order of the large colloids forming a perfect fcc lattice with the small particles present throughout the entire layer. The small colloids show also some regular arrangement in the fracture plane, but the exact packing structure of the small particles within the crystal bulk cannot be inferred from such fracture images. The partial disorder of the small spheres shown in the SEM image may be an artifact due to particle displacement during the breaking of the sample for SEM measurements, or indeed the spheres are in an irregular arrangement within the crystal. Further experiments such as light scattering and confocal microscopy will be pursued to elucidate the small particle packing in more detail, however this is beyond the scope of this thesis.

Besides the hexagonal superstructures in Figure 3.8 a) and b) also a square geometry is found in some surface areas of the samples with up to four small particles being accommodated in the fourfold hollow site of the large colloids, as shown in Figure 3.8 d). This "defect" structure with square symmetry represents most likely the (100) crystal plane parallel to the surface of the fcc crystal, as it is also observed for monomodal colloidal crystals prepared by the vertical lifting deposition method in our lab. The fourfold hollow site at the surface would thus correspond to the octahedral site of the bulk lattice. Such defect areas can expand over several ten square micrometers and their number increases with higher concentrations of the small colloids.

If the small particle concentration is further increased beyond $\phi_S=4.0\times10^{-4}$ the crystalline packing of the large colloids is hampered and only a disordered particle layer with a mixture of large and small colloids is transferred to the substrate. The typical top and side view of such a disordered layer is shown in Figure 3.8 e) for a mixture of 489 nm PS ($\phi_L = 0.005$) and 95 nm PMMA ($\phi_S = 6.0\times10^{-4}$) particles.

The above-described behavior was generally observed for particle combinations of large to small colloids of 330/52, 362/95, 476/87, 489/95, 520/129, 839/187, and 839/205 (nm/nm) and might apply to an even larger range of particle diameters, as long as the colloid mixture can be co-transferred by the vertical lifting deposition.

3.4.3 Size Ratio Variation

In our experiments, a size ratio of up to about $\gamma_{S/L} = 0.26$ still leads to the ordered crystallization of the large colloids in a fcc lattice with the small particles being embedded throughout the whole crystal layer. This size ratio is slightly larger than the theoretical limit of $\gamma_{S/L} = 0.226$ for the tetrahedral site, and accordingly the defect density of cracks in the crystal film is somewhat higher. For example, in a mixed film of 95 nm and 362 nm particles ($\gamma_{S/L} = 0.262$) the region of undisturbed crystal domains is usually around 2-4 µm in diameter between two microcracks.

If the size ratio substantially exceeds the theoretical limit for the tetrahedral site, the ordered packing of the large colloids is disturbed or even prevented by the presence of the small particles, which get co-transferred during the lifting deposition. This effect is demonstrated in Figure 3.8 f) for a disordered film of a colloid mixture (489 nm and 209 nm) with low concentration of the small particles ($\phi_L = 0.005$, $\phi_S = 1.35\times10^{-4}$), but a too large size ratio of $\gamma_{S/L} = 0.427$ to fit into the tetrahedral sites. The fracture through the film on the right image proves the presence of the small particles throughout the whole layer and its general disorder.

On the other hand, if the size ratio is substantially smaller than the tetrahedral limit, large clusters of small particles can be embedded within the interstitial space of the fcc lattice between the large particles without disrupting the crystal order. This is shown in Figure 3.9 a)-d) for small silica nanoparticles (average size 10 nm, $\gamma_{S/L} = 0.016$) which were co-deposited with 626 nm PS particles.

At a low concentration of the nanoparticles ($\phi_S = 4.31\times10^{-4}$) the large PS spheres ($\phi_L = 0.012$) are only coated with a thin shell of the silica particles during the vertical deposition step, which leads to a rough particle surface structure (see Figure 3.9 a). Under identical conditions, but after addition of polyacrylic acid (Mw 50000 g mol^{-1}, $\phi_{PAA} = 0.013$) to the colloidal suspension much more silica particles are included in the fcc crystal of the large spheres, now completely filling the interstitial volume (Figure 3.9 b). The dramatically increased silica filling fraction is explained by the flocculation effect of the polyacrylic acid, which leads to a stronger attraction between the colloids during the vertical deposition and drying process. A similarly high filling fraction in the cocrystal can be achieved without polyacrylic acid by doubling the concentration of the silica nanoparticles in the suspension to about $\phi_S =$

8.62×10^{-4}. While the free volume between the large colloids is completely occupied by the silica particles (see magnification in Figure 3.9 c), an extremely well ordered fcc lattice is formed, as indicated by the linear cracks in Figure 3.9 c). By carefully optimizing the preparation conditions, very large sample areas over several 100 micrometers with perfect crystalline order and without cracks can be obtained (see "Direct Replica Formation" below and Figure 3.9 f). These experimental findings suggest that the silica nanoparticles may even have a stabilizing and enhancing effect on the crystallization process of the large PS colloids

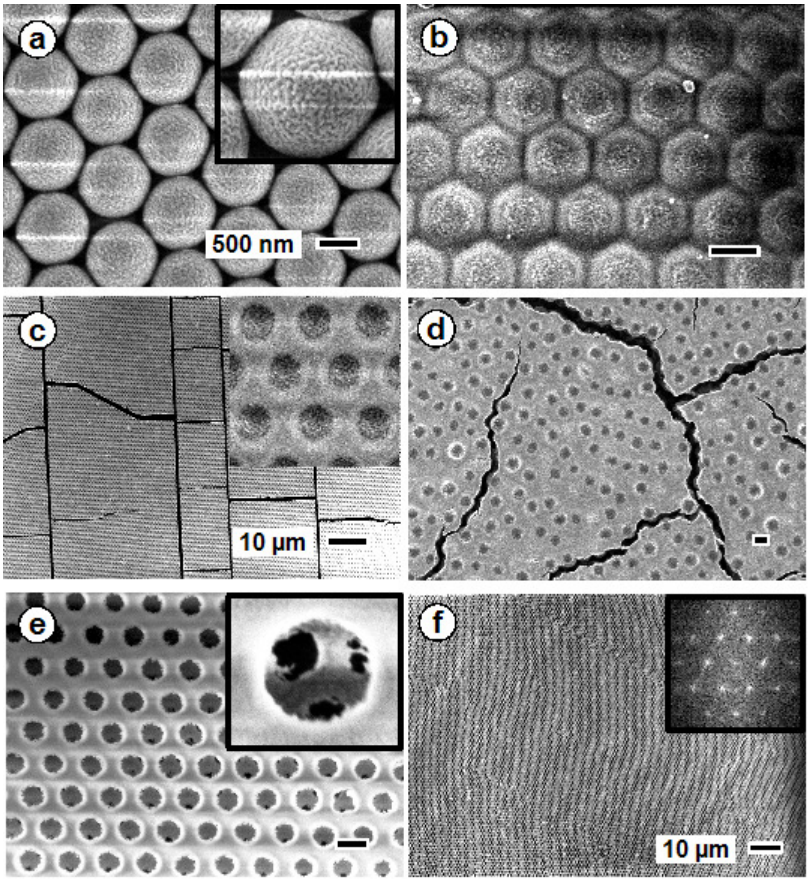

Fig. 3.9: SEM micrographs show the top view of different structures a) Codeposition of silica nanoparticles (average size about 10 nm) at low concentration ($\phi_S = 4.31\times10^{-4}$) with large PS colloids (626 nm, $\phi_L = 0.012$) leading to a thin coating on the large spheres. Magnification shows the rough surface of the coating. b) Complete filling of interstitial volume with the silica nanoparticles due to addition of polyacrylic acid into the suspension (otherwise identical preparation conditions as in a). c) Completely filled colloid crystal without polyacrylic acid, but prepared at higher silica nanoparticle concentration ($\phi_S = 8.62\times10^{-4}$). d) Disordered mixed colloid film obtained at very high silica nanoparticle concentration ($\phi_S = 2.59\times10^{-3}$). e) inverse opals obtained by calcination of the film as shown in c). f) low magnification image of the silica inverse opals with optimal parameters. All scale bars are 500nm except indicated otherwise.

If the relative concentration of the small silica colloids is further increased, the ordered crystallization of the large PS particles is suppressed, as already reported above for the small PMMA spheres with a size ratio of $\gamma_{S/L}$ = 0.194 (Figure 3.8 e). The resulting disordered film prepared from a mixed suspension of the silica (ϕ_S = 2.59×10^{-3}) and the PS (ϕ_L = 0.012) particles is shown in the SEM image of Figure 3.9d). The jagged cracks in this sample additionally confirm the disorder throughout the film, compared to the straight fractures in the highly crystalline layer of Figure 3.9 c).

3.4.4 Direct Replica Formation

The formed composite films consisting of PS microspheres and silica nanopartilces are used to fabricate inverse opals simply by tempering the film at 450°C in air to remove the template PS and sinter the silica nanoparticle matrix**.** Two examples of the obtained silica inverse opals with tuneable periodicity are presented in the SEM images of Figure 3.9 e) and f). The top view of the macroporous film is shown in Figure 3.9 e) with the void diameter of 620 ± 11 nm being comparable to the templating PS microspheres (d_L=626 ± 16 nm), which indicates a negligible shrinkage during the pyrolysis. The inset with higher magnification reveals that each air sphere is connected with its neighbours by round holes resulting from the contact points of the templating PS particles. The image in Figure 3.9 f) at lower magnification as well as the inset with the fast Fourier transformation (FFT) of this image both exhibit the pronounced hexagonal lattice geometry of the replica film without any cracks within several hundred microns. Due to the sintering process at 450°C the as-fabricated film is mechanically robust and thermally stable, which renders it strong enough for further processing such as washing with water, blowing with nitrogen, or further wet-chemical surface modification. Considering the well-defined porosity providing a combination of efficient transport and high specific surface area, the hierarchical structure may be particularly suitable for catalytic and sensor applications.

3.4.5 Spectra

The optical features of the bCC films and inverse opals were characterized by Vis-NIR spectroscopy, and the corresponding stop bands were compared with that of their mCC counterparts. Figure 3 a) shows the absorption spectra of a mCC consisting of PS 476 nm colloids, with the absorption measured perpendicular to the (111) plane, and the absorption spectra of two bCC films comprising PS 476 nm and PMMA 87 nm particles ($\gamma_{S/L}$ = 0.182) with different relative concentrations. When comparing the stop band position of the mCC (1122 nm in the black plot) with that of the bCC films (blue and orange curves), a red shift of the stop band was observed. Moreover, when $\phi_{S/L}$ in the bCC increased from 0.03 to 0.09, the stop band shifted further from 1128 nm (the orange plot) to 1138 nm (the green plot). Such shifts can be explained by the variation of the effective refractive index which depends on the filling fraction of colloidal particles per volume element in the crystal, as discussed further below.

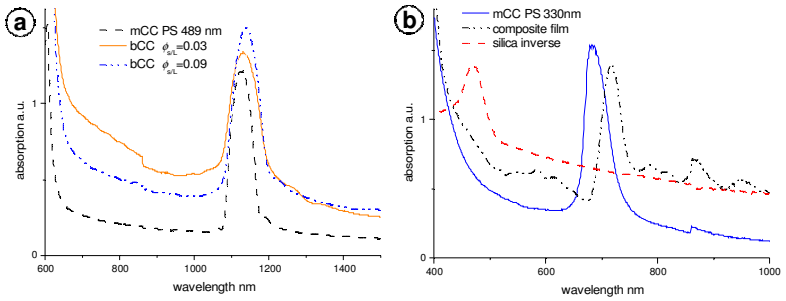

Fig. 3.10: a) Vis/NIR spectra of the mCC formed by 476 nm PS particles (ϕ= 0.005 in suspension), and of bCCs composed of large (PS 476 nm, ϕ_L = 0.005) and small colloids (PMMA 87nm, ϕ_S = 1.5×10^{-4} and 4.5×10^{-4}). b) Vis/NIR spectra of the pure silica inverse opal, the templating mCC (PS 330nm, ϕ= 0.01), and the composite film (PS 330nm, ϕ_L = 0.01 and silica 10 nm, ϕ_S = 6.8×10^{-4}).

In Figure 3.10 b) the absorption spectra of a mCC made of PS 330 nm, a composite film with PS 330 nm and 10 nm silica nanoparticles, and the corresponding silica inverse opal are presented. When comparing the stop band position of the composite film with that of the templating mCC, it is found that the peak is red-shifted from 681 nm to 717 nm. A pronounced blue shift to 480 nm occurs when the PS particles of the composite film were pyrolyzed to form the pure silica inverse opal. These shifts of the

peak positions in these spectra can be explained with Bragg's equation (4), $\lambda_{max} = (8/3)^2 D(n_{eff}^2 - \sin^2\theta)^{1/2}$, for the absorption maxims. Here n_{eff} is the effective refractive index and is determined by equation (5), $n_{eff} = \left[n_{sphere}^2\phi + n_{air}^2(1-\phi)\right]^{1/2}$. In this case ϕ is the volume fraction of the building blocks, n_{block} and n_{matrix} are used instead of n_{sphere} and n_{air} to represent the refractive indices of the building blocks and the matrix, respectively. θ is the angle between the incident light and the normal vector to the fcc (111) plane, in this study it is 0°. For the mCC spectrum (Figure 3.10 a) n_{block} is 1.59 (polystyrene), n_{matrix} is 1.0 (air), and *f* is 0.74 for the fcc lattice. In a bCC, as observed in the SEM images, the large particles can pack in a well ordered fcc lattice while the interstitial space is partially filled by the small colloids. When the interstitial spaces between large PS particles are partially filled with PMMA colloids (n_{PMMA}=1.49), the refractive index of the matrix n_{matrix} increases. Therefore, n_{eff} increases, which results in a red shift of the stop band. As we increase $\phi_{S/L}$ in suspension, interstitial voids between large particles are occupied by more small particles, which leads to a higher n_{matrix}, hence, the stop band further shifts to the right side in the spectra. In the case of the composite colloid crystal with silica nanoparticles, shown in Figure 3.10 b), n_{matrix} increases from 1 (n_{air}) to 1.43 (n_{silica}) in the films, which results in an increase of n_{eff} and causes the red shift. On the other hand, n_{eff} is substantially decreased after removal of the PS particles (n=1.59) from the composite film to form the inverse silica opal. The space originally occupied by the PS particles is replaced by air (n=1), resulting in a pronounced blue shift.

3. 5 Preparation of Multilayered Trimodal Colloidal Structures and Binary Inverse Opals

The quest for photonic materials has reanimated colloidal crystal research with an emergence of innovative preparation methods, new ordered structures and applications. Colloidal crystal self-assembly has attracted particular attention due to its potential as an efficient, inexpensive mass production method.[30, 31, 32] In addition, it provides the possibility to prepare ordered states of matter that are not accessible by other existing nanofabrication methods.[33, 34] The self-assembly process involving multiple colloidal components of different materials and dimensions offers additional

potential. For example, multi-component colloidal crystals can provide intricate structures as basis for photonic and phononic bandgap materials, and multi-scale porous materials with very large surface area for applications in ion exchange, molecular separation, catalysis, chromatography, biomaterials engineering, and membrane reactors.[35, 36, 37, 38]

Recent work has been directed towards the preparation and characterization of binary colloidal crystals.[23-27, 39] This study discribes the first successful co-transfer of a three component mixture with colloidal particles of different materials and diameters in suspension yielding multilayered trimodal colloid crystals by vertical lifting deposition. Pyrolysis of the organic components in these films led to binary inverse opals with a combination of meso- and macroporous cavities. The optical properties of the prepared materials were characterized by Vis-NIR spectroscopy and the measured spectral shifts allowed quantitative calculation of the volume fraction of all components in the film. The crystal structure deduced from these calculations was compared with computer models of the possible particle packing and agreed well with the morphology observed by SEM.

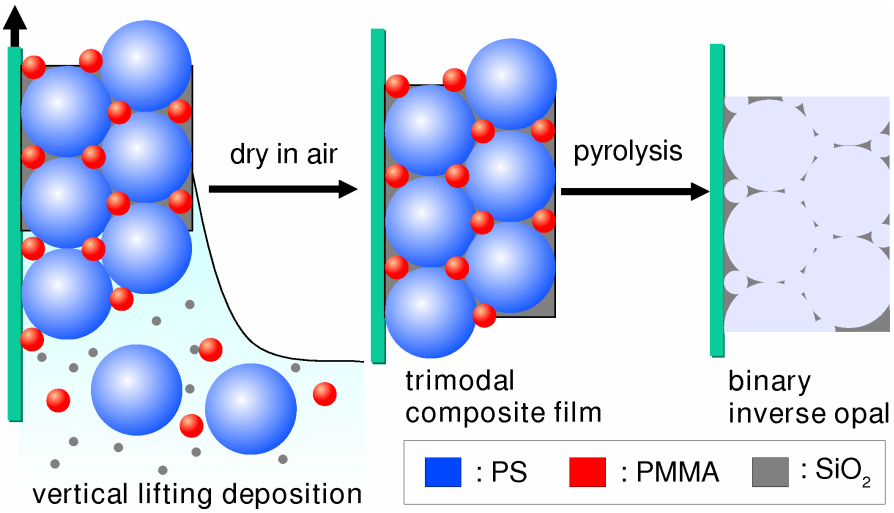

Fig. 3.11: scheme for the preparation of trimodal colloidal structure and binary inverse opal.

Figure 3.11 illustrates the preparation procedure for the trimodal colloid crystals and their corresponding binary inverse opals. We selected polystyrene (PS) microspheres of a diameter D = 465 nm as the large particles, poly(methyl methacrylate) (PMMA) nanospheres D = 84 nm as the intermediate colloids, and silica nanoparticles D = 6 nm as the small component. The relative size ratios were

$\gamma_{I/L} = D_{Intermediate} / D_{Large} = 0.18$, and $\gamma_{S/I} = D_{Small} / D_{Intermediate} = 0.071$, while the relative concentrations were $\phi_{I/L} = C_{Intermediate} / C_{Large} = 0.09$ and $\phi_{S/I} = C_{Small} / C_{Intermediate} = 1.1$. The trimodal films prepared with these parameters maintained the fcc packing of the large PS particles with the intermediate PMMA particles occupying the interstitial voids while the remaining volume was completely filled with the small silica nanoparticles. These silica particles formed the binary inverse opals after pyrolysis.[39] Apparently, the combined effects of the capillary forces and the liquid flux from the suspension to the drying crystal film drive the trimodal crystallization of the particles into an optimal packing, when the meniscus sweeps over the glass substrate while being lifted from the suspension at a controlled speed. By changing the experimental parameters the overall film thickness can be varied between 500 nm up to 6 µm.

Figure 3.12 shows SEM images of the various samples prepared, with the top view of a binary colloidal structure (bCC) consisting of PS (large) and PMMA (intermediate) in Figure 3.12 a). The three-fold hollow sites at the (111) surface of the fcc PS crystal are mainly filled with PMMA particle triplets. Because the PMMA particles start to decompose under the electron beam, these triplets show some deformation compared with a stable PS / PS composite crystal as shown in Figure 3.8.

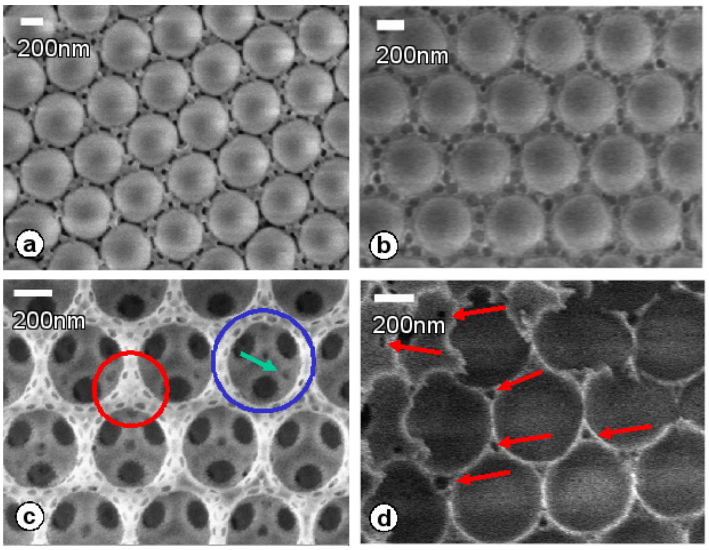

Fig. 3.12: LV-SEM images of the colloid structures. a) Binary colloid crystal (bCC) from large PS and small PMMA particles. b) Trimodal CC from large PS, intermediate PMMA, and small silica particles. c) Top view of binary inverse opal (bIO) after PS and PMMA pyrolysis of the tCC from (b). d) Fracture of the bIO from (c).

The image in Figure 3.12 b) displays the trimodal PS / PMMA / silica composite film (tCC) which was transferred from a mixed particle suspension with the same PS and PMMA concentration as in Figure 3.12 a) and the above specified amount of silica nanoparticles added. In this case, the silica nanoparticles fully occupy the remaining space between the PS and PMMA spheres, with the latter showing beginning decomposition under the electron beam of the microscope. These experiments clearly demonstrate that even in these trimodal particle mixtures the large PS spheres can form a perfect fcc lattice during vertical lifting deposition and accommodate smaller particles in the interstitial space. Figure 3.12 c) exhibits the top view of the binary inverse opal (bIO) formed by pyrolysis of the PS and PMMA particles from the tCC of Figure 3.12 b), leaving a homogeneous silica matrix from the sintered nanoparticles. The sintering process is accompanied with a minor shrinkage of the lattice structure by 2-5 %. Highlighted with the blue circle is the first order macropore with a diameter of 456 nm which originates from the large PS particles and is interconnected with 12 neighboring air spheres by the dark 140 nm windows. The highlighted air sphere triplet in the red circle represents the secondary order pores with a dimension of 80 nm, originating from the intermediate PMMA particles. These pores are also connected with each other by small windows that are formed by the particle-particle contact during drying. Since the size of the connecting windows scales with the particle diameter, we estimate the small window diameters between the secondary pores being about 25 nm in the mesoporous range (80:25=456:140). Thus a regular lattice with a hierarchical film structure of interconnected meso- and macropores is easily created by the presented method. The distribution of PMMA particles within the whole composite film (and not only at the surface) is revealed by the black pores marked with the green arrow in Figure 3.12 c) and corroborated by the pores (highlighted with the red arrows) in the fractured sample of Figure 3.12 d).

The optical properties of all films were characterized by Vis-NIR spectroscopy with the incident light normal to the fcc (111) plane (substrate surface). The spectra are presented in Figure 3.13 a), where the distinct stop band for each structure confirms the high order with a characteristic lattice dimension, in spite of the co-existence of multiple materials with different length scales. The mCC spectrum (iii) with a peak wavelength of 1122 nm represents the reference for the following discussion. Compared to the mCC, the position of the bCC stop band (iv) shifted to a

higher wavelength of 1138 nm, and that of the tCC (v) shifted even higher to 1158 nm. The stop bands of both inverse opals shifted to significantly lower wavelengths, namely 776 nm (ii) for the mono-inverse opal (mIO) and 755 nm (i) for bIO.

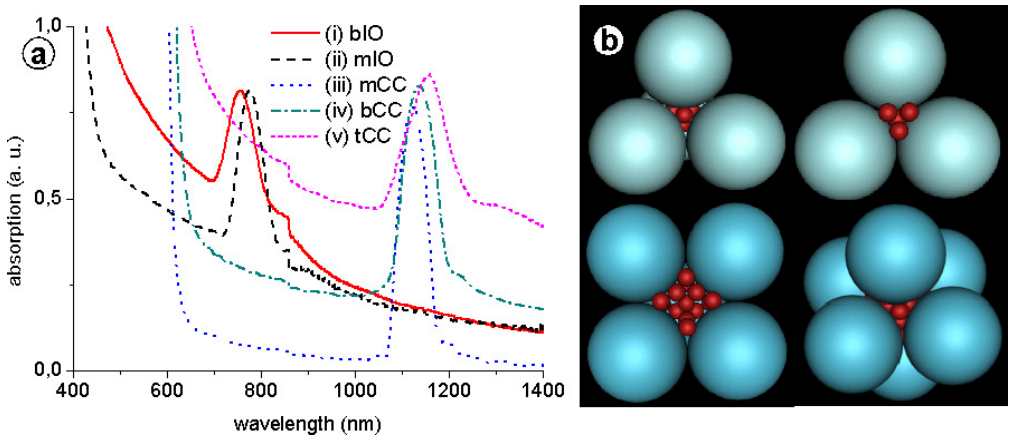

Fig. 3.13: a) Vis-Nir spectra of the formed binary inverse opal (bIO), mono inverse opal (mIO), monomodal colloid crystal (mCC), binary colloidal crystal (bCC), and trimodal colloidal crystal (tCC). b) Computer simulated filling of the tetrahedral (upper row) and octahedral site (lower row) with small particles (γ=0.18).

These stop band shifts can be explained by Bragg's law considering the components refractive indices and their volume filling fractions.[40] In the case of the bCC, which comprises large PS particles (n_{PS} = 1.59) and intermediate PMMA particles (n_{PMMA} = 1.49) with air (n_{air} = 1) filling the voids, the PS particles pack in a regular fcc lattice with a volume fraction of 0.74. Using Bragg's law (Eqs.(4) and (5)) with the measured stop band wavelength of 1138 nm of the bCC, the PMMA volume fraction, ϕ_{PMMA}, was calculated as 9±3%. From the mIO stop band position a refractive index for the nanoporous silica matrix could be determined as $n_{SilicaMatrix}$ = 1.19 ϕ_{PMMA} and ϕ_{PS} in the tCC were regarded as identical to its corresponding bCC, since silica nanoparticles do not appear to obstruct the packing manner of larger spheres as shown by SEM. This assumption was confirmed by back calculation of the theoretical tCC and bIO stop band positions. The derived value for ϕ_{PMMA} was further translated into a crystal structure of the bCC, tCC, and bIO, with each large PS particle (L) correlating to approximately 21-23 intermediate (I) PMMA particles. By computer modeling based on geometrical analyses and optimum position searching, it was found for a size ratio of $\gamma_{PMMA/PS}$ = 0.18 that each tetrahedral site between four

large PS colloids accommodates 4 intermediate PMMA particles, while each octahedral site (between six PS spheres) can accommodate up to 15 PMMA particles. Results are shown in Figure 3.13 b) for PS in blue and PMMA in red: up right, an open tetrahedral site with top large particle removed; up left, tetrahedral site viewed from bottom; lower left, an open octahedral site with one large particle removed, lower right, octahedral site viewed from top. Considering each large sphere is surrounded by eight tetrahedral and six octahedral sights, the stoichiometric composition was derived as LI_{23}. As such, the computer model results correspond well to the ϕ_{PMMA} value deduced from spectral data analysis.

3.6 Fabrication of Colloidal Crystals with Other Methods

3.6.1 Automated Preparation Method for Colloidal Crystal Arrays of Monomodal and Binary Colloid Mixtures by Contact Printing with a Pintool Plotter （This work was performed in cooperation with Dr. Neumann, and Klaus Burkert）

Besides the vertical lifting deposition, a spotting technique was employed to produce colloidal crystal microarrays comprising of up to *9600* single colloidal crystal structures with dimensions down to 100 µm on microfabricated substrates in a parallel fashion.

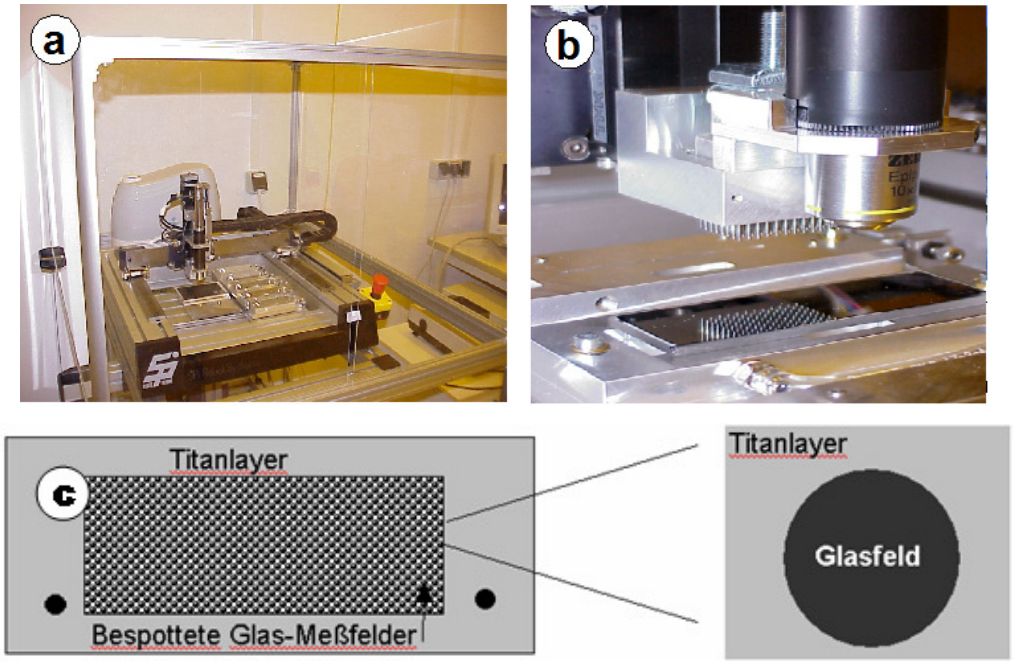

Fig. 3.14: Photographic images of a) high precision portal robot used for spotting colloid suspensions onto pre-structured microarray slides, b) pinhead comprising 96 steel pins with a diameter of d=100 µm, c) scheme of the substrates used for spotting.

Figure 3.14 a) is the high precision portal robot used for spotting colloid suspensions onto pre-structured microarray slides shown in Figure 3.14 c). In order to control the humidity during the spotting and drying process, the system is encapsulated in a housing equipped with an ultrasonic air humidifier. Figure 3.14 b) is a pinhead comprising of 96 steel pins with a diameter of d=100 µm. The pinhead is

automatically adjusted with reference to fiducial fields on the substrate by means of a telecentric microscopy CCD camera imaging system.

Monomodal colloidal crystals and binary colloidal crystals were prepared by contact printing of polystyrene particles in aqueous suspension. The monomodal colloidal crystal arrays were characterized by optical microscopy as shown in Figure 3. 15, the iridescence of all these three samples revealed the regularity of the colloidal structures which is confirmed by SEM images in Figure 3.16.

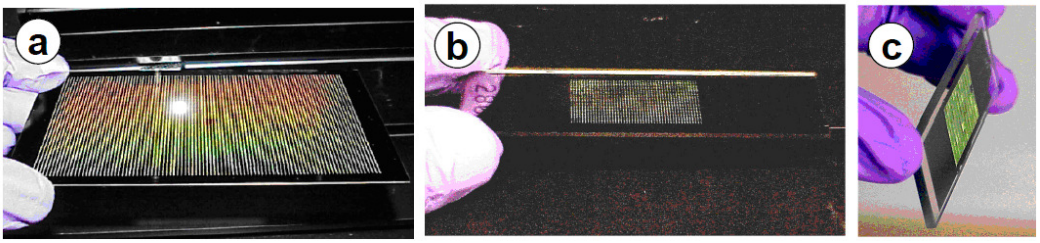

Fig. 3.15: Photographic images of the prepared monomodal colloidal crystal microarrays.

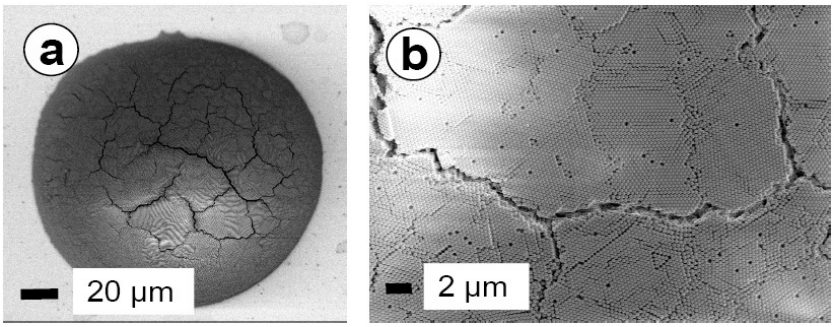

Fig. 3.16: SEM images of a) an individual crystal spot consisting of PS colloids with a diameter of 420nm, b) higher magnification image.

This method was also extended to prepare binary crystals from mixed colloidal suspensions. When the relative concentration and particle size ratio between small and large particles were appropriate, binary colloidal crystal microarrays was fabricated as shown in Figure 3.17.

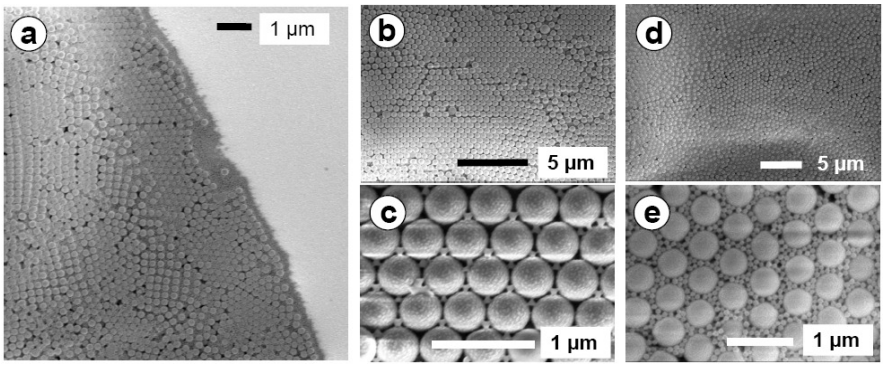

Fig. 3.17: SEM images of binary colloidal crystals. a) The SEM exhibits terrace-shaped form, b) The binary colloidal crystal as in (a) which was obtained by cospotting a mixture of two differently sized particles at a relative weight concentration ratio of $\nu = 0.1$. c) Zoom of image (b) with individual small particles in the three-fold hollow surface sites. d) Binary colloidal crystal spotted at a relative weight concentration ratio of $\nu = 0.41$ with partial disorder. e) Zoom of an ordered domain in d) with many small particles separating the hexagonally packed large spheres.

Optical properties of the colloidal crystal arrays were characterized by reflection spectroscopy. In order to examine the stopbands of the colloidal crystal arrays in a high-throughput fashion, an optical set-up based on a CCD camera was realized. Figure 3.18 a) is the scheme of the set-up, consisting of a white light source, monochromator, polarizer, tilted mirrors, a goniometer, collection lenses and a CCD camera. The crystal array chips are mounted onto the goniometer and reflection spectra are recorded at defined incidence and reflection angles. This set-up allowed simultaneous read-out of all the reflection spectra of several thousand sensor fields per array in parallel.

In agreement with Bragg´s equation, the investigated arrays exhibited strong opalescence, and stopband peaks appeared in the expected wavelength range as shown in Figure 3.18 b), confirming the successful formation of ordered colloidal crystals. Furthermore, a narrow distribution of stopband peaks across the colloidal crystal array

was achieved, as documented by the wavelength distribution histogram in Figure 3.18 c), demonstrating the capability of fabricating highly reproducible crystal spots by the contact printing method with a pintool plotter.

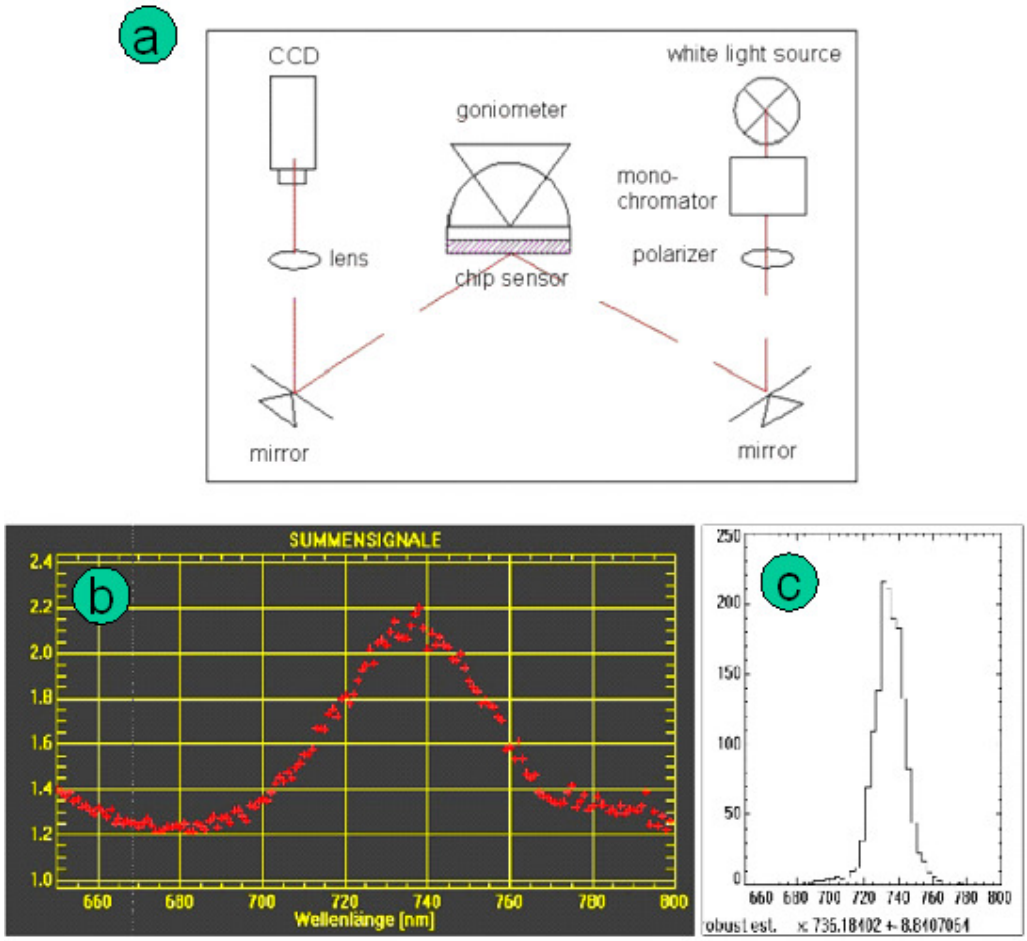

Fig. 3.18: a) Schematic drawing of the reflection readout setup, b) representative reflection spectrum of one colloidal crystal spot (420 nm) with a reflection maximum at 735 nm recorded using the parallel reflection spectroscopy set-up. b) The histogram plot of the wavelength dependent reflectivity (stop-band wavelength) for 1536 colloidal spots demonstrates the narrow distribution of the stop-band position across the entire array.

3.6.2 Vertical Cell Lifting Method for Colloidal Crystal Preparation

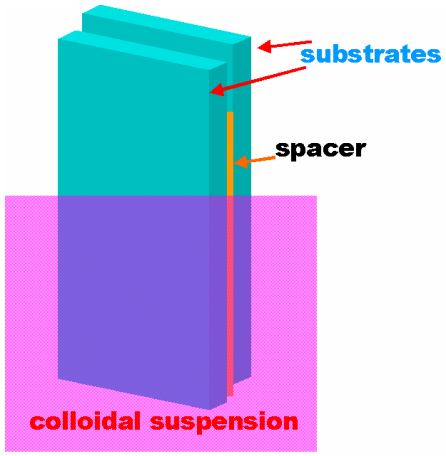

Fig. 3.19: Scheme of a cell method.

Also a so called vertical cell lifting method as a third technique for the preparation of colloidal structures was investigated, Figure 3.19 shows the schematic representation of the procedure, where a cell consisting of two glass substrates separated by two spacers is immersed in a bulk colloidal suspension. The cell is slowly lifted out of the suspension and the colloidal crystal film forms between the two glass substrates by evaporation of the suspending liquid at the top. The film thickness is determined by the spacer between two substrates and the colloidal suspension concentration. Figure 3.20 shows a SEM image of a colloidal crystal film prepared by this method. The film is composed of silica nanoparticles with mean diameter of 6 nm. The film looks quite homogenous, except cracks that are also commonly observed in colloidal crystal films prepared by vapour deposition methods. Confocal microscopy characterization revealed a quite uniform film thickness of about 3µm.

Compared to vertical lifting deposition method, the cell method has potential to produce thicker colloidal crystal films, because the evaporation geometry is different to that of vertical deposition. However, this method takes longer time than conventional vertical lifting deposition in order to obtain crystal films with the area of several square centimetres, because evaporation only occurs at the top of the cell. This method should be useful in the fabrication of nanoparticle crystals (such as nanogold

crystal films, or nanomagnetic crystal films) that could find application in information storage.

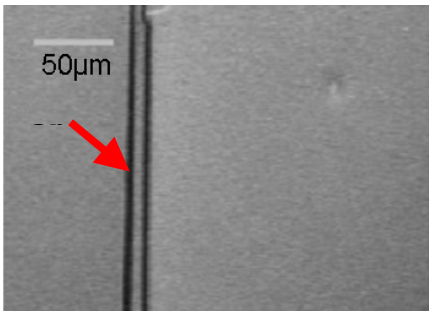

Fig. 3.20: SEM image of colloidal structure film consists of silica nanoparticles with mean diameter of 6nm.

3.7 Conclusions

Monomodal colloidal crystals with the fcc (111) plane parallel to the supporting substrate were prepared by vertical lifting deposition. The thickness ranging from one layer to 80 layers can be easily varied by changing the concentration of the particles in suspension and lifting speed. Typical structural defects, like point defects (e.g. vacancies), line defects (e.g. dislocations), planar defects (e.g. stacking faults), and cracks, usually present in colloidal crystals formed by vertical deposition[9,13] were also found in our materials and well identified in the SEM images. In the present mCCs the approximate diameter of compact domains between cracks were in the order of 10-100 μm (roughly in arrays of several tens to several hundreds particles), an approximate point defect areal density was about 0.005 μm^{-2} at the crystal surface

Binary colloidal crystals with a thickness of several tens layers were directly co-crystallized over a uniform area of several square centimeters within 15 hours by vertical lifting deposition from suspensions with binary colloidal mixtures. The lattice type of the formed crystals could be varied by changing the size ratio and relative concentration between small and large particle in the suspension. The defect density was further increased in the bCCs and additional defect types occurred when compared with those of mCC, which were due to packing faults of the small particles inside the fcc lattice of the large colloids and lattice variations in general.

The developed method was further used for the fast and convenient formation of high quality inverse opals with a low defect density of optical interest by calcination after co-deposition of PS microspheres and silica nanoparticles. It is noteworthy that the defect density in the composite crystals of PS colloids and silica nanoparticles was significantly reduced under appropriate preparation conditions, which might be due to variations of the evaporation kinetics and capillary condensation effects in the mesoporous structure formed by the hydrophilic silica nanoparticles between the PS colloids. This procedure presents a convenient method for the synthesis of metallic inverse opals by lifting a substrate from a colloidal suspension of metal nanoparticle and polymer microsphere. This metallic inverse opal show interesting physical phenomena such as localized surface plasmon resonances (LSPR) and surface enhanced Raman scattering (SERS).[41, 42]

Furthermore, trimodal colloidal structure was fabricated by transferring the large PS particles, intermediate PMMA particles and small silica nanoparticles. And pyrolysis of the trimodal colloidal crystals leads to the corresponding binary inverse opals. Such multi-scaled porous binary inverse opal with ultrahigh available specific surface area which are important in many areas of modern science and technology and could find applications in ion exchange, molecular seperation, catalysis, chromatography, biomaterials engineering, and membrane reactors.

Vis-NIR spectroscopy was used to characterize the stop bands of the corresponding mCCa, bCCs, tCCs, mIO and bIO. The lattice composition in bCC, tCC and bIO was obtained by the spectra shift and the result was confirmed by the computer modeling. As such, the obtained multilayered binary colloidal crystals and trimodal structure with a modified fcc lattice may be more promising candidates for the development of a full photonic bandgap material compared to their monomodal colloidal crystal counterpart.[35, 36]

In addition to the vertical lifting deposition, other methods were also employed to prepare colloidal crystals. Contact printing with a pintool plotter was used to fabricate in parallel monomodal and binary colloidal crystal microarrays comprising of up to *9600* single colloidal crystal structures with dimensions down to 100 μm on microfabricated substrates. Vertical cell lifting method was used to prepare colloidal structures made of silica nanoparticles with 3 μm, which would be almost impossible to the normal vertical lifting deposition, thus provides an avenue for fabrication of thick nanoparticle crystal films.

References:

1 Campo Aránzazu del, Duwez Anne-Sophie, Fustin Charles-André, Jonas Ulrich; review in *Encyclopedia of Nanoscience and Nanotechnology*, Editors: Schwarz James A., Contescu Cristian, Putyera Karol, Dekker Marcel: New York, NY, **2004**, 725-738.

2 Lopez C., *Adv. Mater*. **2003**, *15*, 1679.

3 Xia YN, Gates B., Yin YD, Lu Y., *Adv. Mater*. **2000,** *12***,** 693

4 Dziomkina N. V., Hempenius M. A., Vancso G. J., *Adv. Mater*. **2005,** *17***,** 237

5 Hoogenboom J. P., Rétif C., Bres E. de, Boer M. van de, van Langen-Suurling A. K., Romijn J., van Blaaderen A., *Nano Letters* **2004**, *4*, 205-208.

6 Denkov N. D., Velev O. D., Kralchevsky P. A., Ivanov I. B., Yoshimura H., Nagayama K., *Nature* **1993**, *361*, 455.

7 Dushkin C. D., Nagayama K., Miwa T., Kralchevsky P. A., *Langmuir;* **1993,** *9,* 3695.

8 Velev Orlin D., Denkov Nikolai D., Paunov Vesselin N., Kralchevsky Peter A., Nagayama Kuniaki, *Langmuir*, **1993,** *9*, 3702.

9 Jiang P., Bertone J. F., Hwang K. S., Colvin V. L., *Chem. Mater*. **1999**, *11,* 2132.

10 Fustin C.-A., Glasser G., Spiess H. W., Jonas U., *Langmuir* **2004**, *20*, 9114.

11 Gates B., Qin D., Xia Y., *Adv. Mater*. **1999**, *11*, 466.

12 Im S. H., Lim Y. T., Suh D. J., Park O. O., *Adv. Mater*. **2002**, *14*, 1367.

13 Gu Z. Z., Fujishima A., Sato O., *Chem. Mater.* **2002**, *14*, 760

14 Fustin C. A., Glasser G., Spiess H. W., Jonas U., *Adv. Mater.***2003**, *15* 1025.

15 Dimitrov A., Nagayama K., *Langmuir* **1996**, *12*, 1303

16 Trizac E., Eldridge M. D., Madden P. A., *Mol. Phys*. **1997**, *90*, 675.

17 Dijkstra Marjolein, van Roij Rene, Evans Robert, *Phys. Rev. Lett*. **1998**, *81*, 2268.

18 a) Bartlett P., Ottewill R. H., Pusey P. N., *Phys. Rev. Lett.* **1992**, *68*, 3801. b). Eldridge M. D., Madden P. A., Frenkel D., *Nature* **1993**, *385*, 35.

19 Kaplwn P. D., Rouke J. L., Yodh A. G., Pine D. J., *Phys. Rev. Lett*. **1994**, *72*, 582.

20 Schofield A. B., *Phys. Rev. E* **2001**, *64*, 051403.

21 Wette P., Schoepe H. J., Palberge T., *J. Chem. Phys.* **2005***, 122,* 144901.

22 Bartlett P., Campell A. I., *Phys. Rev. Lett.* **2005***, 95,* 128302

23 Leunissen M. E., Christova C. G., Hynninen Antti-Pekka, Royall C. P., Campell A. I., Imhof A., Dijkstra M., van Roij R., van Blaaderen A., *Nature*, **2005**, *437*, 235.

24 Velikov K. P., Christova C. G., Dullens R. P. A., van Blaaderen A., *Science*, **2002**, *296*, 106.

25 Wang D., Moehwald H., *Adv. Mater.* **2004**, *16*, 244.

26 Ho K. M., Im S. H., Park O. O., *Adv. Mater.* **2005**, *17*, 2501.

27 Kitaev V., Ozin G. A., *Adv. Mater*. **2003**, *15*, 75.

28 Cong H., Cao W., *J. Phys. Chem. B,* **2005**, *109*, 1695

29 a) Fan F., Stebe K. J., *Langmuir* **2004**, *20*, 3062. b) Fan F., Stebe K. J., *Langmuir* **2005**, *21*, 1149.

30 Norris D. J., Arlinghaus E. G., Meng L. L., Heiny R., Scriven L. E., *Adv. Mater.* **2004**, *16*, 1393.

31 Glotzer S. C., Solomon, M. J., Kotov N. A., *AIChEJournal* **2004**, 50, 2978.

32 Dutta J., Hofmann H., *Encyclopedia of Nanoscience and Nanotechnology*, Ed. Nalwa H. S., **2004,** *9,* 617.

33 Gates B. D., Xu Q., Stewart M., Ryan D., Willson C. G., Whiteside G. M., *Chem. Rev* **2005**, *105*, 1171.

34 Geissler M., Xia Y. N., *Adv Mater.* **2004**, *16*, 1249.

35 Joannopoulos J. D., Villeneuve P. R., Fan S., *Nature* **1997**, *386*, 143.

36 Cheng W., Wang J., Jonas U., Fytas G., Stefanou N., *Nature Materials* **2006**, *5*, 830.

37 Yang P., Deng T., Zhao D., Feng P., Pine D., Chmelka B. F., Whitesides G. M., Stucky G. D., *Science* **1998**, *282*, 2244.

38 Yuan Z., Su B., *J. Mater. Chem*. **2006**, *16,* 663.

39 Wang J., Glasser G., Neumann T., Burkert K., Li Q., Knoll W., Jonas U., submitted to *Adv. Mater.*

40 Miguez H., Lopez C., Meseguer F., Blanco A., Vazquez L., Mayoral R., Ocana M., Fornes V., Mifsud A., *Appl. Phys. Lett.* **1997**, *71*, 1148.

41 Coyle S., Netti M. C., Baumberg J. J., Ghanem M. A., Birkin P. R., Bartlett P. N., Whittaker D. M., *Phys. Rev. Lett*. **2001**, *87*, 176801.

42. Tessier P. M., Velev O. D., Kalambur A. T., Robolt J. F., Lenhoff A. M., Kaler E. W., *J. Am. Chem. Soc.* **2000**, *122*, 9554.

Chapter 4 Characterization of colloidal crystals with Brillouin light scattering

(This work was done in cooperation with W. Cheng, Prof. G. Fytas)

4.1 Introduction

Diffraction of photons by periodic structures can display frequency band gaps around Bragg resonance associated with the lattice constant where the propagation of light is forbidden.[1] Such periodic structures were coined photonic crystals. Soon after the emerging exciting developments in this field, theoretical work has focused on the propagation of mechanical (elastic, acoustic) waves in structures with periodic variation of density and /or elastic constants and the search for features with complete phononic band gaps[2-3] in analogy to the optical band gap. The subsequent experimental realization of phononic crystals has been up to now restricted to manually fabricated structures with macroscopic spacing and hence acoustic band gaps in the sub MHz frequency range[4-7]. In contrast to the sonic and ultrasonic crystals, the fabrication of hypersonic phononic crystals at the submicron scale (in the GHz range) requires techniques which are currently being developed[8]. Here, the first observation of a hypersonic band gap is demonstrated in fcc opals of polystyrene colloidal particles infiltrated by different fluids. A self-assembly technique was used to fabricate the opals and high resolution Brillouin spectroscopy was employed to extract the elastic parameters of the constituent particles and measure the dispersion relation between the frequency and the wave vector of the longitudinal wave. Depending on the particle diameter and the speed of sound in the infiltrated fluid, the frequency and the gap width can be tuned. Since hypersonic crystals can simultaneously exhibit phononic and photonic band gaps in the visible spectral region, the technological applications could range from tuneable filters and heat management to acoustic-optical devices[9].

4.2 Brillouin Light Scattering (BLS)

The light scattering event that leads to no change in the incident wavelength is known as Rayleigh elastic scattering. The scattered intensity is inversely proportional to the fourth power of the wavelength of the incident light, and hence the blue light exhibits much stronger scattering than the red light assuming higher transmission. This rationalizes the colours of the sky and the sun in the sky and at the horizon. In addition to the strong elastic scattering due to (static) frozen spatial fluctuations, there is also a weaker inelastic (Brillouin) scattering with small frequency shifts of the incident light. Brillouin scattering is caused by propagating density fluctuations (phonons) in the material. An incident plane wave with an electric field,

$$\vec{E}(\vec{r},t) = \vec{E}_0 e^{i(\vec{k}_0 \bullet \vec{r} - \omega_0 t)} \tag{1}$$

induces a dipole, $\vec{P}$, in a molecule, given by:

$$\vec{P} = \varepsilon_0 \chi \vec{E}(\vec{r},t) \tag{2}$$

where χ is the susceptibility. A result of EM theory is that a dipole oscillating at a frequency ω_0 radiates with a frequency ω in a direction $\vec{k}_s$, where the subscript s stands for the scattered light. The susceptibility χ depends on the density and thus fluctuates with time. The scattered photons have therefore frequencies different from ω_0. There are two components of the fluctuations in density when the material is treated as a continuum (hydrodynamic limit): The Rayleigh central peak damped by the thermal conduction and the Brillouin doublet symmetrically shifted around the Rayleigh line due to the sound waves damped by the viscosity.

The analogy to the Bragg diffraction may be the most direct way to visualize the Brillouin scattering. In Figure 4.1, light of wavelength λ_i impinges onto the sound waves with wavelength of Λ_s. Due to the density variation as the result of the periodic pressure modulation, some of the light is diffracted with the reflection angle being equal to the incident angle. It is exactly what happens when light encounters an interface where the dielectric constant changes.

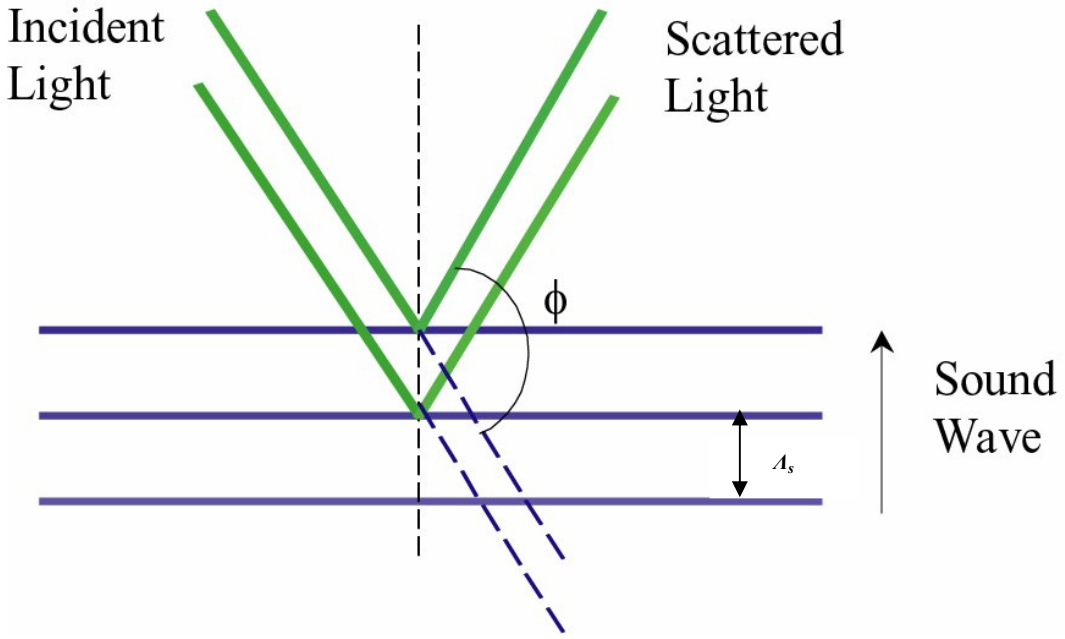

Fig. 4.1: Diffraction of photons by phonons.

In order to observe light at a specific angle, the diffracted beams from different maxima of a sound wave must interfere constructively i.e. the Bragg condition should be satisfied (Equation 3 in Section 3.3.2). Hence, according to Figures 3.5 and 4.1, $d=\Lambda_s$ and $\theta = \phi/2$. Then the condition for Bragg reflection from sound waves reads:

$$\lambda_i = 2\Lambda_s \sin(\phi/2) \tag{3}$$

The frequency $\Delta f=c/\Lambda_s$ of the sound waves with a phase velocity c can be then written as

$$\Delta f = (2c/\lambda_i)\sin(\phi/2) = cq/2\pi \tag{4}$$

where $q=(4\pi/\lambda_i)\sin(\phi/2)$ is the scattering wave vector . The sound waves, however, propagate through vibrating matter (up and down in Figure 4.1) which leads to a Doppler frequency shift $\pm\Delta f$ for the scattered light. Thus the sound wave contribution to the Brillouin scattering spectrum consists of two peaks symmetrically shifted around the frequency f_i of the incident laser beam. Figure 4.2 shows schematically the simplest Brillouin spectrum of a homogenous medium consisting of a triplet structure.

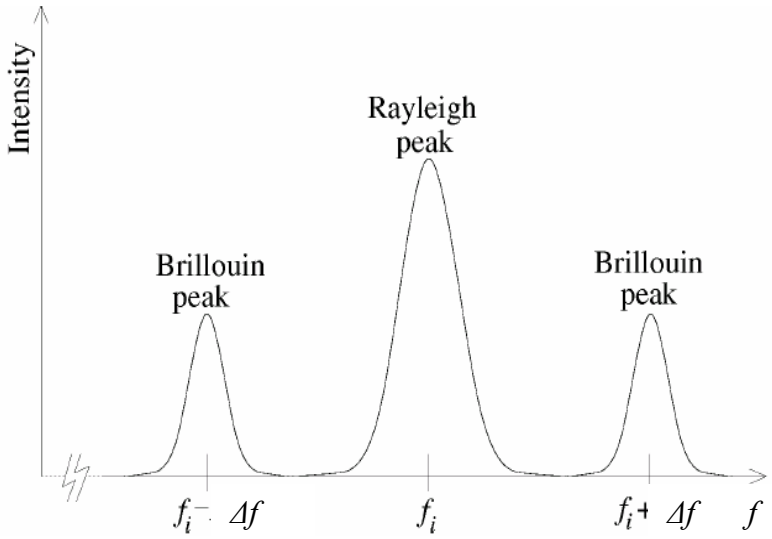

Fig. 4.2: The Brillouin spectrum**.**

For systems inhomogeneous over distances comparable with the phonon wavelength Λ_s, the Brillouin spectrum deviates from the simple structure of Figure 4.2 and can yield rich information on the elastic properties of the microphases. The present colloidal crystals show such inhomogeneous systems which further permits the utilization of the directionality of the scattering wave vector **q**. As sketched in Figure 4.3, $\mathbf{q}=\boldsymbol{k}_s - \boldsymbol{k}_i$, denoting also the sound propagation direction, is defined by the wave vectors of the scattered ($\boldsymbol{k}_s$) and incident ($\boldsymbol{k}_i$) photons. For the special scattering geometry adopted in our experiment with $\theta=2\alpha$ (α being the incidence angle normal to the film surface), $\boldsymbol{q}$ lies in the (111) plane (parallel to the film surface) of the fcc lattice, its amplitude $q=(4\pi/\lambda)\sin(\theta/2)$ is free from the influence of the refractive index of the medium, and it depends only on the scattering angle θ and the wavelength of the incident laser beam λ. In hypersonic crystals, as requested by the translational symmetry of the lattice, the momentum conservation has to be modified by introducing a reciprocal lattice vector $\boldsymbol{G}$ so that $\boldsymbol{q}=\boldsymbol{k} \pm \boldsymbol{G}$**.** Since phonons with wave vectors $\boldsymbol{k}$ and $\boldsymbol{k} \pm \boldsymbol{G}$ represent the same wave according to Bloch's theorem, the phononic properties of a hypersonic crystal can be revealed by recording the dispersion relation $\omega(q)$. In combination with its high resolution compared with inelastic X-ray scattering,[10] Brillouin light scattering (BLS) has been used as a unique nondestructive and noncontact technique to probe phonon propagation in microstructures at hypersonic frequencies.

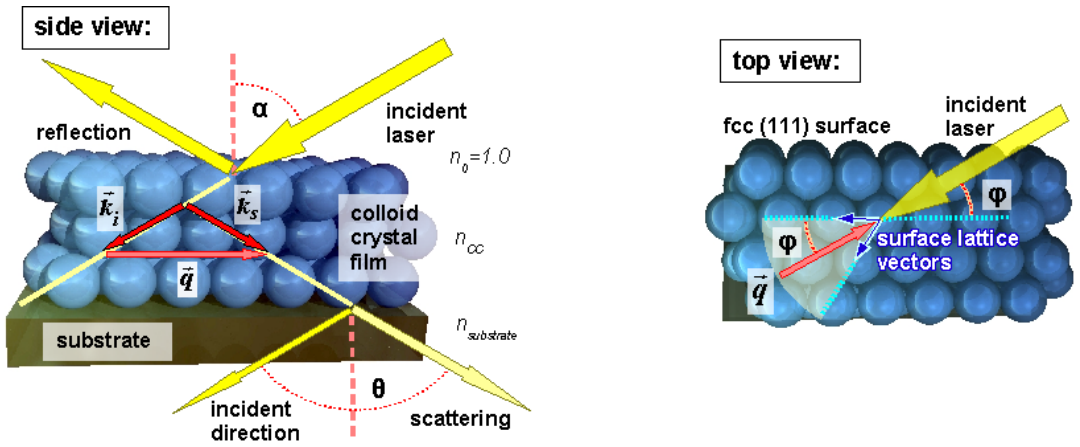

Fig. 4.3: Scheme of the supported film structure and the scattering geometry**.** The side view shows the different light beams (incident, reflected, transmitted and scattered) and the wave vectors for the incident laser and the scattered light defining the scattering wave vector q in the (111) plane of the fcc crystalline film. The refractive indices of the different layers do not affect q when the scattering angle θ is twice the angle of incidence α.The top view illustrates the possibility to probe wit q different directions (φ) in the (111) plane of the fcc lattice.

4.3 Experimental

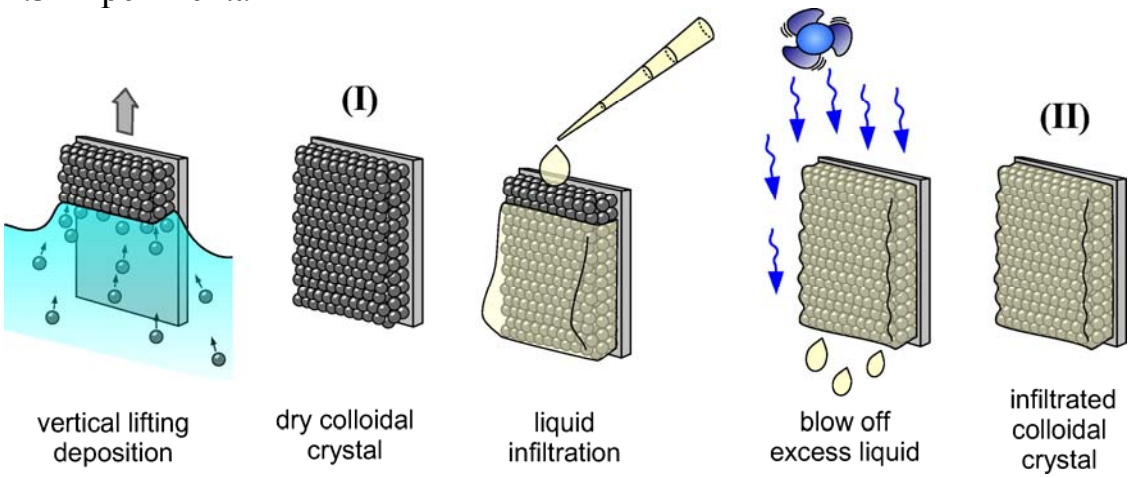

Fig. 4.4: Steps in the fabrication of soft opals films**.** Self assembly and infiltration procedures.

Crystalline films of monodisperse polystyrene (PS) spheres in air have been fabricated with the vertical lifting deposition (for details readers are recommended to read chapter 3), where the monodisperse PS particles were synthesized with the emulsifier free emulsion polymerization and purified by several cycles of centrifugation and redispersion (details about emulsion polymerization can be found in chapter 2). To obtain liquid infiltrated colloidal crystals, these dry PS opals were subsequently infiltrated by fluids with different longitudinal sound velocities (here we

used glycerol, silicon oil poly(methylphenylsiloxane), PMPS, poly(dimethylsiloxane) PDMS 1000 g/mol) by pipetting an appropriate volume onto the crystal and removing excess liquid in a constant stream of nitrogen for 4 hours. The entire procedure is outlined in Figure 4.4.

4.4 Characterization of Dry Colloidal Crystals

For colloidal crystals in aqueous solution, BLS has revealed the presence of various excitations related to particle eigenmodes (collective polymer vibration within a sphere)[11, 12], ″Bragg″ modes (phononic bandgap due to constructive and destructive interference) and mixed modes (due to acoustic phonons/particle eigenmodes hybridization)[12]. The former are rather weak due to the immediate contact with the fluid medium[13] and hence leakage of the elastic energy. Very recently[14], the application of BLS to a synthetic opal consisting of closed packed SiO_2 (in air) has resolved up to six particle eigenfrequencies describing its spheroidal (*i, l*) modes where *i* designates the *i*-th mode of the *l*-th harmonic. The amplitude of the modes decreases monotonically with *l* for the highly incompressible SiO_2 and hence still many modes are probably missing. Colloidal crystals prepared in our lab for a range of particle diameters offer the possibility to enhance the amplitude of the elastic excitations and hence resolve a large number of eigenfrequencies allowing for a rigorous comparison with theoretical calculations.

With the vertical lifting deposition method, we fabricated crystalline films of monodisperse polystyrene (PS) spheres in air and measured up to twenty-one vibrational modes by high resolution inelastic light (Brillouin) scattering. For five different particle diameters (d) between 170-860 nm, this rich experimental spectrum is well captured theoretically proving the scaling relation $\omega(i, l) \sim d$ for all localized PS modes with two material elastic constants (e.g. Young's modulus, shear modulus) and the particle size polydispersity. The experiments have revealed an additional unexpected low frequency continuum mode which probably relates to overdamped shear waves.

The PS opals exhibit strong multiple light scattering due to the strong elastic form factor of the individual nanospheres and their large optical contrast with the surrounding air. The scattering wave vector $\boldsymbol{q}$ is therefore ill-defined and at any scattering angle the spectrum corresponds to a backscattering geometry with $q=4\pi n/\lambda_0$

where the refractive index n=1.59 and λ_0 (=532nm) is the laser wavelength. In this case, the dispersion relations for acoustic-like phonons[8,11, 12, 15,] cannot be measured. However, photon multiple scattering was found to enhance the inelastic scattering from localized (***q***-independent) modes. Figure 4.5 a) displays the ***q***-independent Brillouin spectra of the five PS opals recorded at low scattering (20°) angle by a six pass tandem-Fabry-Perot interferometer[16]. The incident laser beam and the scattered light were both linearly polarized perpendicular to the scattering plane but due to the mixture of the polarization the spectra include contributions from longitudinal and transverse modes. For the two largest diameters, the multiple scattering cut-off at about 14 GHz corresponds to the acoustic phonon in bulk PS with $\lambda \approx 5.8$GPa.

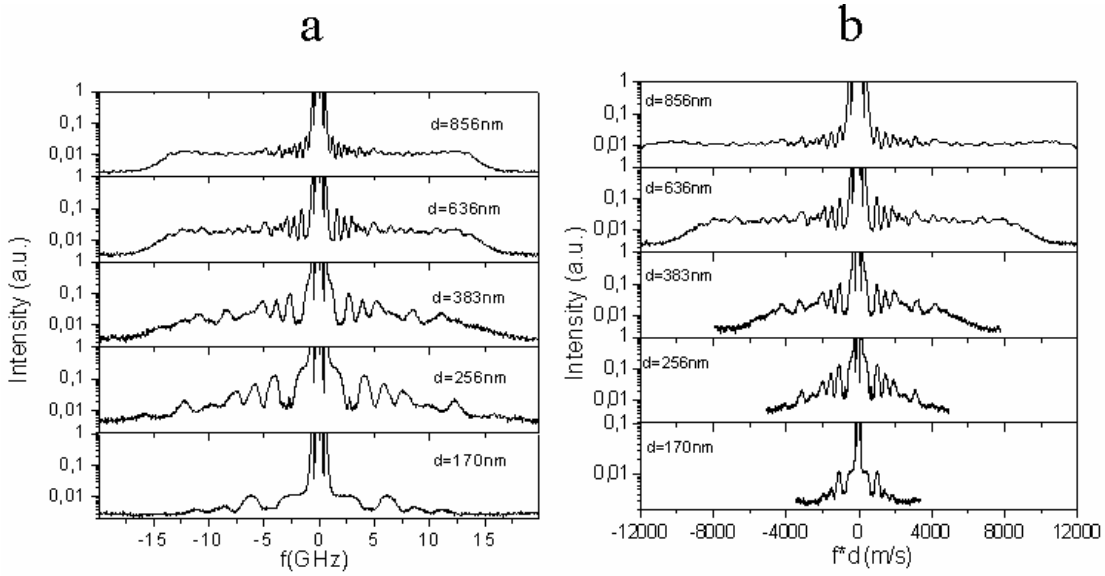

Fig. 4.5: a) Brillouin light scattering spectra of polystyrene opals with five different particle diameters, d, as indicated in the plot. More than twenty modes can be resolved in the opal with the highest d=856 nm, b) the scaling of certain spectral features with d is depicted by the reduced plot in b.

The spectra showed several Brillouin doublets with their number and proximity increasing with particle diameter; up to 21 modes are resolved for the highest d in comparison with the six modes observed in silica opals.[17, 18] The ***q***-independence of the spectra was verified for the PS opal with the lowest d that exhibited the weakest multiple scattering among all samples and confirmed to the localized nature of these modes. The latter was demonstrated in the reduced plot in Figure 4.5 b. The pertinent features observed, for the first time, in this plot, are : (i) the successful scaling of the

rich spectrum of the vibration modes, (ii) the line shape and the amplitude of the observed modes and (iii) the featureless low frequency spectral component .

My co-operators, Economou et al. compared the experimental data with the theoretical results obtained by considering a plane sound wave propagating in the air and impinging upon a single PS sphere in air. The sphere eigenmodes appear as resonance peaks in the acoustic wave scattering cross section plot versus frequency. They depend on the mass density and the speed of sound in the air and in the PS particle, as well as on the size of the particle. To reveal more clearly the resonances, we have subtracted from the calculated scattering amplitude the scattering amplitude for a rigid sphere of equal size. The peaks in the scattering cross section are very narrow, since the elastic constant and mass density contrast between the PS sphere and the surrounding air is very large and the coupling of the sphere eigenmodes to the surrounding air is small. To avoid the possibility of losing a peak in the calculations (due to its almost δ-function shape) we use instead of the air mass density an artificially larger mass density of 50kg/m^3, for the matrix material surrounding the particles. This results in a broader width for the calculated peaks without altering their position.

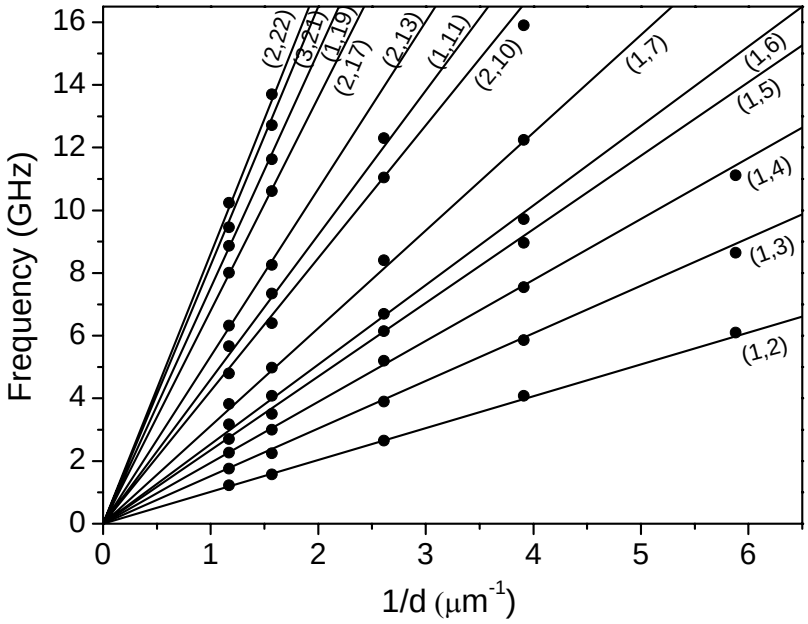

Fig. 4.6: Peak frequencies of the Brillouin spectra as a function of the inverse diameter. Up to thirteen frequencies are shown to obey the f~d-1 scaling (solid lines).

The resonances at frequencies f (*i,l*) are labeled by (*i*, *l*) where *l* denoted the angular momentum quantum number, and *i* is the order of the mode for a given *l*. The identification of the quantum numbers in theory is done by taking the incident sound wave of only one *l* each time. In the calculations, they used the experimentally provided values for the longitudinal sound velocity c_L=2350m/s and mass density ρ=1050kg/m^3 of PS, while the value of the transverse sound velocity, c_T=1210m/s, in PS was obtained by fitting the calculated frequencies to the experimental ones. These theoretical calculations with a single adjustable parameter describe the experimental vibration eigenfrequencies very well, as demonstrated by the solid lines in Figure 4.6, and the comparison between the theoretical and experimental reduced frequencies f(*i*,*l*)d in the first and second column of Table 4.1. The observed agreement allowed for the assignment of the observed modes, identified by the integers (*i*, *l*), which are compiled in Table 4.1. We noted here that the sound scattering cross section calculations can be used as a method for the determination of unknown material parameters.

Table 4.1: Vibration modes of polystyrene spheres in air.

	f(*i*,*l*)d(nmGHz)[a]	f(*i*,*l*)d(nmGHz)[b]	(*i*,*l*)
1	1040	1017	1,2
2	1480	1518	1,3
3	1900	1945	1,4
4	2310	2348	1,5
5	2480	2538	1,6
6	3140	3119	1,7
7	4100	4237	2,10
8	4700	4607	1,11
9	5290	5340	2,13
10	6780	6797	2,17
11	7450	7523	1,19
12	8100	8247	3,21
13	8730	8609	2,22

a) experimental b)computed

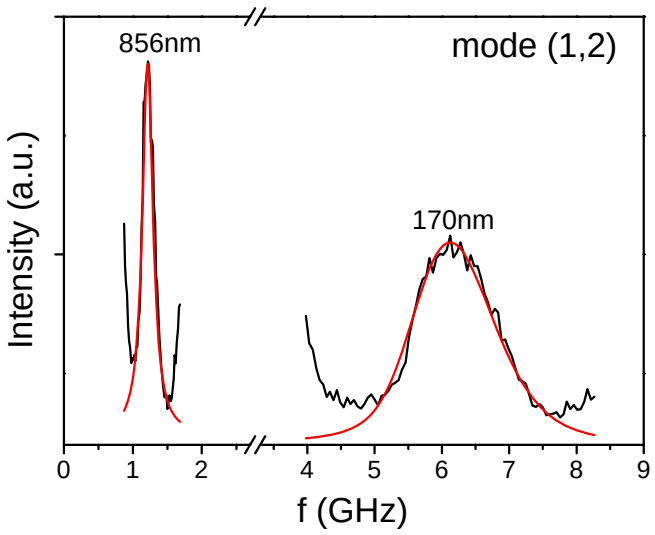

Fig. 4.7: The lowest frequency (1, 2) modes for the smallest and largest PS sphere, black line represents the experimental data, while red curve is the theoretical fitting.

For an isolated particle without internal losses, there is no dissipation of the elastic energy which should lead to very narrow spectra indistinguishable from the instrumental function. The observed broad and asymmetric line shape of the experimental peaks, in particular for the low *l*-modes (Figure 4. 7), was attributed to the finite particle size polydispersity. My coworkers theoretically represented this frequency dependence by a convolution of a Gaussian distribution function of the particle size and a Lorentzian line:

$$I(\omega) \approx \int dx A(x) \frac{\Gamma(x)}{(\omega - \omega(x))^2 + \Gamma(x)^2} \frac{\exp\left[-(x-D)^2 / 2\sigma^2\right]}{\sqrt{2\pi}\sigma} \tag{8}$$

where $A(x) \approx A_0$, $\omega(x) = \frac{c_1}{x}$. The peak frequency ω(x) and the natural half width at half maximum, Γ(x), was close to the instrumental width for monodisperse particles without internal losses. The experimental spectrum for the lowest frequency mode (1,2) of the smallest (170nm) and largest (856nm) PS spheres (black line in Figure 4.7) can be reproduced well (red line in Figure 4.7) by Equation (8) by using fixed c_1=1020nmGHz (the slope of the solid line in Figure 4.6) and the variance σ as the only adjustable parameter besides the amplitude A_0. The different shape of the experimental spectrum of the (1, 2) mode for these two diameters is partly due to the ω~1/d dependence and the different size polydispersity (σ=14 for 170nm PS particles

and 10 for 856nm PS particles) with the large particle possessing lower σ. The obtained values of the variance confirmed the size distribution extracted from the SEM images. For particles in the nanometer and micrometer range, the eigenfrequencies fall in the teraherz[19,20] and megahertz[16] range, respectively.

4.5 Characterization of Wet Opals

The existence of band gaps in various phononic crystals has been experimentally observed[4-7], yet all realized systems so far are restricted to sonic and ultrasonic crystals with macroscopic periodicity, e.g. in the millimeter range assembled manually with great patience[5-7]. The desire for further extending the investigation of this phononic band gap formation phenomenon to even higher frequencies, entering the hypersonic (GHz) range, largely comes from the distinct nature inherent to hypersonic waves and the consequent emergence of possible novel applications.[8, 9, 21, 22] Unlike sonic and ultrasonic waves, whose generation usually relies on an external stimulus, acoustic waves at hypersonic frequencies can be formed merely by random thermal motion of the atoms of a material, and these high-frequency thermally excited acoustic waves are often referred to as phonons. In dielectric materials, thermal energy is mainly transported by phonons, therefore hypersonic phononic crystals capable of manipulating the flow of phonons could have an impact on controlling the thermal conductivity. Furthermore, due to the fact that its lattice constant lies in the range of visible light wavelength, a hypersonic crystal may permit concurrence of phononic and photonic band gaps,[8, 9, 22] making the integrated management of electromagnetic and elastic waves possible. This feature, unique to hypersonic crystals, allows the design of a number of novel acousto-optical devices[8,9,22] including optical modulators and optically pumped acoustic oscillators.

To shift the band gap to higher frequencies, the creation of periodic patterns necessarily at the submicron scale can benefit from techniques which are being explored for the fabrication of soft structures. Holographic interference lithography has been recently employed to fabricate polymer based hypersonic crystalline structures.[9, 23] The phononic dispersion relation of such single crystalline triangular arrays of cylindrical holes in an epoxy matrix[24] measured by spontaneous Brillouin light scattering[1] did not reveal the anticipated band gap, probably being obscured by the strong optical diffraction. In this work I adopt a previously developed self-

assembly technique[25, 26] by vertical lifting deposition to fabricate fcc single crystalline colloidal films of monodisperse polystyrene (PS) nanospheres on glass substrates. These soft PS opals were subsequently infiltrated by fluids with different sound velocities. Using BLS to map the dispersion relation of the longitudinally polarized phonons in such colloidal crystals, my coworkers and I present the first experimental observation of a hypersonic band gap.

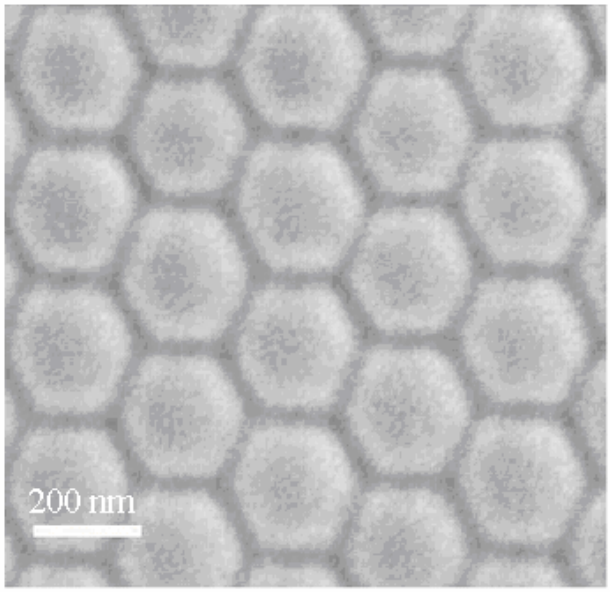

Fig. 4.8: SEM image of the silicon oil infiltrated wet PS opal, D is 256nm.

The infiltration of the dry opal by fluids with a refractive index close to that of PS eliminates the multiple light scattering and hence leads to a well-defined **q**. The resulting wet opal made up of close-packed PS spheres (fcc) with the interstices fully occupied by the liquid, represents a hypersonic crystal of solid inclusions in a fluid host, as shown in the SEM image in Figure 4.8 for the opal with d=256 nm infiltrated by silicon oil. It is desirable to probe the dispersion relation $\omega(\mathbf{q})$ along the high symmetry directions in the reciprocal space, since the phononic band gap is usually manifested in the dispersion diagrams along these directions.[2,3,27] In our case, the first Brillouin zone (BZ) of the fcc lattice (of which the reciprocal is bcc) is a truncated octahedron with its center denoted by Γ and the corresponding highest symmetry directions pointing from Γ to the zone face centers, i.e. along Γ-L and Γ-X as shown in Figure 4.9. In the scattering geometry of Figure 4.3, all possible experimental **q** vectors are confined in a plane, whose intersection with the BZ forms a hexagon (blue line Figure 4.9). Therefore it is unlikely to follow strictly the phonon propagation

along Γ-L or Γ-X. Nevertheless, the direction of **q** can be selected close to Γ-L, as along Γ-M, where M denotes the edge centre of the hexagon as defined above. In this case, the probed dispersion diagram should show no essential difference from the Γ-L direction, since on a given zone face the band splitting near the face center is roughly constant, as can be shown by first-order perturbation theory[28].

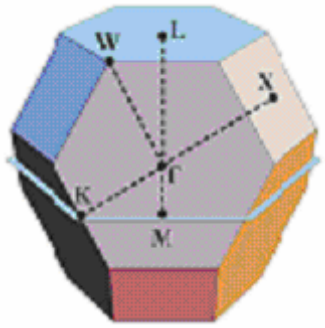

Fig. 4.9: Scheme of the first Brillouin zone (BZ) for fcc lattice, with the blue hexagonal line indicating the plane of all experimental scatteing vector.

Figure 4.10 shows polarized Brillouin spectra of the wet opal infiltrated by silicon oil with particle diameter d=256 nm, taken at five different values of q near the BZ boundary along the Γ-M direction. Apparently, a double peak feature appears in all these spectra, and this can be well represented (red line) by a double Lorentzian line shape (violet and green lines, convoluted with the instrumental function), the violet line indicates the mode with acoustic-like behaviour. The splitting of the single peak feature at low q (long wavelength) into double peaks across the BZ boundary is a typical Bragg-gap effect due to the band folding into the first BZ. The observed acoustic phonons are longitudinally polarized, as they disappear in the depolarized Brillouin spectrum. However, the concurrent absence of the transverse phonons in the depolarized spectrum is consistent with the nature of this phononic system, since the infiltrated fluid does not support shear waves.

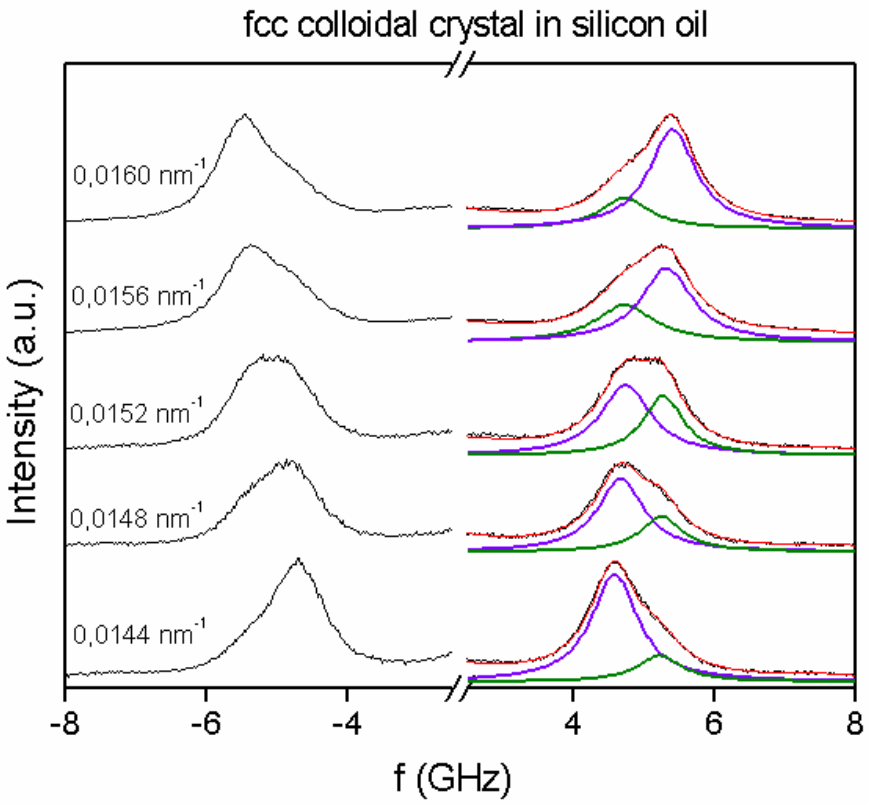

Fig. 4.10: Phonon propagation in the fcc wet opals at the egdes of the Brillouin zone. Brillouin light scattering spectra of the PS(256nm)/silicon oil wet opal for the indicated wave vectors vectors q in the vicinity of the BZ edge in the direction ΓL. The deconvolution in two spectral components (the acoustic branch in violet) is indicated for the Stokes side of the spectrum.

A more complete knowledge of the phonon propagation can be obtained by referring to the measured dispersion relation $\omega(\mathbf{q})$ as depicted in Figure 4.11. The two dashed gray lines indicate the acoustic phonon propagation in pure PS and silicon oil, which are measured independently. The slope of these lines yields the sound velocity ($c=\omega/q=2\pi f/q$) in the respective medium; c amounts to (1400±25) m s^{-1} in silicon oil. In the hypersonic crystal, only one longitudinal acoustic phonon branch is observed at low frequencies. The corresponding dispersion curve, $\omega(\mathbf{q})$, is linear and thus describes sound propagation in a homogeneous effective medium, as anticipated for long wavelengths exceeding the lattice spacing. The slope of this line yields an effective sound velocity c_{eff}=(1950±40) m s^{-1}, which is intermediate between the sound velocities in the two component materials. The most striking feature of the dispersion relation is the presence of a clear Bragg gap at frequency 5 GHz with a

width about 0.4 GHz for $q \approx 0.015$ nm^{-1} which matches the distance Γ-M. Correspondingly, propagation of hypersonic phonons with frequencies within the marked blue region in Figure 4.11 is forbidden in the present wet opal with a sound velocity ratio of about 1.7 between the particle and the fluid. It is remarkable that, after infiltration, no particle eigenmodes are observed which could, in principle, lead to a hybridization gap between the continuum acoustic band and the l=2 resonance band as predicted theoretically.[29] The absence of particle eigenmodes might relate to the weaker elastic contrast between the constituent media of the wet opals and hence stronger leakage of the elastic field energy into the surrounding liquid.

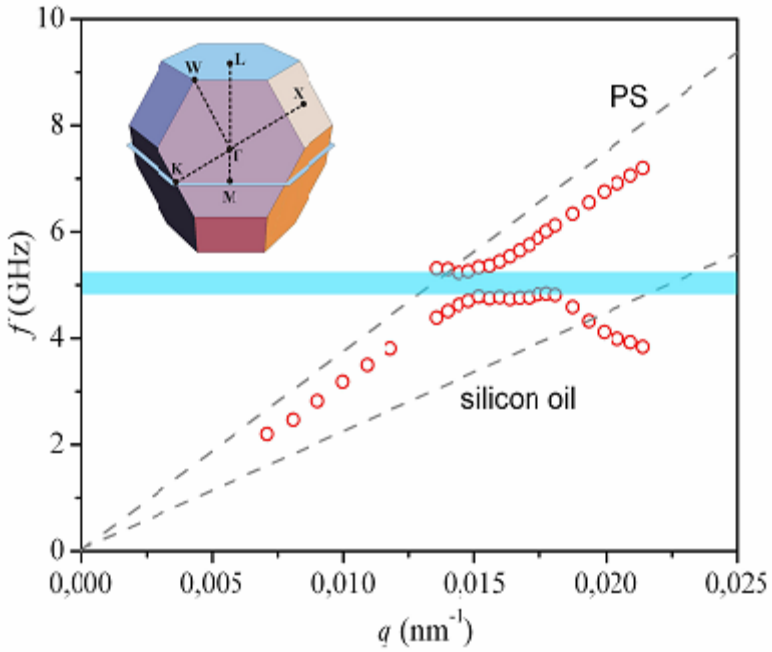

Fig. 4.11: Phononic gap in the dispersion relation. The dispersion f vs q plot with **q** lying in the (111) plane .The observed gap of about 0.4GHz (blue stripe) is along the ΓL direction in the bcc reciprocal lattice shown in the inset. The **q**-direction is in the plane passing through K and the center Γ of the BZ (inset). The effective medium longitudinal speed of sound $c_L = 2\pi f/q$ (at low q's) is intermediate between the sound velocities in the pure PS and liquid matrix components presented by the slopes of the two dashed lines.

The width of the Bragg gap in Figure 4. 11 should be directly related to the difference between the sound velocities and the densities of the component materials in this phononic structure[1-3]. Since most soft materials have comparable low densities, it is the sound velocity contrast that matters. Hence, the gap width should depend on

the elastic contrast between the fluid matrix and the PS particles. In addition to silicon oil, glycerol and low molecular mass PDMS were also used as matrix fluids, both of which have notably different sound velocities from silicon oil. In PDMS, c=(1050±20) m s^{-1} is virtually **q**-independent whereas in glycerol c increases from 2000 m s^{-1} at ultrasonic to 2500 m s^{-1} at hypersonic frequencies due to structural relaxation in the GHz frequency range at ambient temperature[30]. The sound velocity in these three matrix fluids was computed from their Brillouin spectra, e.g. as shown in Figure 4.12 a) in which all spectra were recorded at similar q; for comparison the spectrum of a bulk PS sample is also shown. The unusually high sound velocity in glycerol (comparable to that in PS) is mainly due to its remarkably strong hydrogen-bonding network that slows down the structural relaxation, i.e. from the sub-THz to the GHz domain, thus leading effectively to a solid-like behavior at hypersonic frequencies. The very different phonon attenuation in these fluids is directly reflected in the line width of their Brillouin spectra and this disparity could help understand and ultimately control the losses in phononic crystals.

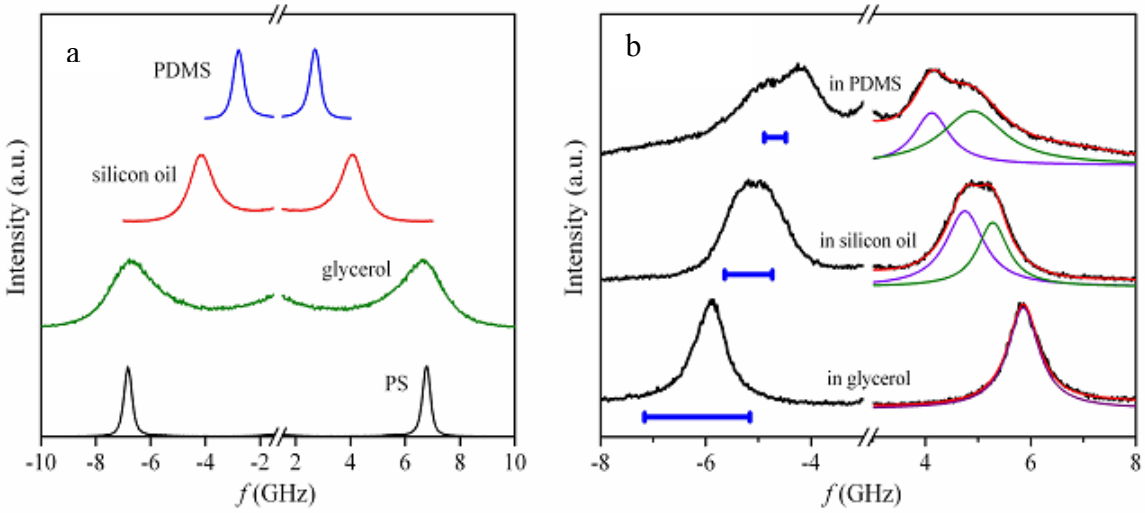

Fig. 4.12: a) Brillouin light scattering spectra of the PS (256nm) colloidal crystal in three different matrices as indicated in the plot at q=0.0152nm^{-1} directed near ΓL at the center of the hexagon in the reciprocal lattice (inset to Figure 4.9). The elastic contrast between PS and the matrices strongly controls the separation of the two modes and hence the width of the gap; in glycerol the gap almost disappears. The deconvolution of the spectra shows that the line width of the two modes is not related to the losses in the pure matrices indicated by -| |- the full width at half height of the spectrum. This clear trend follows the elastic contrast between PS and pure liquids as reflected in the Brillouin spectra of the pure components at 0.017nm^{-1}

The influence of the fluid matrices on the band gap becomes apparent in the Brillouin spectral shape in Figure 4.12 b), recorded at the BZ boundary (q=0.0152 nm^{-1}) along Γ-M for three phononic crystals with different liquid infiltration. The elastic contrast between PS and the liquid matrices clearly controls the splitting of the two peaks and hence the width of the gap. In the PDMS opal, the two peaks exhibit the largest separation, in contrast to the glycerol opal where only a single peak is discernible suggesting a negligibly small gap. This clear trend follows the elastic contrast between PS and the pure liquids shown in Figure 4.12a). There is no obvious correlation, however, between the line width in the phononic crystals and that in the corresponding infiltrated liquids, marked by the blue bars, which were measured at about the same q. Instead, the phonon damping in the opal infiltrated by a fluid with strong sound attenuation, e.g. glycerol, is significantly suppressed, and vice versa. Since the attenuation of acoustic waves in glassy PS is very weak, as indicated by the narrow Brillouin peak (Figure 4.12a), the origin of the hypersonic sound attenuation in the phononic crystals and in the pure matrix fluids should be different. In the former, the attenuation of phonons appears to relate to the elastic mismatch between the matrix fluid and PS particles as it increases with the elastic constant contrast**.** Large elastic contrast leads to strong scattering of phonons at the interface between the component materials. On the other hand, the stronger the scattering of phonons, the shorter is the mean free path, and thus the Brillouin line width increases.

The successful tuning of the band gap in hypersonic phononic colloidal crystals by means of different infiltration media is even more apparent in the combined dispersion relations of Figure 4.13. These are plotted in reduced scales, $\omega a/2\pi c_{\text{eff}}$ vs $(2/3)^{3/2} qa/\pi$, where c_{eff} is the effective medium phase sound velocity for the three wet opals, a is the lattice constant of the fcc crystal ($a=\sqrt{2}\,d$), and $(3/2)^{3/2}\pi/a$ is the distance Γ-M in the reciprocal space. The successful overlap of the acoustic branch at low q in all the three phononic crystals results from the different experimental values of c_{eff} decreasing from (2400±50) m s^{-1} in glycerol-infiltrated to (1670±30) m s^{-1} in the PDMS-infiltrated opals. This trend is expected since the disparity between the PS sound velocity and the fluid sound velocity increases from glycerol to PDMS (Figure 4.12a). For the wet opals with distinct elastic contrast between the constituent media, c_{eff} can be captured by the effective medium theory[31] of elastic composites consisting of a fluid host with solid (PS) inclusions. With no adjustable parameter, using the

experimental densities and the sound velocities of the constituent media, the computed c_{eff} is about 8% lower than the experimental values. This moderate deviation might relate to the neglect in the theory of sound dissipation and possible contacts of the solid inclusions at this high packing density.

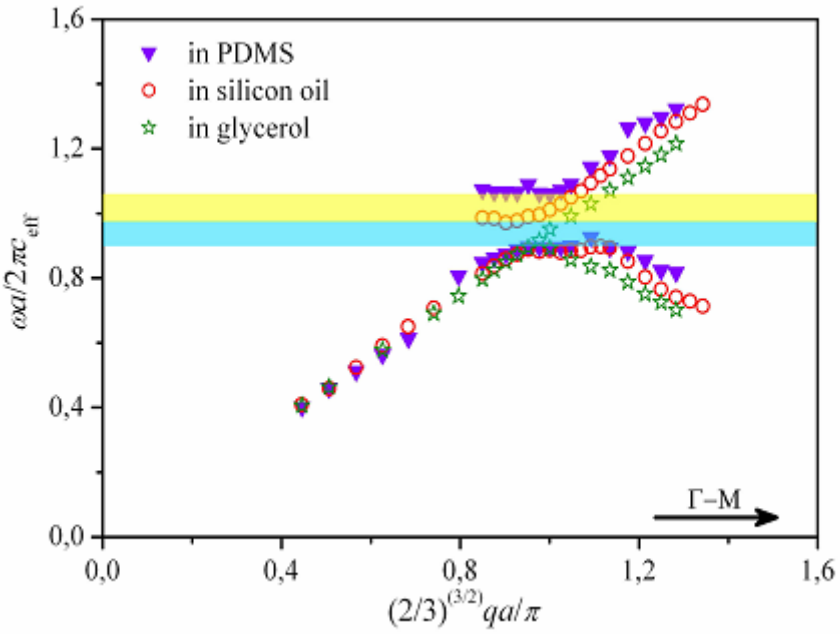

Fig. 4.13**:** Tuning of the phononic gap with infiltration**.** The dispersion plot in a f/c_L vs q presentation, where c_L is the effective medium phase sound velocity for the three PS (256nm) infiltrated colloidal crystals at the edge of the BZ near L (see Figure 4.9).The biggest gap with 0.8 GHz (colored bands) is observed for the PDMS matrix, whereas there is no discernible gap in glycerol.

The tuning of the band gap can be further achieved by changing the periodicity of the phononic crystal while maintaining the elastic parameters of the component materials. Benefiting from our well-controlled self-assembly of fcc colloidal crystals, this can be easily accomplished by varying the size of the monodisperse PS nanospheres. The measured dispersion relations for longitudinal phonons traveling in two phononic colloidal crystals of two different PS diameters along the same crystallographic direction Γ-M are displayed in Figure 4.14. Obviously, the central frequency of the gap f_c as well as its width Δf can be tuned with the particle diameter. Long wavelength (low q) longitudinal phonons see the same effective medium and thus expectedly propagate with the same velocity, c_{eff}=(1950±40) m s^{-1}, in both systems. We make use of this value to map the experimental dispersion of Figure 4.14

on the band structure diagram of a fcc phononic crystal. With no adjustable parameter, indeed, both systems exhibit the same band gap along the same Γ-M direction, suggesting that the frequency f_c and the width of the Bragg gap Δf are inversely proportional to the lattice parameter. Therefore, these phononic crystals forbid wave propagation with wavelengths commensurate to their lattice periodicity. This result is a direct consequence of the invariance of the wave equation of elasticity under the simultaneous transformation of space coordinates and frequency: $\mathbf{r} \rightarrow s\mathbf{r}$ and $f \rightarrow f/s$, where s is an arbitrary scaling parameter, for any inhomogeneous system characterized by frequency-independent elastic coefficients

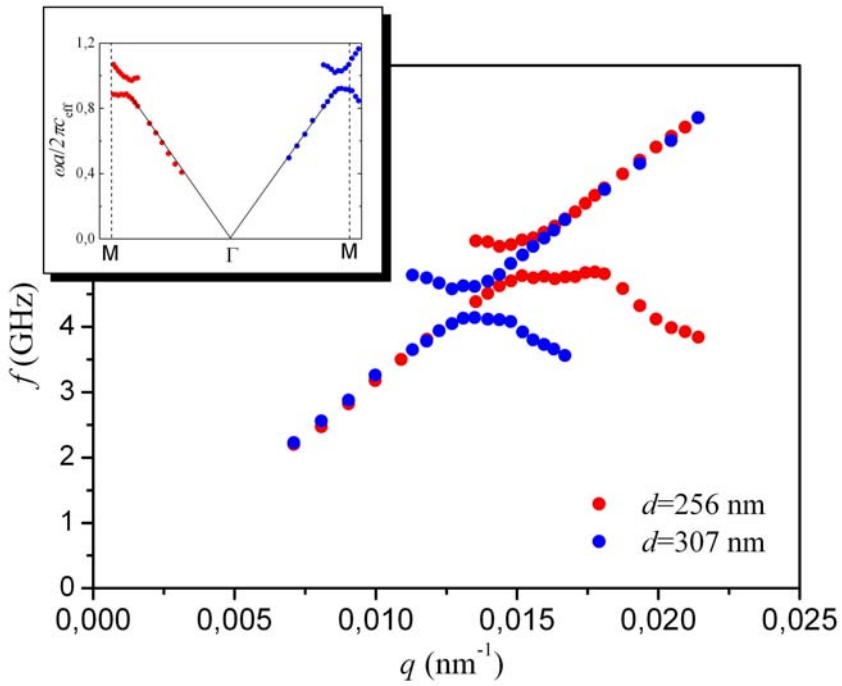

Fig. 4.14: Tuning the gap with particle diameter**.** The dispersion relation, f vs q, for two PS/silicon oil phononic crystals with 256 nm and 307 nm PS particle diameter. Inset: The band structure diagram for the systems of the main plot.

4.6 Conclusions

My coworkers and I demonstrate that high resolution Brillouin spectroscopy can reveal a large number of vibration eigenmodes of submicrometer particles in synthetic soft opals. All these hypersonic frequencies are identified by spherical harmonics $Y_{lm}(\theta, \varphi)$ angular dependence and the radial $R_i(r)$ variation in analogy to the atomic orbitals. The peculiar line shape of the low frequency modes is a sensitive index of the particle size distribution.[32]

As colloidal particle crystals are considered for an increasingly number of potential applications in photonics for optical signal and data processing and sensor applications, the establishment of a nondestructive high resolution optical technique opens new means for micromechanical characterization in phononic and photonic structures in the spectral region of visible light.

This first realization of hypersonic phononic crystals based on a self-assembling of colloidal particles provides opportunities with regard to both such class of materials and applications, in a rapidly evolving new (about ten years old) field. It demonstrates the direct measurement of the phononic dispersion relation using an optical technique that also allows the study of fundamental issues of phonon dissipation in these materials. [33]

References

1 Joannopoulos J. D., Villeneuve P. R., Fan, S. H. *Nature* **1997**, *386*,143.

2 Sigalas M., Economou E. N., *Solid State Commun* **1993***, 86*, 141.

3 Kushwaha M. S., Halevi P., Dobrzynski L., Djafari-Rouhani B. *Phys. Rev. Lett.* **1993**, *71*, 2022.

4. Marinez-Sala R.,Sancho J.,Sanchez J.V., Gomez, V., Liinares,J., *Nature* **1995**, *378*, 241.

5. Montero de Espinoza F. R., Jimenez E., Torres M., *Phys.Rev.Lett*.**1998**, *80*,1208.

6. Liu Z., Zhang X., Mao Y., Zhu Y. Y., Yang Z., Chan C. T., Sheng P., *Science* **2000,** *289*, 1734.

7. Vasseur J. O., Deymier P. A., Chenni B., Djafari-Rouhani B., Dobrzynski L., Prevost D., *Phys.Rev.Lett*. **2001**, *86*,3012.

8. Gorishnyy T., Ullal C. K., Maldovan M., Fytas G., Thomas E. L., *Phys.Rev.Lett*. **2005,** *94*, 115504.

9. Gorishnyy T., Maldovan M., Ullal C., Thomas E. L., *Physics World* **2005,** *18*, 25.

10 Kriegs H., Steffen W., Fytas G, Monako G., Dreyfus C., Pitzicalis M., Hadjichristidis N., *J.Chem.Phys*. **2004**, *121*, 2376.

11 Liu J., Ye L., Weitz D. A., Sheng P., *Phys.Rev.Lett*. **1990**, *65*, 2602.

12 Penciu R. S., Kiegs H., Petekidis G., Fytas G., Economou d E. N., *J.Chem.Phys*. **2003**, *118*, 5224.

13 Saviot L., Murray D. A., *Phys.Rev.Lett*. **2004**, *93*, 217801.

14 Kuok M.H., Lim H. S., Ng S. C., Liu N. N., Wang Z. K., *Phys.Rev.Lett*. **2003**, 90, 255502.

15 Urbas A, Thomas E. L., Kriegs H, .Fytas G., Penciu R. S., Economou E. N., *Phys.Rev.Lett*. **2003**, *90*, 108302.

16 M.de Billy J., *Acoust.Soc.Am*. **2001,** *110,* 710.

17 Cheng Z., Zhu J., Russel W. B., Chaikin P. M., *Phys.Rev.Lett*. **2000**, 85, 1460.

18 Hoppenbrouwers M., Water W. van de, *Phys.Rev.Lett*. **1998**, *80*,3871.

19. Duval E., Bourkenter A., Shampagnon R., *Phys.Rev.Lett*. **1986**, *56*, 2052.

20 Ikezawa M., Okuno T., Masumoto Y., Lipovskii A. A., *Phys.Rev.B* **2001**, *64*, 201315R.

21 Kent, A. J. *et al. Phys. Rev. Lett.* **2006**, *96*, 215504.

22 Maldovan, M., Thomas, E. L. *Appl. Phys. Lett.* **2006**, *88*, 251907.

23 Jang, J. H., Ullal, C. K., Gorishnyy, T., Tsukruk, V. V., Thomas, E. L. *Nano Lett.* **2006**, *6*, 740.

24 Joannopoulos, J. D., Meade, R. D., Winn, J. N. *Photonic Crystals: Molding the Flow of Light* (Princeton Univ. Press, New Jersey, **1995**).

25 Gu, Z., Fujishima, A., Sato, Osamu., *Chem. Mater.* **2002**, *14*, 760.

26 Fustin, C.-A., Glasser, G., Spiess,H. W., Jonas, U.. *Langmuir* **2004**, *20*, 9114.

27 van Tiggelen, B. A. & Skipetrov, S. E. (Eds.) *Wave Scattering in Complex Media: From Theory to Applications* (Kluwer Academic Publishers, Dordrecht, **2003**).

28 Ashcroft, N. W. & Mermin, N. D. *Solid State Physics* (Saunders College Publishing, New York, **1976**).

29 Psarobas I. E., Modinos A., Sainidou R., Stefanou N., *Phys. Rev. B* **2002**, *65*, 064307.

30 Giugni A., Cunsolo A., *J. Phys.: Condens. Matter* **2006, *18,*** 889.

31 Gaunaurd, G. C., Wertman. W., *J. Acoustic. Soc. Am.* **1989**, *85*, 541-554.

32 Cheng W., Wang J., Jonas U., Fytas G., Penciu R. S., Economou E. N, *J. Chem. Phys.* **2005**, *123,* 121104.

33 Cheng W., Wang J., Jonas U., Fytas G., Stefanou N., *Nature Materials* **2006***, 5,* 830.

Chapter 5 Application of Colloidal Crystals

5.1 Inverse Opals of Polyaniline and its Copolymers Prepared by Electrochemical Techniques (This work was done in cooperation with Dr. S. Tian)

5.1.1 Introduction

Recently, sacrificial template methods[1-7] have been shown to offer an effective approach for the fabrication of structured materials with unique properties that are difficult to produce by traditional patterning procedures (like photolithography,[8] soft lithography,[9-10] dip-pen nanolithography,[11] holographic patterning,[12] etc.). The templates normally used include diblock copolymers,[13-16] anodized alumina layers,[17-20] organic or inorganic colloidal crystals,[21-23] and others.[24-25] Among these, self-assembled colloidal crystals (synthetic opals) stand out as ideal templates for creating highly ordered three-dimensional (3D) structures with interconnected macropores (the so-called “inverted opals” or “inverse opals”), which show potential for applications ranging from photonic crystals to catalysts and bioreactors.[26-35] To date, inverse opals from numerous materials, such as metals,[36-37] inorganic oxides,[21-23] or polymers,[31-32,35,38-42] have been fabricated using a variety of colloidal crystal templates.

The original interest for preparing inverse opals with conjugated polymers originated from the motivation to obtain photonic bandgap crystals with enhanced interaction with light. The ease of tuning the refractive index of the conjugated polymers[38-39] suggested to use them as model systems to investigate how the periodic structure of the crystal mutually enhances the optoelectronic properties of the polymer and vice versa. Recently, considerable research interest also focused on their potential applications for biosensing purposes, by exploiting the advantages provided by the highly ordered porous structure and the huge surface area they posses.[31-35]

Until now, inverse opals based on different conjugated polymers, such as polypyrrole,[32,40,43] polythiophene,[31,43] polyphenylenevinylene,[38,39] and polyaniline,[44] have been prepared by polymerizing the corresponding monomers either wet chemically or electrochemically in the interstitial voids of the colloidal crystal template. Compared to the wet chemical synthesis, electrochemical polymerization

allows for a much better control of the structural quality of the inverse opal (e.g. uniformity of the film thickness and size of interconnected pores.) by controlling the polymerization time and the applied potential or current.[31-35,38-42,43-44]

Here, in cooperation with Dr. Tian, I apply two electropolymerization methods to prepare polyaniline (PANI) inverse opals by using polystyrene (PS) colloidal assemblies as sacrificial templates. A chemical polymerization method for the preparation of inverse PANI opal was reported previously by Caruso and his coworkers.[44] However, due to the inherent drawbacks of the method used (as discussed further below), the quality in terms of defect density and detailed structural integrity of the obtained PANI inverse opals was somewhat poor. Moreover, the loss of redox activity of PANI in neutral solutions[45, 46] also precludes the use of such pure PANI inverse opaline sturctures for biosensing applications. It has been demonstrated, however, that the redox activity of PANI can be sustained in neutral pH solutions by doping it with different polyanions (such as poly(styrenesulfonate), PSS)[47-52], modified gold nanoparticles[53,54], or modified carbon nanotubes.[55] By using electropolymerization, Dr. Tian and I demonstrate that PANI inverse opals can be obtained with much higher quality. Furthermore, by controlling the polymerisation time, it can be exactly controlled whether the topmost layer of the inverse opal is open or closed. Finally, efforts are also directed towards preparing inverse opals of PANI composites by electrocopolymerizing aniline in the presence of different dopants, in order to explore their potential for biosensing applications.

5.1.2 Polyaniline (PANI)

It reflects scientific and technological importance of the conducting polymers that the 2000 Noble Price in chemistry went to Alan J. Heeger, Alan G. Macdiarmid and Hideki Shirakawa "*for the discovery and development of conductive polymers" (noble citation)*.[56] Among the conducting polymers, polyaniline stands out as one of the most important ones, because of its ease of preparation, environmental stability, affordability, and wide application as the active electrode materials in energy storage,[58] opto-electronic devices,[59] display devices,[60] and chemical and biochemical sensors.[61,62] Molecularly, PANI is of particular interest due to the presence of the chemically flexible –NH- group in the polymer backbone, which not only takes part in protonation and deprotonation but also contribute to π bond formation.[63] It is widely accepted that PANI is a mixed oxidation state polymer consisting of a reduced benzenoid units and a oxidized quinoid unit (Figure 5.1 A), with the average oxidation state given by (1-y).[64, 65] It can exist in several oxidation states ranging from the completely reduced leucoemeraldine base state (LEB) (Figure 5.1 (B)), where 1-y=0, to the completely oxidized pernigraniline base state (PNB), where 1-y=1. The half oxidized (1-y=0.5) emeraldine base state (EB) has always been written as a series of alternating two benzenoid units and one quinoid unit. The above three PANI forms have insulating properties, but the emeraldine base state can be reversibly transformed to a conducting form, the emeraldine salt (ES) form, if EB is non-redoxly doped with acid. In this process, the imine nitrogen atoms of the polymer are protonated to give a polaronic from where both spin and charge are delocalized along the entire polymer backbone. This is different from the redox-doping ones through which ES can also be obtained from its corresponding LEB form or PNB form by either a chemical or an electrochemical step in acidic conditions (Figure 5.1 (B)). It has been reported that if all carriers contribute to the conductivity, the room temperature conductivity of the PANI would be comparable to that of copper (~10^5 S/cm)[66].

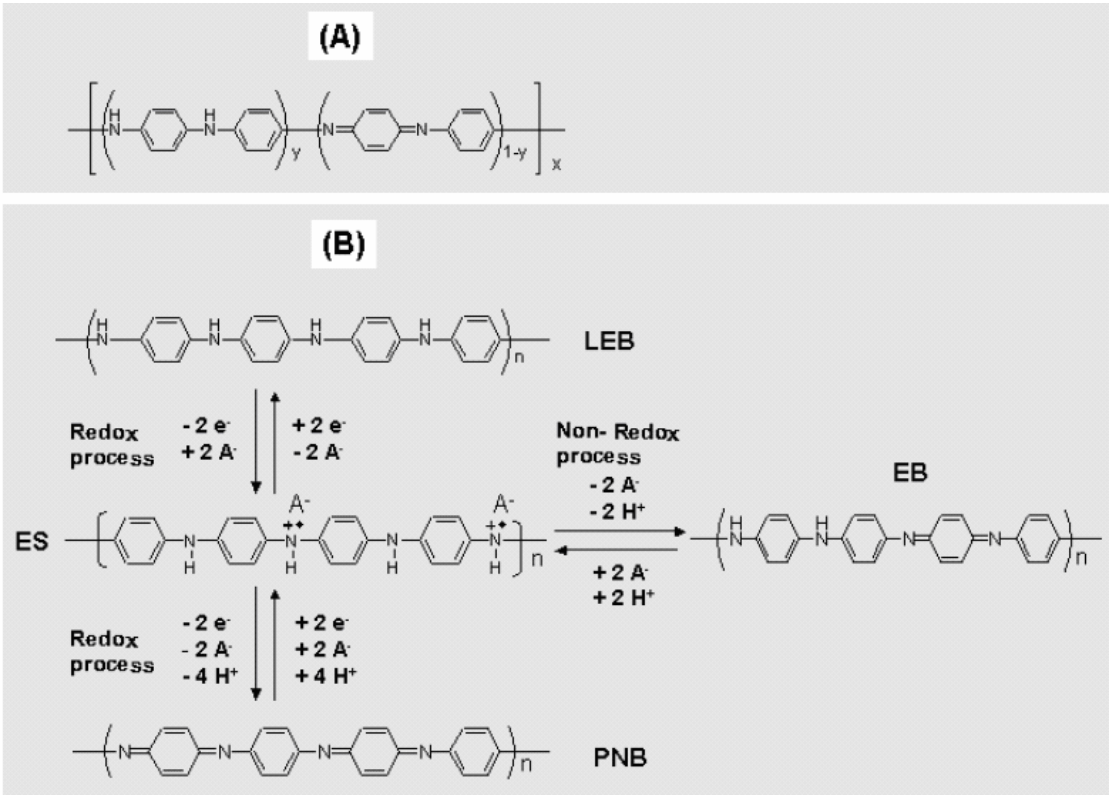

Fig. 5.1: A) the general chemical structure of PANI. B) the chemical structure of the three oxidation states of PANI, and the transition scheme from them to the conductive emeraldine salt.

5.1.3 Synthesis of PANI by Electropolymerisation with mCC Templates

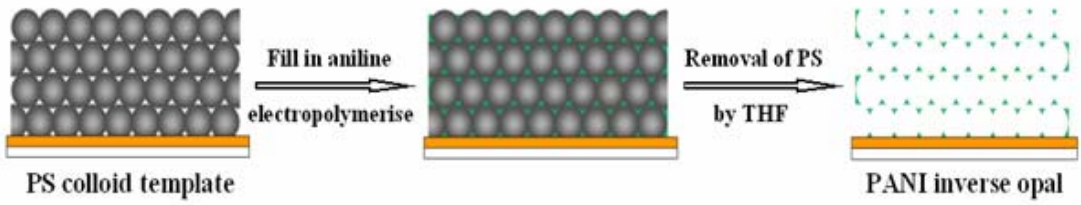

Fig. 5.2: Schematic illustration of the procedure used for fabricating PANI inverse opals.

The electropolymerisation and electrochemical measurements were performed with an EG&G 273A potentiostat, with the PS colloidal assembly-loaded Au substrate as the working electrode, a coiled platinum wire being used as the counter electrode, and

an Ag/AgCl (3 M NaCl) electrode as the reference electrode. All potentials reported here are with respect to this reference electrode. The morphologies of the colloidal crystals and inverse opals were imaged with a low voltage scanning electron microscopy.

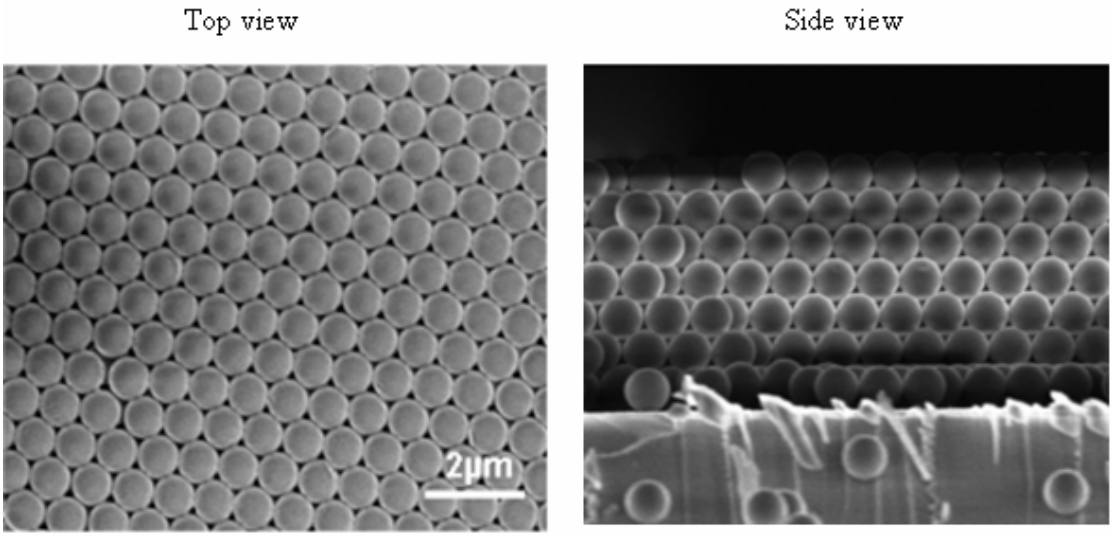

Fig. 5.3: Typical SEM images of a 3D PS colloidal crystal template prepared by vertical lifting deposition on gold surface.

The fabrication procedure of the PANI inverse opals by electropolymerisation using the PS colloidal templates is shown in Figure 5.2. The colloidal crystal templates shown in Figure 5.3 were fabricated on Au substrates (50 nm Au evaporated onto LaSFN9 glass slides with a 2 nm Cr adhesion layer in between) by a vertical lifting deposition from the colloidal suspension (0.5 wt %-2.5 wt %) on a home made dipping device described in Chapter 3.[67,68,69] In order to increase the wettability of the Au substrate, it was pre-functionalized with a layer of hydrophilic thiol (normally 3-macapto-1-propanesulfonic acid). After flooding the interstices of the PS colloidal template with aniline solution (0.02 M aniline in 0.5 M H_2SO_4), electropolymerisation was carried out by either a galvanostatic method or by cyclic voltammetry. After polymerisation, the resulting polymer film was thoroughly rinsed with 0.5 M H_2SO_4, then exposed to a tetrahydrofuran (THF) solution for ~ 10 h in order to remove the PS template and to obtain the well-structured PANI inverse opals. The entire preparation process above was carried out in an electrochemical cell.

The polymerisation process is assumed to proceed via the following mechanism:[57,67]

First, the radical cation is formed through an electron transfer from the 2s energy level of the nitrogen atom in aniline as shown in Figure 5. 4. Among the possible resonant forms, (c) is the most reactive because of the substituting inductive effect and absence of the steric hindrance.

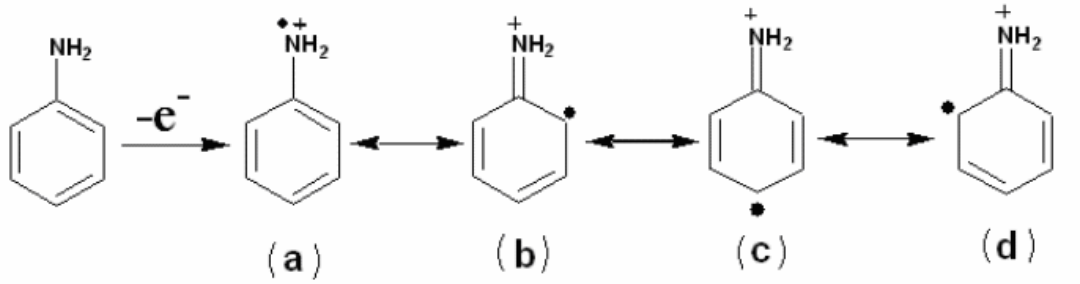

Fig. 5.4: Formation of the aniline radical cation and all possible resonant structures

Second, the so called “head to tail” reaction between the radical cations (mostly form (c)) in acidic medium leads to the formation of dimers by eliminating two protons. This results in new radical cation dimers through the oxidization at the required potential, thus the radical cation of the monomer reacts to build up the aniline chain. The entire process is depicted in Figure 5.5 and Figure 5.6.

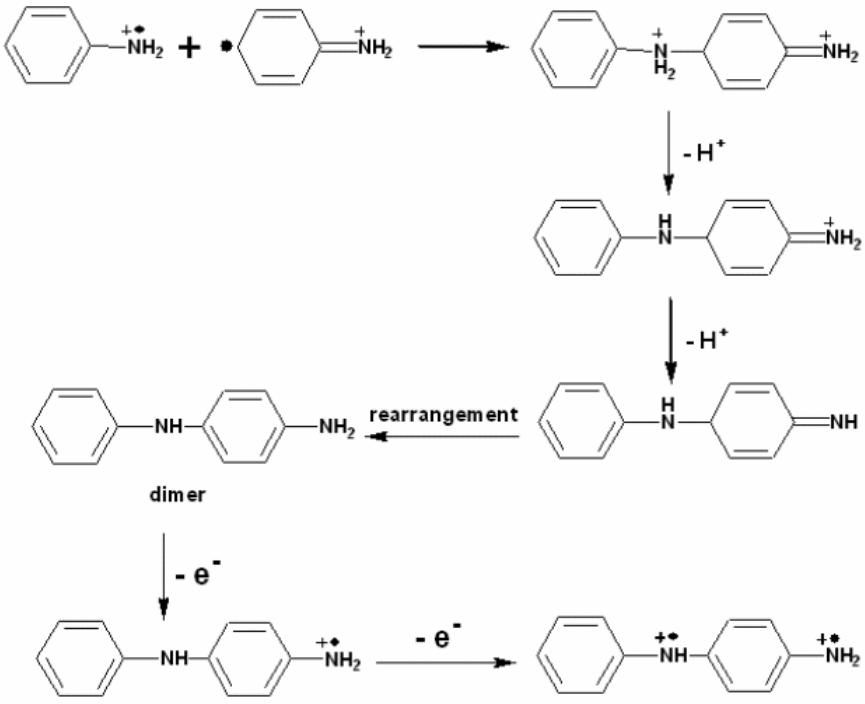

Fig. 5.5: Formation of aniline dimer and its radical cation.

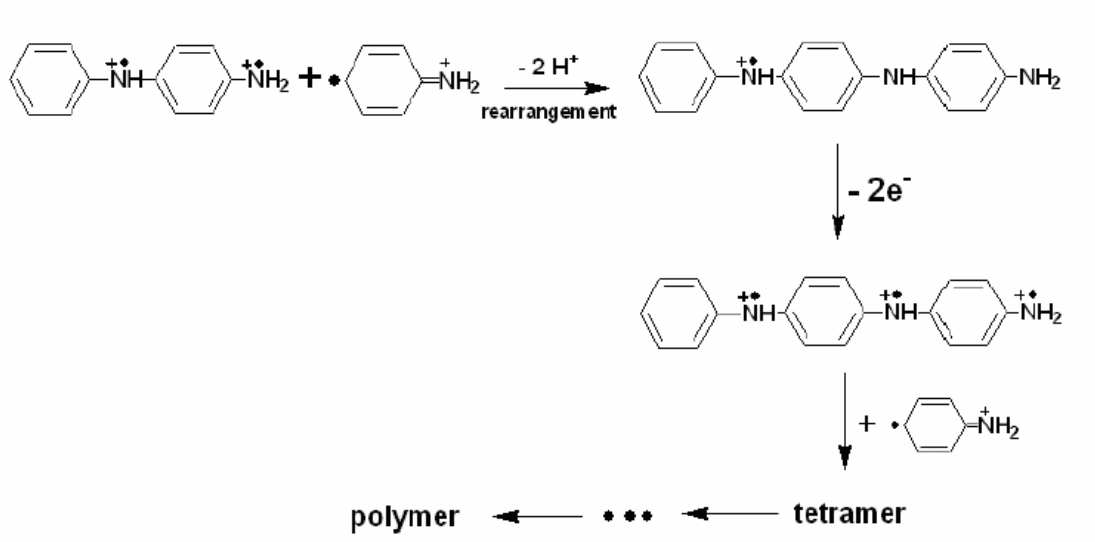

Fig. 5.6: One possible way of the formation of PANI polymer.

5.1.3.1 Fabrication of Pure PANI Inverse Opals

SEM images of one sample of the PANI inverse opals fabricated by cyclic voltammetry at a scan rate of 20 mV/s for 10 cycles is shown in Figure 5.7. A well-ordered 3D network of PANI was obtained covering a very large area (~ 0.7 cm^2, limited only by the electrochemical cell). This PANI inverse opaline structure is believed to be held together by physical crosslinking and weak interactions, like hydrogen bonding and van der Waals forces between the PANI chains.[44] The enlarged image in Figure 5.7 (B) shows that the pores are assembled in a hexagonal array and are connected to each other via similarly symmetrical smaller pores, indicating a continuous mesoporous 3D structure typical for an inverse fcc lattice.

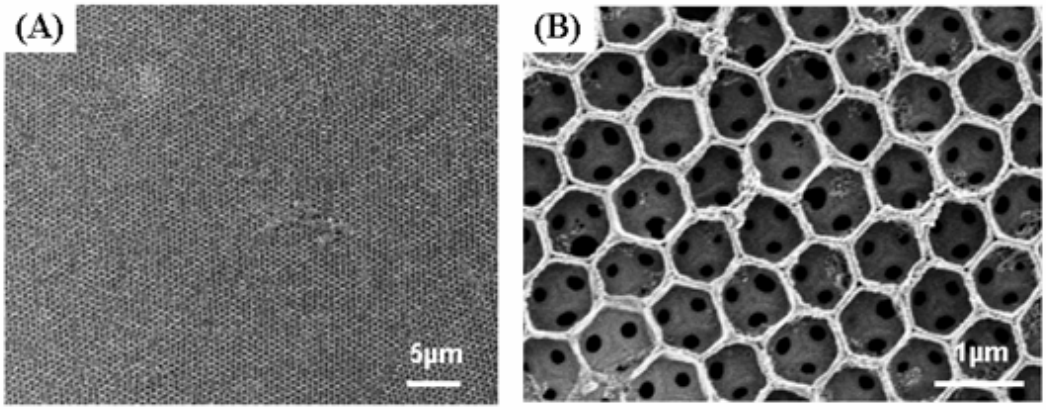

Fig. 5.7: SEM images of PANI inverse opals prepared via cyclic voltammetry, at low (A) and higher (B) magnification. The structure were formed using a CV scan rate 20 mV s^{-1} for 10 scan cycles

Compared with the wet chemical polymerisation method,[44] the quality of the PANI inverse opals prepared by this electropolymerisation method was greatly enhanced in terms of defect density and structural fidelity of the walls and voids. Furthermore, the shrinkage in our case (< 5%) is reduced to one-third of that obtained from wet chemical procedure (~ 15%), retaining almost the original geometry of the underlying PS template, which may also explain the low defect density over a very large area in the prepared inverse opaline films. In our case, the improved quality may arise from the well controlled polymerisation process by using a slow potential scan rate. This method allows the in-situ formation of PANI chains starting from the gold electrode at the base of the colloid crystal template to fill the interstices by a layer-type growth

mechanism in a highly ordered way and leading to a much more compact structure without blocking the pores above the PANI growth front. In contrast, the polymerisation rate in the wet chemical polymerisation approach via infiltration is more difficult to control, and isotropic polymerisation and precipitation may result in the aggregation of the formed PANI chains within all pores and packing into a relatively loose and disordered structure. Thus, further infiltration of monomer and oxidizer to increase the PANI loading is impeded. Actually, in our experiments, we found that the quality of the obtained PANI inverse opals decreased with increasing potential scan rate, possibly due to a very lose packing of the rapidly forming PANI chains. If the scan rate was too high, this could even lead to the collapse of the 3D structures after the removal of the PS colloidal template.

In a second polymerisation route, the PANI inverse opals were prepared by a galvanostatic method. By adjusting the polymerisation time and applied current this method allows for the exact control over the structure formation and film thickness of the PANI inverse opaline films obtained. Figure 5.8 shows the voltage changes during the electropolymerisation process along with the resulting film morphologies. The curve exhibits a transition point (TP) after which the voltage increases very sharply. A similar phenomenon was also found in the current changes seen during a potentiostatic preparation.[40, 70] This TP was ascribed to a rapid increase of the electrochemical reaction area once the growth front of the deposited material reached the template/bulk solution interface. This was confirmed in our experiments by stopping the polymerisation process at different stages as indicated by the arrows and taking SEM images of the PANI inverse opaline films obtained at each stage (also shown in Figure 5.8). If the polymerisation process was stopped at a very early stage ((a), after 10s), a bowl-shaped PANI array was obtained. At this stage, the thickness of the PANI layer formed is thinner than that of a PS particle monolayer (c.f. inset sketches for references). If the polymerisation process was stopped at a later stage ((b), after 200 s, but before the TP), an open 3D mesoporous structure resulted, with smaller channels connecting each cavity with its neighbours. The image (c) corresponded to the termination of the polymerisation process near the TP. It is clear, that right at the TP some of the pores at the top layer begin to close. If the polymerisation process is continued further, then all the pores of the topmost layer are closed by a complete PANI film. Beyond this point, hyperbranched PANI fibrils start to form on top of the closed pores ((d)). For practical purposes, an open 3D structure

like (b) is preferred to allow access to dissolved species into the interior of the mesoporous PANI inverse opal, so care must be taken to stop the polymerisation process before the TP (e.g. by monitoring the potential change during polymerisation).

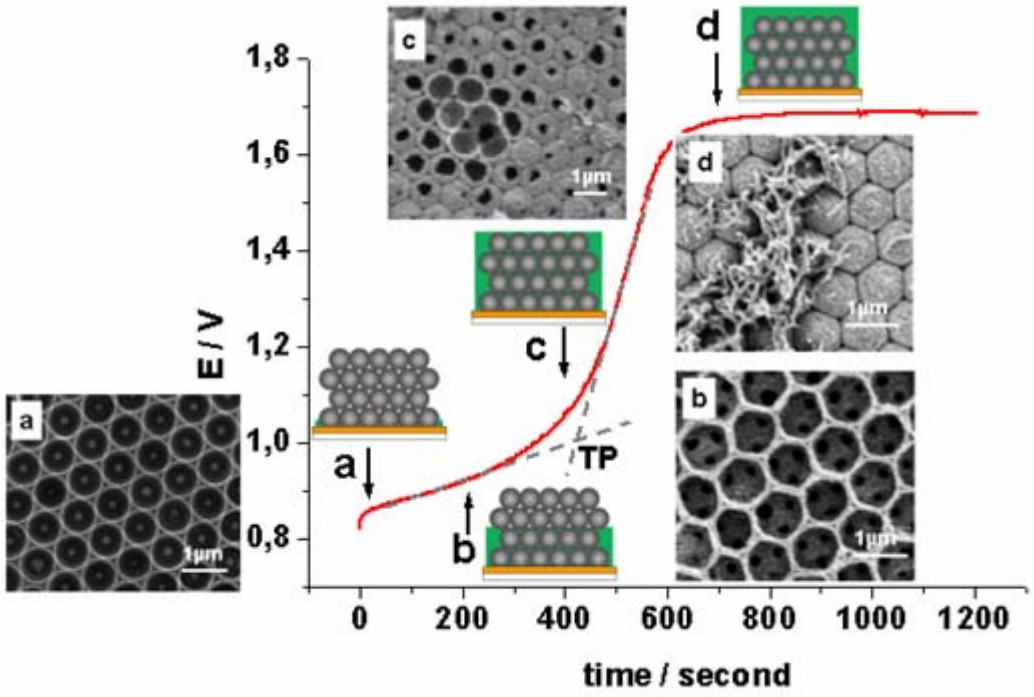

Fig. 5.8: Voltage changes during the electropolymerisation process for preparing PANI inverse opals by the galvanostatic method at a current density of 0.05mA cm^{-2}. Inset sketches show the status of the formed PANI inside the PS template at each stopping point as indicated by the arrows. SEM images of the corresponding PANI inverse films obtained at these points are also shown.

5.1.3.2 Preparation of PANI Composite Inverse Opals.

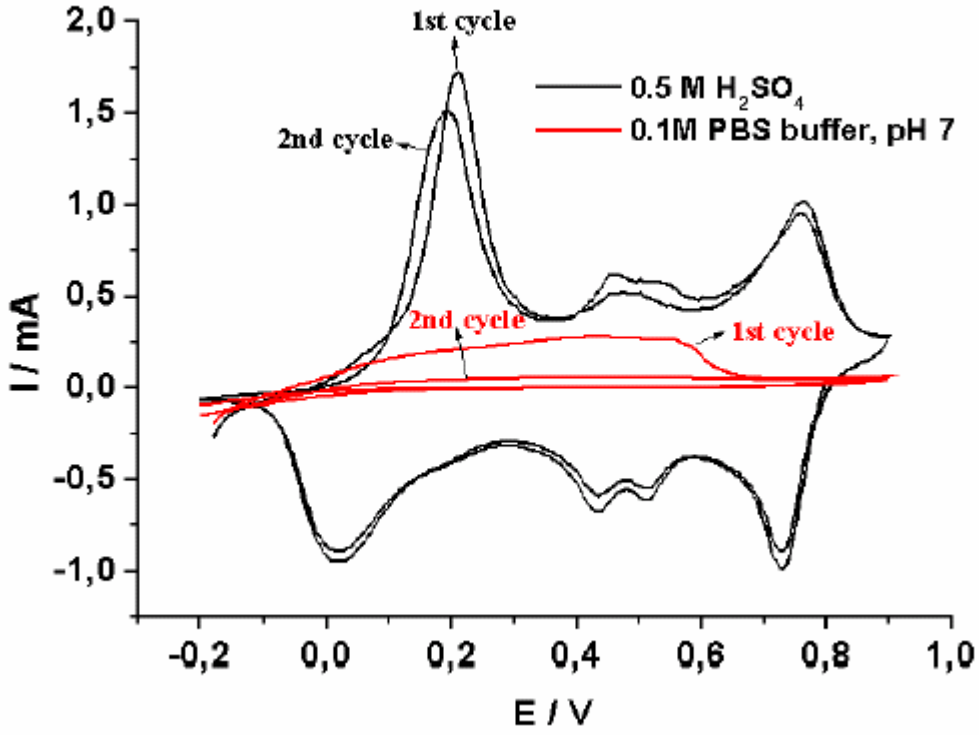

Fig. 5.9: Cyclic voltammograms of PANI measured in acidic and neutral pH solutions for two consective scans at a scan rate of 20mV/s.

Although many applications in chemical sensors for PANI have been reported,[71-75] literature about the direct application of PANI for biosensing purpose is limited.[76] This is because the redox activity of PANI can be maintained only in acidic environments and bioassays normally require neutral conditions. Electroactivity of PANI films both in acid and neutral conditions was measured and the results are shown in Figure 5.9. PANI shows redox activity in 0.5M H_2SO_4 solution, but if the same film was measured in pH7 PBS buffer solution, only a weak broad oxidative peak appeared in the first potential cycling, and even this peak disappeared in the second scan. Many efforts have been reported to solve this drawback, and can be devided into two main types:[77-79]

a) Introduction of the acidic groups such as –COOH, -SO_3H into the PANI chain, the so-called self-doping method. With this method, the micro-environment of nitrogen atoms in the PANI chain is changed and the local pH value is shifted

by the ionic groups introduced, and thus the electroactivity of the PANI is maintained at neutral conditions.

b) Using the negatively charged polyelectrolytes such as poly(acrylic acid), poly(vinyl sulfonate), poly(styrene sufonate) to dope the PANI during electrocopolymerisation is the second method. With this method PANI keeps the electroactivity because the trapped polyelectrolyte can protonate PANI in a broad pH range.

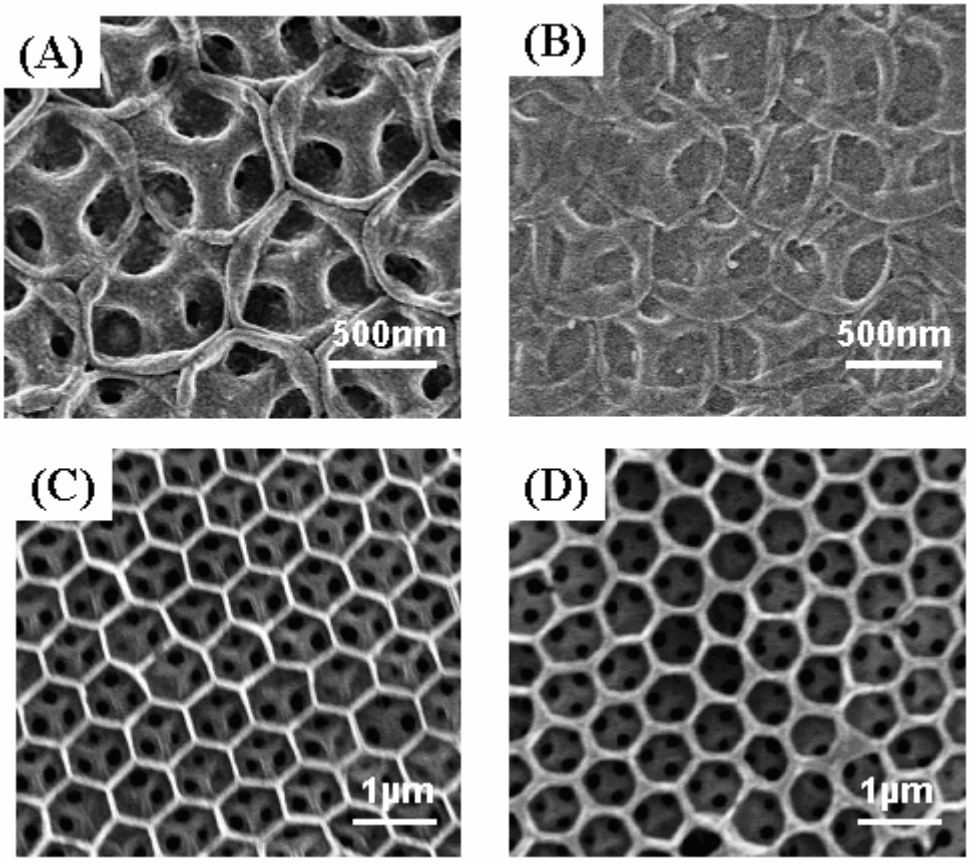

Fig 5.10: SEM images of PANI composite inverse opaline films by copolymerizing aniline with PAA (A), 2-ABA (B), or PSS (C) and (D). (A),(B), (C) were prepared via cyclic voltammetry at a scan rate of 20 mV s^{-1} for 10 cycles, while (D) was obtained by a galvanostatic method at a current density of 0.05 mA for 10 min. The concentration of PAA, PSS and 2-ABA is 0.02 M each.

In order to explore their applications for biosensing purposes, Dr. Tian and I also tried to fabricate PANI composite inverse opals either by doping with negatively charged polyelectrolytes,[47-52] or by copolymerizing aniline monomers with aniline derivatives containing acid groups, like 2-aminobenzoic acid (2-ABA). In this way,

we expected an inverse opaline film to form that remains electroactive at neutral pH. Shown in Figure 5.10 (A) and (B) are the SEM images of PANI composite inverse opaline films prepared by copolymerization of aniline with either PAA or 2-ABA, respectively, using the same growth conditions as those for pure PANI. From the SEM images it becomes clear that in both cases the structures obtained collapsed to some extent, especially the one of the copolymer with 2-ABA. We suspect this may be the poor mechanical properties of the dopants used or some phase separation occurring during the polymerisation process.

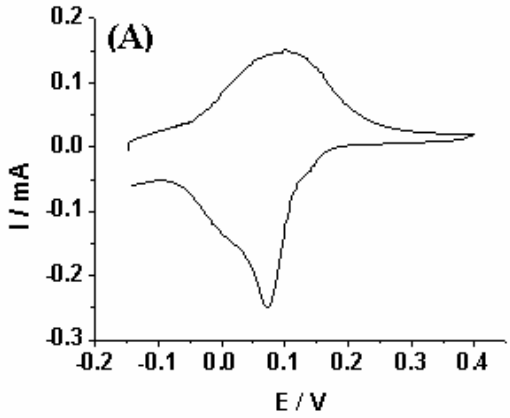

Fig. 5.11: Cyclic voltammogram of a PANI/PSS inverse opaline films as shown in Figure 5.10(C), measured in 0.1 M PBS buffer, pH 7.1.

However, if we use a dopant with a higher internal mechanical strength, like PSS, high-quality 3D structures can be obtained by either cyclic voltammetry or by galvanostatic preparation, as shown in Figure 5.10 (C) and (D), respectively. Very nice interconnected hexagonal arrays resulted in both cases, as found in the pure PANI inverse opaline films. A most important finding is that, the PANI/PSS inverse opaline films still retain a good redox activity at neutral pH, after removal of the PS template by THF, as shown in Figure 5.11. A broad redox peak is observed between –0.15V and +0.4V, with a redox potential at around +0.083V, similar to that found for the unpatterned PANI/PSS system.[49, 51]

5.1.4 Application for Electrocatalysis

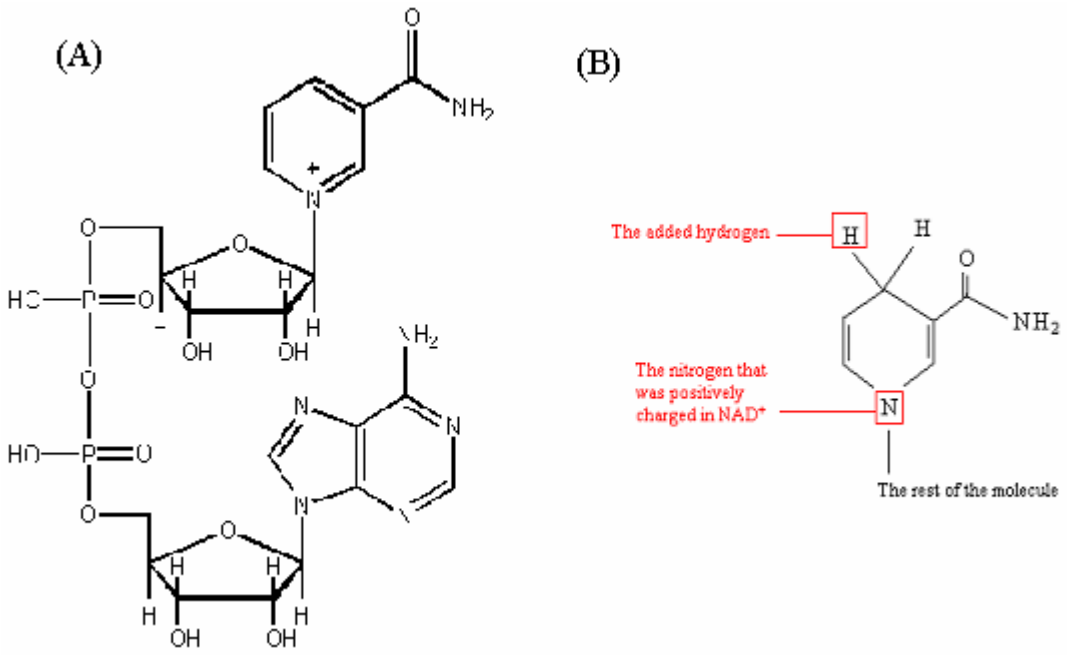

Fig. 5.12: The structure of NAD^+ A) and the change of the nicotinamide group when NAD^+ is reduced and become NADH B).

Considering the huge surface area of the prepared PANI/PSS inverse opal films and their capability of being redox-active at neutral pH, they are promising candidates either for electrocatalysis, or as a support for biomolecules, like enzymes or other proteins. It has been previously reported[48-52] that the doped PANI can electrocatalyze the oxidation of reduced ß-nicotinamide adenine dinucleotide (NADH) as shown in Figure 5.12. NADH and NAD^+ are important coenzymes and take part in a number of dehydrogenase enzymatic reactions and play an key role in developing amperometric enzyme sensors or biofuel cells that use dehydrogenase dependent enzymes. However normally different redox mediators are used to overcome the high potential (>1 V) needed for NADH oxidation. PANI doped with polyanions during the electropolymerization was found to be a good candidate.[80,81]

Our preliminary efforts to use PANI/PSS inverse opaline films as electrocatalytic supports for the oxidation of NADH showed that the electrocatalytic ability of these inverse opaline films is more than one order of magnitude higher than that for unpatterned PANI/PSS film (Figure 5.13). The sensitivity of the PANI composite

inverse opal films may be further enhanced and extended to other biological system by optimising the fabrication procedures and by selecting other suitable dopants.

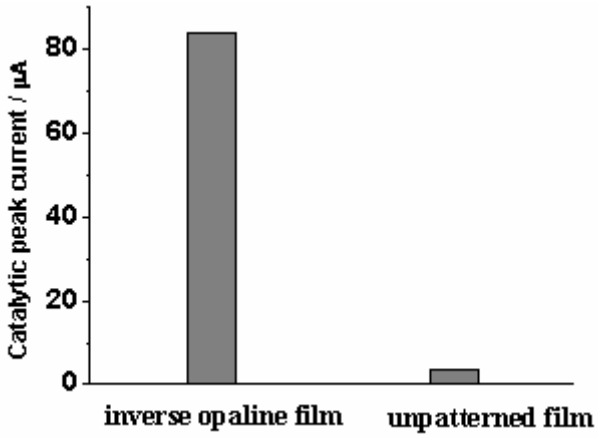

Fig. 5.13: Comparison of the electrocatalytic activity of a PANI/PSS inverse opaline film toward the oxidation of NADH and that of the unpatterned PANI/PSS film with the same film thickness. The NADH concentration was 10 mM, and the CV scan rate was 5 mVs^{-1}.

5.2 Preparation of Monodisperse Carbon Particle Arrays with Hierarchic Structures by Silica Inverse Opal Templates (this work has been done in cooperation with Dr. Zhi L in Prof. Muellen' group at the MPIP)

A general method for preparing carbon nanoparticles (CNPs) with controllable hierarchical first order structure (FOS), second order structure (SOS) and higher order structure (HOS) was developed by combining the precursor defined pyrolysis (PDP) of specific organic compounds and the template method of silica inverse opals that can be dissolved in dilute HF acid.

5.2.1 Experimental

Silica inverse opals on quartz substrates were prepared by depositing a bimodal colloidal mixture of 626 nm polystyrene particles (PS) and 6 nm silica nanoparticles in suspension by vertical lifting followed by pyrolysis in air. Details of the procedure can be found in chapter 3. Compounds **1,**[82] **2**,[86] and **3**[84] shown in Figure 5.14 were synthesized according to procedures described elsewhere. The compounds were dissolved in THF (for **1** and **3**) or acetone (for **2**) (5-30 mg/mL); and the solution was introduced into the template by drop casting. The amount of substance loaded into the template can be controlled by the concentration of solution and by the volume of solution applied to the silica template. All the heat treatments and pyrolysis of the samples (PDP) were carried out on quartz slides in an electric furnace in an argon atmosphere. The silica inverse opal templates were dissolved in 5 % aqueous HF solution after PDP procedure. The template-free samples were washed with water and ethanol, dried under vacuum and subjected to further characterization. SEM measurements were performed on a LEO 1530 field emission scanning electron microscope. TEM studies were conducted on a Philips EM420 electron microscope operating at 120 kV. DSC measurements were performed on a Netsch DSC 200 (Germany) at a scanning rate of 10 K min^{-1}. TGA measurements were recorded on a Mettler TG50 thermobalance.

5.2.2 Results

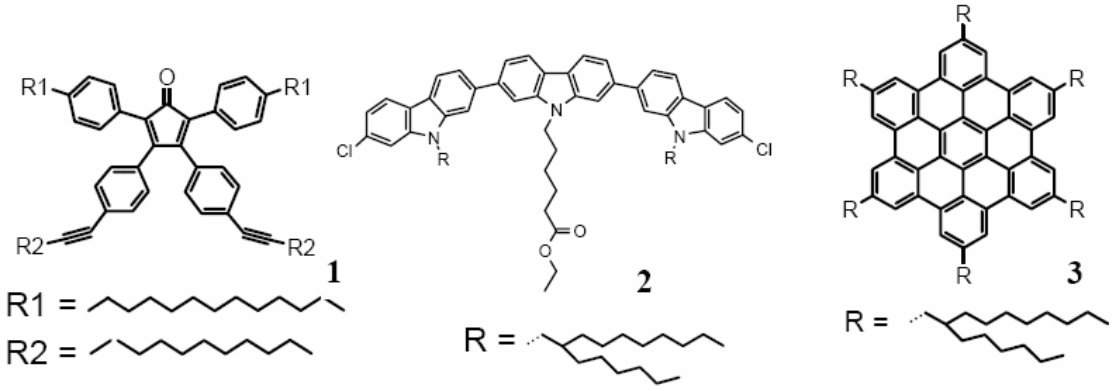

Fig. 5.14: Three carbon rich precursors used for pyrolysis (PDP) in silica inverse opal templates.

Dr. Zhi and I used silica inverse opals as templates to prepare hierarchic carbon nanoparticles (CNP) based on recently developed precursor directed pyrolysis (PDP).[82] Three carbon-rich molecules shown in Figure 5.14 with totally different functionalities and thermal behaviors were chosen as precursors. The principle of choosing precursors is that the starting compound should contain at least two parts; one part must lead to the carbon material in high yield after pyrolysis, while the other part must supply flexibilities for processing and for multi-functionalization of the CNPs.

Cyclopentadienone and alkyne dienophile units of **1** can react in an intermolecular Diels-Alder cycloaddition to form thermally stable hyperbranched polyphenylenes. The long alkyl chains (R_1 and R_2) makes **1** solution processible and susceptible to yield porous structures at high temperatures.[82] **1** was introduced into the pores of the silica inverse opal templates by drop casting a THF solution of **1.** Stepwise heating of the **1**-loaded template at 250 ºC for 2 h and then 350 ºC for 2 h under argon produced cross-linked hyperbranched polyphenylene,[82] which was further pyrolysized at 600 ºC for 5 h to result in carbonaceous particles inside the pores of the silica inverse opal (Figure 5.15 a). After removing the template with dilute HF solution, well aligned, monodisperse CNP films were obtained (Figure 5.15 b). These films were constructed consisting of a layered architecture, and every layer was composed of orderly organized CNPs. Interestingly, two kinds of CNPs were formed in this case. The CNPs in the top layer of the film were semispheres having a bowl-shaped wall structure, see Figure 5.15 b), and c). Apparently, these semispheres originate because of the particular morphology of the top layer inverse opal shown in Figure 3.9. The

formation of the bowl-shape was probably owing to the surface tension of the melt composed of **1** and the small contact angle between the melt and the silica surface at high temperatures. Inside the film, spherical carbon particles were found (Figure 5.15 c). The diameter of the spheres was smaller than that of the original polystyrene spheres used for inverse opal preparation, possibly due to the shrinkage of the precursors during thermal treatment. The overall thickness of the CNP film could be varied by tuning the number of layers in the templating colloid crystals.

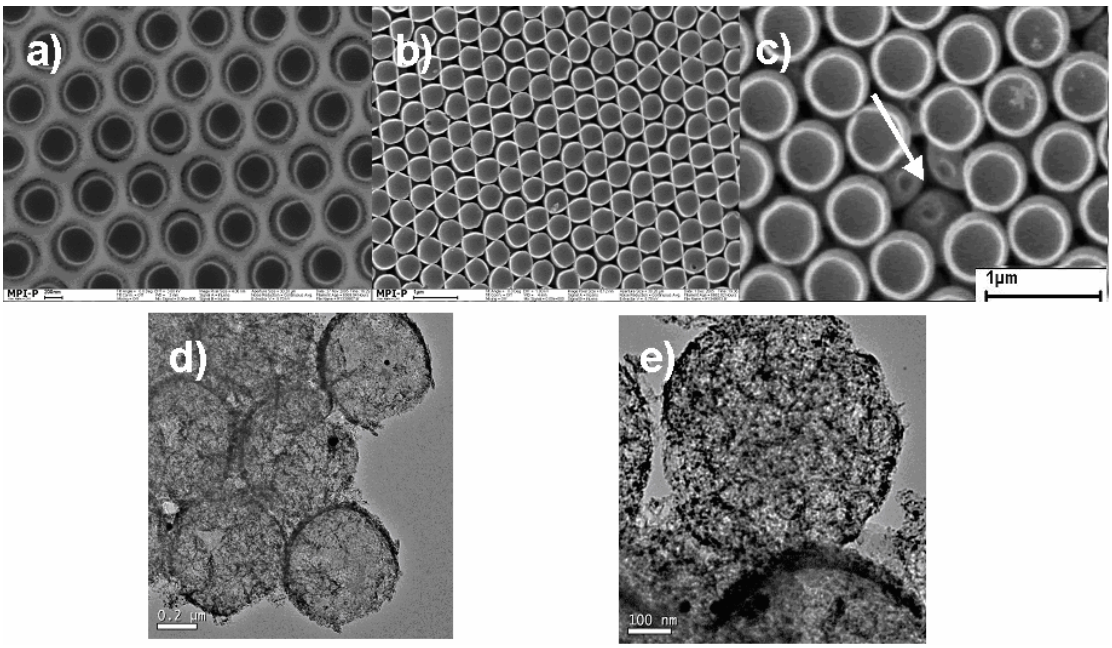

Fig. 5.15: SEM images of a) carbonaceous materials formed within the template, b) well-organized CNPs obtained after removing the template, c) carbon spheres (as indicated by the arrow) were aligned underneath the bowl-shaped semispheres. TEM images of d) well-organized porous carbon spheres; e) magnified spheres with 3D highly porous internal structures after treatment at 600 ºC.

These CNPs were highly porous as revealed by TEM in Figure 5.15. d) and e). These images showed that the channels were connected with each other to form a 3D porous structure (Figure 5.15 e). The pores have different sizes, and most of them are smaller than 10 nm, leading to a huge surface area within the spheres. One can speculate that an increase of the temperature to 600 ºC resulted in a complete decomposition of the alkyl chains, which then evaporated through the cavities and left a porous structure behind.

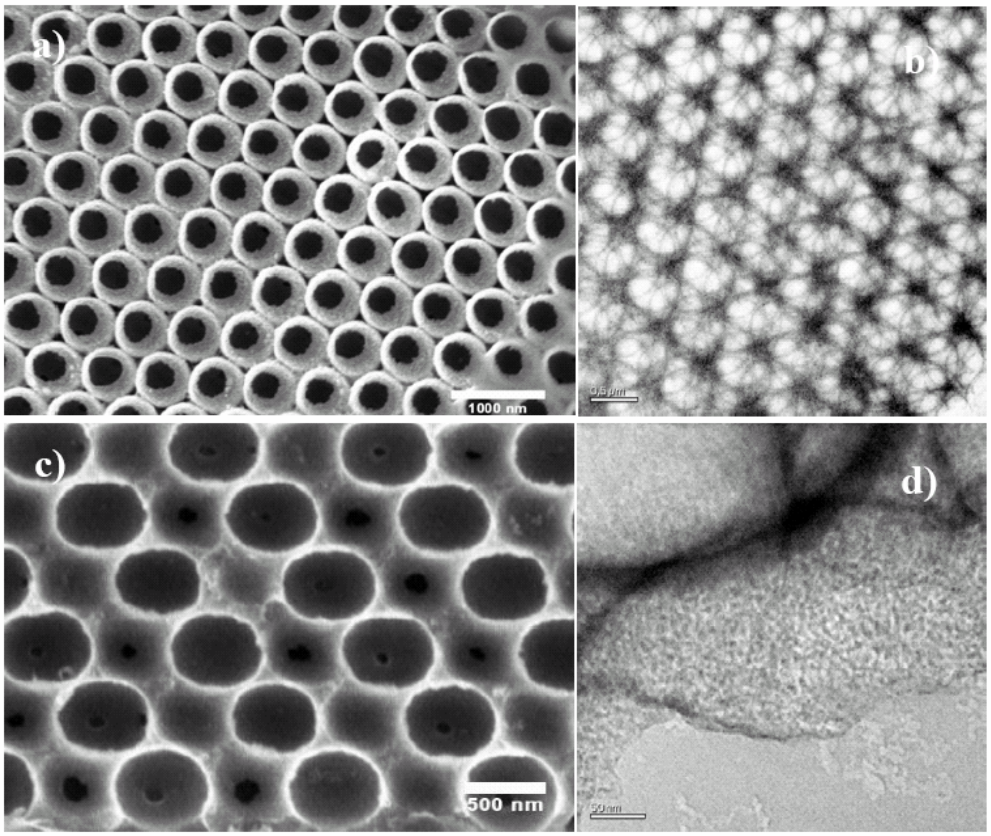

Fig. 5.16: SEM and TEM images of well organized carbonaceous hollow spheres obtained by the PDP method using compound **2** as precursor, a) and b) top view of the aligned hollow spheres showing the fcc (111) plane of the film, c) side view of the membrane revealing the fcc (110) plane, d) HRTEM showing homogeneously dispersed small Pt particles in the wall structure of the hollow spheres.

Precursor **2**, i) is again a combination of a rigid π-part and a soft alkyl part; ii) is an electron-rich species with heteroatoms that offer the potential for complexing metals; iii) contains chloro substituents that could facilitate cross-linking upon thermal treatment. CNPs obtained by PDP from **2** (Figure 5.16) are hollow carbonaceous spheres. These CNPs were aligned in an ordered fashion and most of them stuck together, thereby forming a porous first order structure, i.e. a CNP membrane (Figure 5.16. a). This is obviously the replica of the silica inverse opal template. At the same time, the hollow macropores (> 50 nm) of every CNP produced the second order structure of the membrane. The highly porous shell of every hollow sphere, containing mesopores (from 2 to 50 nm) with an average pore size below 10 nm, gave rise to the unique higher order structure of the membrane. In a subsequent step, metal particles could be introduced into the CNPs by an in-situ reduction method.[83] When a

mixture of **2** and hexachloroplatinic acid was loaded into the silica template, stepwise heat treatment of the mixture at 300 ºC for 2 h, 400 ºC for 2 h, and then 450 ºC for 2 h allowed very small Pt particles (5 nm) to disperse homogeneously in the shell of the carbon hollow spheres (Figure 5.16 d). These porous carbon supported Pt particles are expected to have applications as high performance catalysts.

Precursor **3** is a typical discotic mesogen,[85] and tends to form columnar aggregates due to the pronounced aromatic π-stacking interaction between the discs. Compared with hexa (4-dodecylphenyl)-*peri*-hexabenzocoronene (HBC-PhC12), compound **3** has very good solubility in organic solvents because of the branched long alkyl chains and the melting point (96 ºC) is low, allowing processing from solution or from the melt. Compound **3** thus appears to be an ideal precursor for the pyrolytic formation of graphitic species.

With stepwise thermal treatment of the **3**-loaded inverse opal at 400 ºC for 2 h, 500 ºC for 2 h, and then 600 ºC for 5 h, CNPs were formed in the pores of the template. After removal of the template, carbonaceous spheres were obtained, as shown in Figure 5.17. These monodisperse CNPs are organized in a layered fashion into an ordered lattice. Interestingly, compared to the bowl-shaped particles formed from **1**, the top layer formed from precursor **3** were also bowl-shaped particles, but with a slit on the bottom of the bowl (Figure 517a). One of the possible reasons for this peculiarity is the crystallization of the molecular discs during heat treatment, leading to density change of the sphere by shrinking and splitting of the solid surface. Underneath these slit-containing bowls, carbon spheres with several pits on the surface were formed (Figure 5.17 b). Generally, these pits came from the sinter necks of the inverse-opal template, which were produced during the preparation of the template.[85] However, these sinter necks are more obvious than those formed from **1** (Figure 5.15 c), suggesting stronger surface tension and crystallization tendency of precursor **3** during heat treatment.

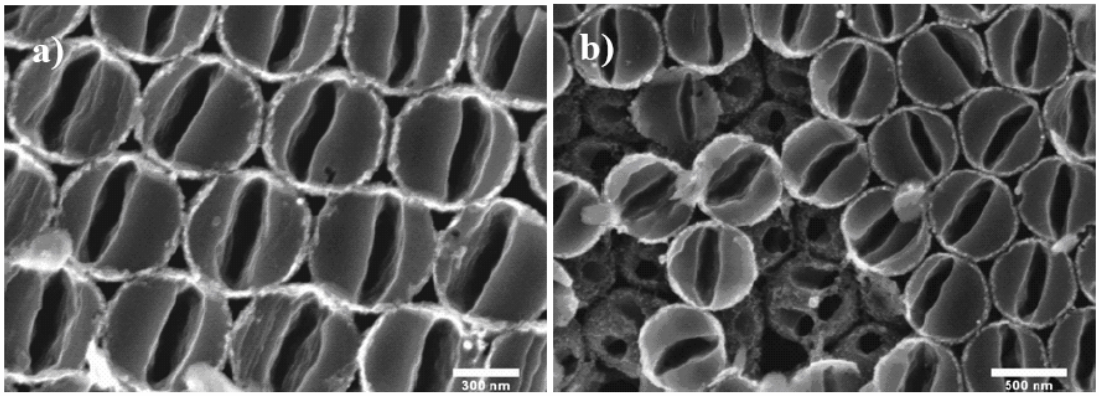

Fig. 5.17: SEM images of CNPs obtained by thermal treatment of compound **3** in the silica inverse opal template; a) top layer sphere with bowl-shaped morphology and slit structures, b) underneath the top layer, ball-shaped spheres were formed.

TEM characterization demonstrated that most of the bulk CNPs were completely filled particles (Figure 5.18) and, in the top layer, bowl-shaped particles were formed (Figure 5.18 b). In this case, well-organized CNP arrays formed the first order structure (FOS). The second order structure (SOS) was represented by the fully-filled spheres and slit-containing bowl-shaped particles, which were formed mainly due to the structure inducement of the precursor, **3**. Interestingly, besides FOS and SOS, higher order structure (HOS) could also be tuned by choosing different precursor structures. Selected area electron diffraction characterization (inset of Figure 5.18 a) disclosed that the CNPs shown in Figure 5.18 were constructed from aligned discotic structures with a distance of 0.35 nm between discs, suggesting a graphitic structure (inset of Figure 5.18 b). This is obviously due to the π-aromatic stacking and pre-arrangement of the discotic precursor molecules. Conductivity measurements of the CNPs showed that the product, obtained after thermal treatment of **3**, was semiconducting (the surface resistance of the film measured by a 4-probe method is about 100 MΩ) and thus attractive for fabrication of microelectronic devices.

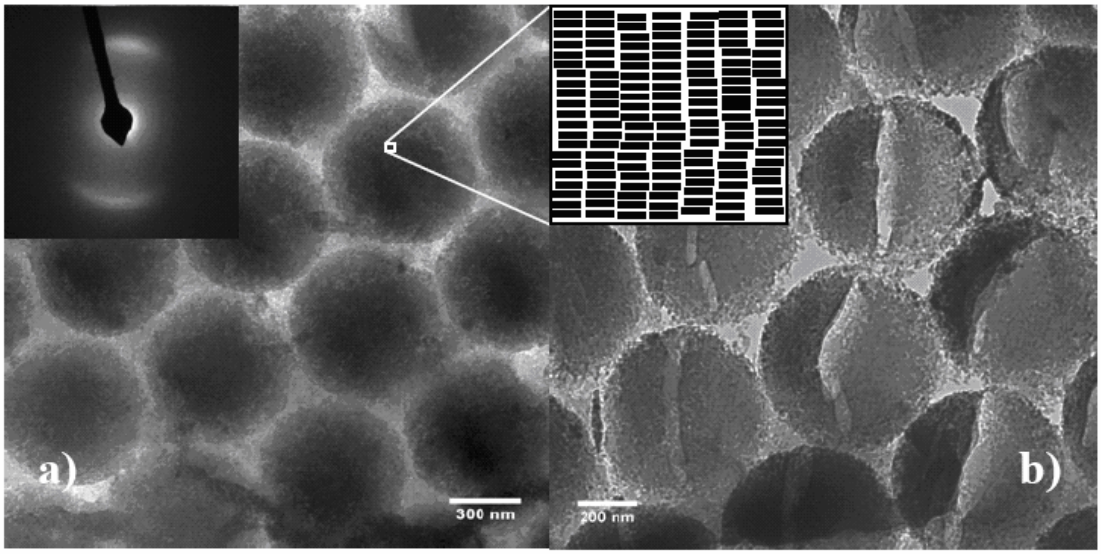

Fig. 5.18: TEM images of the obtained carbon spheres by thermal treatment of compound **3**; inset of a) shows the electron diffraction pattern of the carbon spheres; inset of b) illustrates the graphitic structures of the spheres formed by stacking of the discotic precursors.

5.3 Fabrication of Gold / Silica Composite Inverse Opals

To further explore applications of silica inverse opals as templates for 3D nanofabricaion, I also fabricated gold / silica composite inverse opals. Figure 5.19 demonstrates the preparation procedure. After functionalization of silica inverse opal wall with a positively charged silane (N-trimethoxysilylpropyl- N, N, N-trimethylammonium chloride),[87] negatively charged gold nanoparticles were deposited from suspension onto the silica inverse opal wall simply due to electrostatic attraction.[88] With electroless plating using gold nanoparticles as catalysts and seeds, a thin gold film was formed along the silica inverse opal wall, as such gold / silica inverse opals were formed.[89]

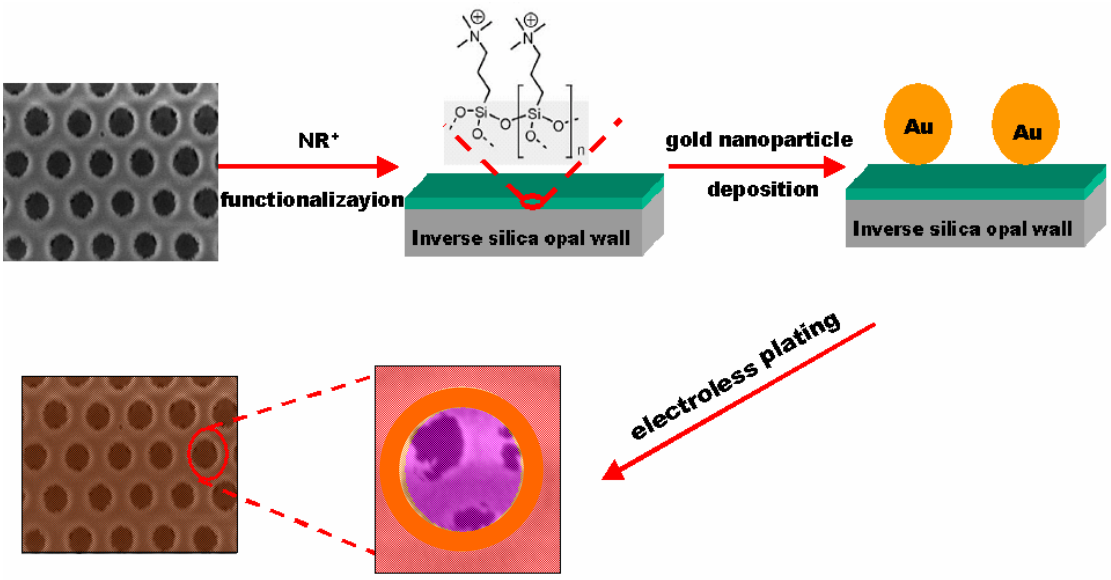

Fig. 5.19: Scheme of the preparation procedure.

Figure 5.20 presents images before and after gold nanoparticles deposition onto the silica inverse opal wall. Gold particles are distributed homogeneously throughout the whole inverse opal film with some separation between gold nanoparticles, due to the Coulomb repulsion force between the negatively charged gold nanoparticles.

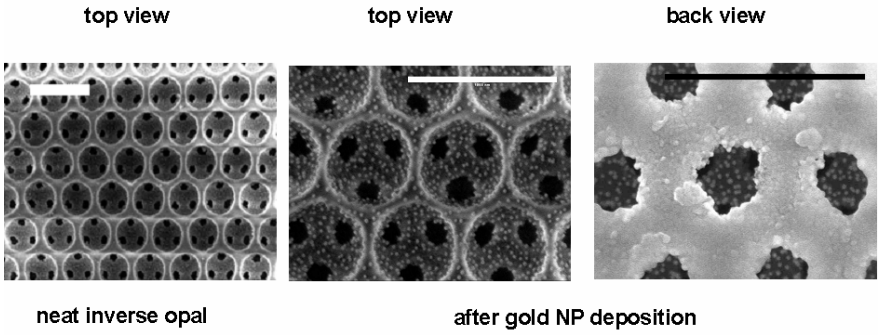

Fig. 5.20: SEM images of the inverse opals before and after gold nanoparticle deposition. The scale bar is 1μm.

Figure 5.21 are SEM images of inverse opals with gold particles at different plating time. Au^{3+} in the solution was reduced by hydroxylamine-hydrochloride onto the existing Au colloidal particles.[89] Here gold nanoparticles behave as catalysts and nuclei, therefore only increment in diameter of existing gold nanoparticles during electroless plating was observed. A thin granular gold film was formed along the

silica inverse opal scaffold and the opening of the composite inverse was still remained, when the plating time was 10 mins as shown in Figure 5.21 b). If the plating time was further increase, the opening would be closed as shown in Figure 5.21 c).

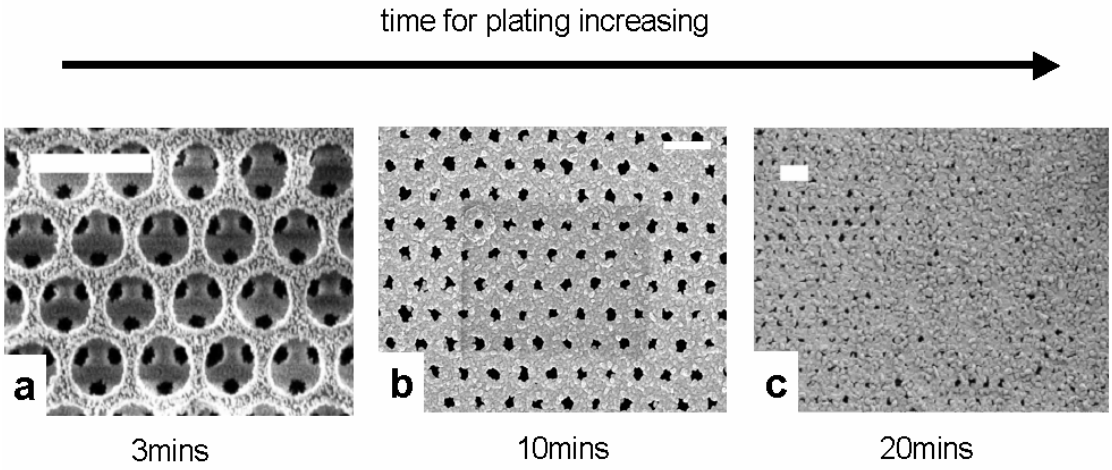

Fig. 5.21: SEM images of composite inverse opals at different stages of plating. The scale bar is 1μm.

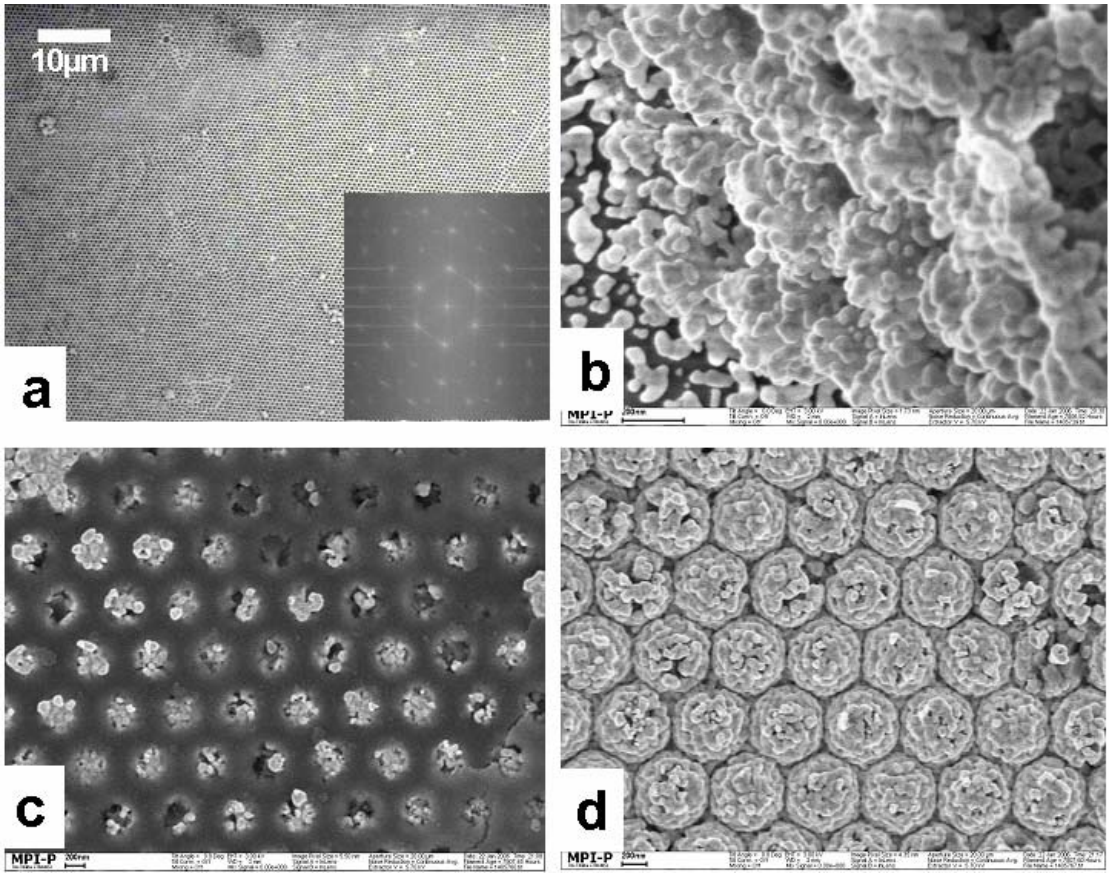

Fig. 5.22: a) low magnification image of the gold / silica inverse opal, inset is the FFT of the image, b) a perspective image from a crack, c) image from the back side, d) gold porous spheres after removal of silica template with HF acid.

Figure 5.22 a) is a low magnification image of gold / silica composite inverse, revealing that the domain between cracks can be as large as several hundred microns in diameter. Inset in Figure 5.22 a) is its FFT image, the hexagonal pattern of bright dots demonstrates that domain in Figure 5.22 a) is single crystalline. Figure 5.22 b), c) show the images from the crack and the backside, which confirm that the granular gold film extends throughout the entire silica inverse opal. Figure 5.22 d) is the SEM image of gold porous sphere array obtained after the removal of silica template.

As such, a convenient method for the preparation of silica / gold composite inverse opals is described. Removal of the silica scaffold, porous gold sphere array remains. Such gold silica inverse opals and gold porous array should find applications in surface enhanced Raman spectroscopy (SERS) and biosensing.

5.4 Conclusions

High quality inverse opals of pure PANI and its copolymers (like PANI/PSS) were fabricated via electrochemical methods utilizing PS colloidal crystal templates. The dopants incorporated had a significant effect on the structure and mechanical stability of the opaline films prepared, and the PANI composite films obtained remained electroactive at neutral pH. Due to their huge surface area, they showed a pronounced electrocatalytic efficiency and may present potential candidates for biosensing applications, e.g. as specific electrocatalyst or bioreactors.

Controllable hierarchic carbon nanoparticles were prepared using silica inverse opals as templates in combination with precursor defined pyrolysis. Also gold / silica inverse opals were prepared with silica inverse opal templates, and after removing the silica templates with HF acid, porous gold sphere arrays were obtained. Such gold silica inverse opals and gold porous array should find applications in surface enhanced Raman spectroscopy (SERS) and biosensing.

References:

1 Gates B., Yin Y., Xia Y., *Chem. Mater.* **1999**, *11*, 2827.

2 Jiang P., Hwang K. S., Mittleman D. W., Bertone J. F., Colvin V. L., *J. Am. Chem. Soc.* **1999**, *121*, 11630.

3 Kulinowski K. M.; Jiang P.; Vaswani H.; Colvin V. L. *Adv. Mater.* **2000**, *12*, 833.

4 Dai H., Wang E. W., Lu Y. Z., Fan, S. S., Lieber C. M., *Nature*, **1995**, *375*, 769.

5 Pan Z., Lai H. L., Au F. C. K., Duan X., *Adv. Mater*. **2000**, *12*, 1186.

6 Yan H., Blanfor C. F., Holland B. T., Smyrl W. H., Stein A., *Chem. Mater.* **2000**, *12*, 1134.

7 Rahman S., Yang H., *Nano Lett.* **2003**, *3*, 439.

8 General reviews on photolithography: *Optical Lithography*, a special issue of *IBM J. Res. Dev.* **1997**, *1-2*, 3.

9 Rogers J. A., Paul K. E., Jackman R. J., Whitesides G. M., *Appl. Phys. Lett.* **1997**, *70*, 2658.

10 Xia Y., Whitesides G. M., *Angew. Chem., Int. Ed. Engl.* **1998,** *37*, 550.

11 a) Piner R. D., Zhu J., Xu F., Hong S. H., Mirkin C. A., *Science* **1999**, *283*, 661. b) Jaschke M., Butt H., *Langmuir* **1995**, *11*, 1061.

12 Hariharan P., *Optical Holography: Principles, Techniques, and Applications*, 2nd ed., Cambridge University Press, New York **1996**.

13 Park M., Harrison C., Chaikin P. M., Register R. A., Adamson D. H., *Science* **1997,** *276*, 1401.

14 Morey M. S., O'Brien S., Schwarz S., Stucky G. D., *Chem. Mater.* **2000**, *12*, 898.

15 Cheng W., Baudrin E., Dunn B., Zink J. I., *J. Mater. Chem.* **2001**, *11*, 92.

16 Grosso D., Boissiere C., Smarsly B., Brezesinski T., Pinna N. Albouy P. A., Amenitsch H., Antonietti M. Sanchez C., *Nat. Mater.* **2004**, *3*, 787

17 Martin C. R., *Science* **1994**, *266*, 1961.

18 Yuan Z. H., Huang H., Fan S. S., *Adv. Mater.* **2002,** *14*, 303.

19 Yuan Z. H., Huang H., Dang H. Y., Cao J. E., Hu B. H., Fan S. S., *Appl. Phys. Lett.* **2001**, *78*, 3127.

20 Rahman S., Yang H., *Nano Lett.* **2003**, *3*, 439.

21 Holland B. T., Blanford C. F., Stein A., *Science* **1998**, *281*, 538.

22 Jiang P., Bertone J. F., Colvin V. L., *Scince* **2001**, *291*, 453.

23 Norell M. A., Makovicky P., Clark J. M., *Nature* **1997**, *389*, 447.

24 Dai H., Wong E. W., Lu Y. Z., Fan S., Lieber C. M., *Nature* **1995**, *375*, 769.

25 Kresge C. T., Leonowicz M. E., Roth W. J., Vartuli J. C., Beck J. S., *Nature* **1992**, *359*, 710.

26 Wijnhoven J. E. G. J., Vos W. L., *Science*, **1998**, *281*, 802.

27 Braun P. V., Wiltziusm P., *Nature* **1999**, *402*, 603.

28 Tetreault N. T., Miguez H., Ozin G. A., *Adv. Mater.* **2004**, *16*, 1471.

29 Lodahl P., Driel A. F. V., Nikolaev I. S., Irman A., Overgaag K., Vanmaekelbergh D., Vos W. L., *Nature* **2004**, *430*, 654.

30 Vanmaekelbergh D., Vos W. L., *Nature* **2004**, *430*, 654.

31 Jiang P., *Angew. Chem. Int. Ed.* **2004**, *43*, 5625.

32 Cassagneau T., Caruso F., *Adv. Mater*. **2002**, *14*, 1629.

33 Cassagneau T., Caruso F., *Adv. Mater.* **2002**, *14*, 1837.

34 Wang Y., Caruso F., *Chem. Commun*. **2004**, 1528.

35 Wang Y., Caruso F., *Adv. Funct. Mater.* **2004**, *14*, 1012.

36 Qian W., Gu Z., Fujishima A., Sato O., *Langmuir* **2002**, *18*, 4526.

37 Velev O. D., Tessier P. M., Lenhoff A. M., Kaler E. W., *Nature*, **1999**, *401*, 548.

38 Jiang P., Cizeron J., Bertone J. F., Colvin V. L., *J. Am. Chem. Soc.* **1999**, *121*, 7957.

39 Deutsch M., Vlasov Y. A., Norris D. J., *Adv. Mater.* **2000**, *12*, 1176.

40 Yoshino K., Tatsuhara S., Kawagishi Y., Ozaki M., Zakhidov A. A., Vardeny Z. V., *Appl. Phys. Lett.* **1999**, *74*, 2590.

41 Sumida T., Wada Y., Kitamura T., Yanagida S., *Chem. Commun.* **2000**, 1613.

42 Park S. H., Xia Y., *Adv. Mater.* **1998**, *10*, 1045.

43 Johnson S. A., Oliver P. J., Mallouk T. E., *Science* **1999**, *283*,963.

44 Cassagneau T., Caruso F., *Adv. Mater.* **2002**, *14*, 34.

45 Wang D., Caruso F., *Adv. Mater.* **2001**, *13*, 350.

46 Diaz A. F., Logan J. A., *J. Electroanal. Chem*., **1980**, *111*, 111.

47 Ohsaka T., Ohnuki Y., Oyama N., Katagiri K., Kamisako K., *J. Electroanal. Chem.* **1984**, *161*, 399

48 Karyakin A. A., Strakhova A. K., Yatsimirsky A. K., *J. Electroanal. Chem*. **1994**, *371*, 259.

49 Bartlett P. N., Birkin P. R., Wallace E. N. K., *J. Chem. Soc., Faraday Trans.* **1997**, *93*, 1951.

50 Bartlett P. N., Wallace E. N. K., *J. Electroanal. Chem.* **2000**, *486*, 23.

51 Raitman O. A., Katz E., Bückmann A. F., Willner I., *J. Am. Chem. Soc.* **2002**, *124*, 6487.

52 Tian S. J., Baba A., Liu J. Y., Wang Z. H., Knoll W., Park M.-K., Advincula R., *Adv. Funct. Mater*. **2003**, *13*, 473.

53 Tian S. J., Armstrong N. R., Knoll W., *Langmuir* **2005**, *21*, 4656.

54 Tian S. J., Liu J. Y., Zhu T., Knoll W., *Chem. Commun*. **2003**, *21*, 2738.

55 Tian S. J., Liu J. Y., Zhu T., Knoll W., *Chem. Mater.* **2004**, *16*, 4103-4108.

56 http://nobleprize.org/chemistry/laureates/2000.

57 Syed A. A., Dinesan M. K., *Talanta* **1991**, *38*, 815.

58 Macdiarmid A. G., Mu S. L., Somasiri N., Wu W., *Mol. Cryst. Liq. Cryst*. **1985**, *121*, 187.

59 Paul E. W., Ricco A. J., Wrighton M. S., *J. Phys. Chem*. **1985**, *89*, 1441.

60 Kitani A., Yano J., Sasaki K. J., *Electroanal. Chem*. **1986**, *209*, 227.

61 Josowics M., Janata J., *Anal. Chem*. **1986**, *58*, 514.

62 Foulds N. F., Lowe C. R., *J. Chem. Soc., Faraday trans.* **1986**, *82*, 1259.

63 Diaz A. F., Logan J. A., *J. Electrochem. Chem***. 1980**, *111*, 111.

64 Shimano J. Y., MacDiarmid Alan G., *Synth. Met*. **1987**, *18*, 285.

65 Tian S. Ph.D dissertation p1.

66 Kohlman R. S., Zibold A., Tanner D. B., Ihas C. G., Ishiguro T., Min Y. G., Macdiarmid A. G., Epstein A. J., *Phys. Rew. Lett*. **1997**, *78*, 3915.

67 Fustin C. A.. Glasser G., Spiess H. W., Jonas U., *Adv. Mater.* **2003**, *15*, 1025.

68 Fustin C. A., Glasser G., Spiess H. W., Jonas U., *Langmuir* **2004**, *20*, 9114.

69 Shouldice G. T. D., Vandezande G.A., Rudin A., *Eur. Polym. J.* **1994**, *30*, 179.

70 Liu J. Y., Tian S. J., Knoll W., *Langmuir* **2005**, *21*, 5596.

71 Bobacka J., Ivaska A.,. Lewenstam A, *Electroanalysis* **2003,** 15, 366.

72 Nicolas-Debarnot D., Poncin-Epaillard F., *Anal. Chim. Acta* **2003**, *475*, 1.

73 Virji S., Huang J., Kaner R. B., Weiller B. H., *Nano lett.* **2004**, *4*, 491.

74 Pringsheim E., Zimm D., Wolfbeis O. S., Adv. Mater. **2001**, 13, 819.

75 Huang J., Virji S., Weiller B. H., Kaner R. B., *J. Am. Chem. Soc*. **2003**, *125*, 314.

76 Forzani E. S., Zhang H., Nagahara L. A., Amlani I., Tsui R., Tao N., *Nano Lett*. **2004**, *4*, 1785.

77 Ohsaka T., Ohnuki Y., Oyama N., Katagiri K., Kamisako K., *J. Electroanal. Chem*. **1984**, *161*, 399.

78 Karyakin A. A., Strakhova A. K., Yatsimirsky A. K., *J. Electroanal. Chem*. **1994**, *371*, 259.

79 Raitman O. A., Katz E., Bueckmann A. F., Willner I., *J. Am. Chem. Soc*. **2002**, *124*, 6487.

80 Moiroux J., Elving P. J. J., *Anal. Chem*. **1978**, *50*, 1056.

81 Jaegfeldt H., *J. Electroanal. Chem*. **1980**, *110*, 292.

82 a) Zhi L., Wu J., Li J., Kolb U., Müllen K., *Angew. Chem. Int. Ed.* **2005**, *44*, 2120; *Angew. Chem.* **2005**, *117*, 2158; b). Zhi L, Gorelik T., Wu J., Kolb U.,. Müllen K, *J. Am. Chem. Soc.* **2005**, *127*, 12792.

83 a) Lu J., Moon K., Xu J., Wong C. P., *J. Mater. Chem.* **2006**, *16*, 1543, b) L. Zhi, T. Zhao, Y. Yu, *Scripta Materialia* **2002**, *47*, 875.

84 Kastler M., Pisula W., Wasserfallen D, Pakula T., Müllen K., *J. Am. Chem. Soc.* **2005**, *127*, 4286.

85 King J. S., Gaillot D. P., Graugnard E., Summers C. J., *Adv. Mater.* **2006**, *18*, 1063.

86 Jung S., Pisula W., Rouhanipour A., Räder H. J., Jacob J., Müllen K., *Angew. Chem. Int. Ed.* **2006**, *45*, 2685; *Angew. Chem.* **2006**, *118*, 4801.

87 Jonas Ulrich, Krüger Christian, *J. Supramol. Chem.* **2002**, *2*, 255.

88 Liang Zhijian, Susha Andrei, FCaruso rank, *Chem. Mater.* **2003,** *15*, 3176.

89 Brown Kenneth R., Natan Michael J., *Langmuir*, **1998**, *14*, 726.

Chapter 6 Summary

Conventional emulsion polymerization, soapless emulsion polymerization, and seeded emulsion polymerization were employed to synthesize nano-, microspheres with functional groups of sulfate, carboxylic acid, poly ethylene glycol specifically designed for different purposes. Furthermore fluorescent dyes were introduced into the polymer particles with miniemulsion polymerzation.

Multilayer monomodal colloidal crystal (mCC), binary colloidal crystals (bCC) and trimodal colloidal crystals (tCC) (monomodal, binary and trimodal refer to the components of particles in the colloidal crystals, hence monomodal crystals have only one component, binary has two, and trimodal has three) were fabricated with vertical lifting deposition by one up-stroke, where the thickness can be easily controlled by adjusting the lifting speed, and the concentration of the colloidal particles in suspension. For binary colloidal crystals, the effects of the relative concentration in suspension and the relative size ratio between small and large particles on the binary crystal structure were systematically studied. Typical structural defects, like point defects (e.g. vacancies), line defects (e.g. dislocations), planar defects (e.g. stacking faults), and cracks, usually present in colloidal crystals formed by vertical deposition were also found in our materials and well identified in the SEM images. In the present mCCs the approximate diameter of compact domains between cracks were in the order of 10-50 μm, an approximate point defect areal density was about 0.005 μm^{-2} at the crystal surface, while line defects and stacking faults were found about every 5-10 μm. The defect density was further increased in the bCCs and additional defect types occured, which were due to packing faults of the small particles inside the fcc lattice of the large colloids and lattice variations in general. The successful preparation of binary and trimodal colloidal crystals provides an avenue for the realization of complete photonic bandgap materials.

The same method was applied for the direct replica formation and preparation of mono-inverse opals (mIO) and binary inverse opals (bIO) (mIO and bIO are defined by the air sphere components in inverse opals, so mIO means that such inverse opals consist of only one kind of air spheres and bIO is formed with two kind of air spheres) by simultaneous deposition of large, crystal-forming PS and PMMA latex particles (the sacrificial template), and replica-forming silica nanoparticles (the matrix material filling the interstitial space) followed by the removal of the templating particles by

pyrolysis. Such hierarchical meso and macroporous structures, which are mechanically robust and thermally stable, may find applications in catalysis, biomaterial engineering, and membrane reactors.

Optical properties of all the prepared crystals and inverse opal films are characterized by Vis-NIR spectroscopy, and analysis of the spectral shifts leads to the lattice composition in the bCC, tCC and bIO, which agrees well with the result from computer modeling.

In addition to vertical lifting deposition, a spotting technique was employed to produce colloidal crystal microarrays in parallel comprising of up to *9600* single colloidal crystal structures with dimensions down to 100 μm on microfabricated substrates. Optical properties of the colloidal crystal arrays were characterized by reflection spectroscopy. Vertical cell lifting method was also employed to fabricate silica nanoparticles arrays, which exhibits potential to assemble thicker nanoparticle films than the normal vertical lifting deposition.

Numerous vibrational eigenmodes of spherical submicrometer particles in fabricated soft opals are experimentally detected by Brillouin light scattering and theoretically identified by their spherical harmonics by means of single phonon scattering cross section calculations. The particle size polydispersity is reflected in the line shape of the low frequency modes.

First realization of hypersonic phononic crystals utilizing self-assembled colloidal crystals allows the control of the propagation of phonons and opens up the horizon of opportunities both in colloidal science and in the rapidly evolving new (about ten years old) field of phononics. The direct measurement of the dispersion relation in phononic crystals using the optical technique of Brillouin scatterings also allows the study of fundamental issues of phonon dissipation in these structures. The methodology of this work will contribute to the search for the designing of optimal phononic structures operating in the hypersonic regime, including the exploration of other fabrication techniques, e.g. holographic interference lithography.

High quality inverse opals of pure PANI and its copolymers (such as PAA, PSS) were fabricated via electrochemical polymerization in PS colloidal crystal templates. The incorporated dopants have a significant effect on the structure and mechanical stability of the prepared opaline films, and the obtained PANI composite films remained electroactive at neutral pH. Due to their huge surface area, they showed

pronounced electrocatalytic efficiency and may present potential candidates for biosensing applications, e.g. as specific electrocatalysts or bioreactors.

A method was developed for the preparation carbon nanoparticles with controllable hierarchic structures using silica inverse opals as templates in combination with the precursor defined pyrolysis (PDP). Silica inverse opals were further used for the preparation of gold / silica inverse opals, and gold porous sphere arrays were obtained by the removal of silica scaffold.